Large Eddy Simulation of High Reynolds Number Complex Flows

A DISSERTATION
SUBMITTED TO THE FACULTY OF THE GRADUATE SCHOOL
OF THE UNIVERSITY OF MINNESOTA
BY

Aman Verma

IN PARTIAL FULFILLMENT OF THE REQUIREMENTS
FOR THE DEGREE OF
DOCTOR OF PHILOSOPHY

Krishnan Mahesh, Adviser

September, 2012

Acknowledgements

I am grateful to Prof. Krishnan Mahesh for giving me the opportunity to pursue my doctoral research under his guidance and for his constant support and encouragement. He is patient, attentive and always keen to discuss and address problems. I have learned a lot from his profound knowledge, expertise and experience.

My parents Mr. Arun Kumar Verma and Mrs. Meenu Verma, and my sister Aakansha are a source of unconditional and constant support, and encouragement. My achievements would not be possible without them. I would especially like to thank Ms. Fiona Ng for being understanding and supportive, and motivating me in my endeavors.

My life in Minnesota and the graduate school experience was memorable because of my friends, some of whom are Dr. Abhijit Chakraborty, Dr. Projjwal Banerjee, Dr. Rajes Sau and Amartya S. Banerjee. I have enjoyed working with all my group members who provided helpful advice and good conversations. I would like to thank Dr. Suman Muppidi, Dr. Hyunchul Jang, Dr. Michael D. Mattson, Prahladh Iyer, Rajapandiyan Asaithambi, Zane Nitzkorski, Dr. Xiaochuan Chai and Aswin Gnanaskandan.

I am grateful to Dr. Peter Chang, Dr. Stuart Jessup and their colleagues at the Naval Surface Warface Center Carderock Division (NSWCCD) for providing us with experimental data for propeller crashback. I am also grateful to Prof. Joseph Katz and Dr. Xiaofeng Liu at John Hopkins University for providing the experimental data for turbulent flow past a cavity.

This work was supported by the United States Office of Naval Research (ONR) under ONR Grant N00014-05-1-0003 with Dr. Ki-Han Kim as technical monitor. Computing resources were provided by the Arctic Region Supercomputing Center (ARSC), Minnesota Supercomputing Institute (MSI), Texas Advanced Computing Center (TACC) and the National Institute for Computational Sciences (NICS).

To my mother, father and sister

Abstract

Large eddy simulation (LES) using the dynamic Smagorinsky model (DSM) [1, 2] and discretely kinetic energy conserving numerical methods [3] has successfully predicted complex flows such as gas turbine combustors [3] and marine propeller crashback [4–8]. This dissertation discusses three advancements towards reliably using LES for high Reynolds number complex flows on unstructured grids: (1) predicting and understanding the massively separated crashback flow past a propeller with hull, (2) a dynamic Lagrangian model with dynamic estimation of the Lagrangian timescale for inhomogeneous flows, and (3) a hybrid constrained wall model for attached wall-bounded flows.

Propeller crashback is an off-design operating condition where a propeller rotates in the reverse direction. Experiments [9] have shown that the presence of an upstream hull significantly increases the side-force on a propeller in crashback below an advance ratio of $J = -0.7$. LES is performed for a propeller with and without hull at two advance ratios, $J = -1.0$ and $J = -0.5$. LES reproduces the experimentally observed behavior and shows good quantitative agreement. Time averaged flow fields are investigated for a qualitative understanding of the complex flow resulting from the interaction of the upstream hull with the propeller blades. At $J = -1.0$, two noticeable flow features are found with the hull - a recirculation zone upstream in the vicinity of the propeller and a vortex ring much closer to the propeller. In contrast, at $J = -0.5$, there is a much smaller recirculation zone which is further upstream due to the increased reverse flow. As a result, the hull does not make much difference in the immediate vicinity of the propeller at $J = -0.5$. For both advance ratios, side-force is mostly generated from the leading edge separation on suction side. However, high levels of side-force are also generated from trailing edge separation on suction side at $J = -1.0$.

The dynamic Lagrangian averaging approach for the Dynamic Smagorinsky Model

(DSM) for LES, proposed by Park and Mahesh [10], is extended to an unstructured grid framework and applied to inhomogeneous complex flows. The Lagrangian time scale is dynamically computed from the solution and does not need any adjustable parameter. The Lagrangian time scale used in the standard Lagrangian model by Meneveau et al. [11] contains an adjustable parameter θ. The dynamic time scale is computed based on a "surrogate-correlation" of the Germano-identity error (GIE). Also, a simple material derivative relation is used to approximate GIE at different events along a pathline instead of Lagrangian tracking or multi-linear interpolation. The proposed model is applied to LES of turbulent channel flow on unstructured zonal grids at various Reynolds numbers. Improvement is observed when compared to other averaging procedures for DSM, especially at coarse resolutions. The model is also applied to flow over a cylinder at two Reynolds numbers and good agreement with previous computations and experiments is obtained. Noticeable improvement is obtained using the proposed model over the standard Lagrangian model; this is attributed to a physically consistent Lagrangian time scale. The model also shows good performance when applied to flow past a propeller with hull in crashback at $J = -0.7$. It regularizes the eddy viscosity, adjusts locally to the dominant flow features and has negligible additional overhead.

A constrained formulation for the dynamic subgrid-scale model for LES is proposed. It is employed as a dynamic wall model when the constraint is imposed in the near-wall region of attached wall-bounded flows. An externally prescribed Reynolds stress is used as the constraint. However, unlike conventional zonal approaches, Reynolds stress is not imposed as the solution, but used as a constraint on the subgrid-scale stress so that the computed Reynolds stress closely matches the prescribed one only in the mean sense. In the absence of an ideal wall model or adequate near-wall resolution, an LES solution at coarse resolution is expected to be erroneous very near the wall while giving reasonable predictions away from the wall. The Reynolds stress constraint is limited to the region where the LES solution is expected to be erroneous. The Germano-identity error (GIE) is used as an indicator of LES quality such that the Reynolds stress constraint is activated only where the GIE exceeds a certain threshold. The proposed model is applied to LES of turbulent channel flow at various Reynolds numbers and grid resolutions to obtain significant improvement over DSM, especially at coarse resolutions. This formulation is extendable to constraints on the mean of other flow quantities.

Contents

List of Tables

List of Figures

Chapter 1

Introduction

1.1 Motivation

Turbulent flows commonly occur in many natural and engineering settings such as in the atmosphere, over an aircraft, past off-shore platforms, inside engines, and over computer chips. Reynolds number (Re), which is a measure of the dominance of inertial forces to viscous forces, is characteristically high for turbulent flows. Traditionally, many Computational Fluid Dynamics (CFD) codes are based on the Reynolds Averaged Navier-Stokes (RANS) methods. Although, RANS has met with success for attached wall-bounded flows, it is inadequate for predicting more challenging and unsteady complex flows. On the other hand, Direct Numerical Simulation (DNS) is a simulation methodology where all the scales of turbulence are resolved down to the Kolmogorov scale. However, high Reynolds number flows exhibit such a large range of length and time scales that DNS is rendered prohibitively expensive for the foreseeable future.

Large Eddy Simulation (LES) is a viable analysis and design tool for complex flows due to advances in massively parallel computers and numerical techniques. LES is essentially an under-resolved turbulence simulation using a model for the unresolved or subgrid-scales (SGS) to account for the inter-scale interaction between the resolved and the unresolved scales. As a result, its computational cost is lower than that of DNS. The success of LES is due to the dominance of the large, geometry dependent, resolved scales over the small, unresolved scales in determining important flow dynamics and statistics.

Figure 1.1: DARPA SUBOFF model AFF8 with fairwater and appendages [12].

Marine configurations are subject to a variety of complex hydrodynamic phenomena affecting the overall performance of the vessel. The turbulent flow affects the hydrodynamic drag, propulsor performance and structural integrity, control-surface effectiveness, and acoustic signature of the marine vessel. Hence, an unsteady numerical simulation methodology such as LES is well suited to study such complex turbulent flows. For example, the Reynolds number for flow past a model marine vessel (e.g. DARPA SUBOFF in fig. 1.1) is on the order of $Re \sim O(10^7)$ based on the freestream and vessel length. Currently, RANS and hybrid variants of RANS-LES methods (such as Detached Eddy Simulation - DES) are used to numerically simulate such high Re flows. LES also promises increased accuracy over RANS based methods in predicting unsteady phenomena such as cavitation and noise production.

1.2 Overview

This dissertation develops the capability to enable LES of high Re flows in complex geometries (e.g. a marine vessel) and provide physical insight into the turbulent flow. This is achieved in the following steps. Firstly, LES is performed to investigate the geometry induced separated flow past a marine propeller attached to a hull, in an off-design condition called crashback. Secondly, fundamental developments in LES modeling are pursued to improve the LES predictions, especially for high Re complex flows on relatively coarse, unstructured grids. The techniques employed to investigate the physical flow features and the LES models developed are general and applicable to other flow scenarios as well. Wherever appropriate, statistical *a posteriori* testing of the proposed LES and SGS models is performed by comparing with available DNS and experimental data. A review of the past work is included in the relevant chapters of this dissertation.

The principal contributions of this work are as follows:

- LES is performed for a marine propeller with and without an upstream hull at two advance ratios, $J = -1.0$ and $J = -0.5$. LES reproduces the experimentally observed increase of side-force at $J = -1.0$ and shows good quantitative agreement. The time averaged flow fields are analyzed to reveal the effect of the hull and explain the generation of higher side-force with the hull at $J = -1.0$. Furthermore, the flow fields are conditionally averaged to understand extreme loading events (high and low amplitude side-force). This understanding is used to propose a physical mechanism to explain the generation of different side-force at different advance ratios with the hull.

- The dynamic Lagrangian averaging approach for the Dynamic Smagorinsky Model (DSM) for LES, proposed by Park and Mahesh [10], is extended to an unstructured grid framework and applied to complex flows. Park and Mahesh [10] computed their time scale for homogeneous flows by averaging along directions of homogeneity. The present work proposes modifications for inhomogeneous flows on unstructured grids. This development allows the Lagrangian averaged dynamic model to be applied robustly to inhomogeneous flows without any adjustable parameter.

- The proposed SGS model is applied to LES of turbulent channel flow, flow over a cylinder and propeller crashback, on unstructured grids. The variation of the proposed time scale with grids and Reynolds numbers is discussed. Improvement in statistics is observed when compared to other averaging procedures for DSM and over the standard Lagrangian time scale due to Meneveau et al. [11]. The improvement in results is due to the fact that the Lagrangian time scale is physically consistent with the instantaneous flow. The model regularizes the eddy viscosity and adjusts locally to the dominant flow features.

- A novel wall model is proposed for the Dynamic Smagorinsky Model (DSM) for application to LES of high Reynolds number wall-bounded flows. The wall model is formulated as a generalized constraint in the DSM methodology. It is imposed dynamically in the near-wall region of wall-bounded flows when the LES solution

is expected to be erroneous based on the Germano-identity error. An externally prescribed mean Reynolds stress is used as the constraint. However, unlike conventional zonal approaches, Reynolds stress is not imposed as the solution, but used as a constraint on the subgrid-scale stress so that the computed Reynolds stress closely matches the prescribed/target one only in the mean sense.

- The proposed wall model is applied to LES of turbulent channel flow at various Reynolds numbers upto $Re_\tau = 10000$ and grid resolutions to obtain significant improvement over DSM, especially at coarse resolutions. The effect of the near wall constraint on the computed eddy viscosity and subsequently the flow, is discussed. The model is also analyzed for its sensitivity to model parameters and numerical methods. This constrained formulation is general and can be extended to incorporate constraints on the mean of other flow quantities.

- LES is performed to predict cavitation in the turbulent flow past an open cavity. Turbulent inflow is obtained from a separate rescaled boundary layer simulation to match the turbulent inflow in the experiments of Liu and Katz [13]. The time averaged single-phase statistics are in good agreement with the experiment [13]. The sensitivity of the one-way coupled Euler-Lagrange numerical method to different initial bubble radii (R_{b0}) is studied by introducing bubbles of different R_{b0} and comparing their Lagrangian statistics. Smaller bubbles appear to cavitate the least and cavitation increases with increasing R_{b0}.

This dissertation is organized as follows. Chapter 2 covers the governing equations, SGS stress model for LES and a brief description of the algorithm/numerical discretization for unstructured grids. LES of the flow past a marine propeller with an upstream hull is studied in the crashback mode of operation in chapter 3. A dynamic procedure to estimate the Lagrangian time scale for the dynamic Lagrangian SGS stress model for unstructured grids is described in chapter 4. A novel hybrid RANS-LES constrained SGS stress model is described in chapter 5. Finally, LES is performed to predict cavitation in turbulent flow past a cavity in Appendix A.

Chapter 2

Numerical Method

2.1 Governing equations

A continuum description of a single phase fluid flow is provided by the Navier–Stokes (N–S) equations. The three-dimensional, incompressible, constant density N–S equations for a Newtonian fluid in a Galilean frame of reference are given by

$$\frac{\partial u_i}{\partial x_i} = 0, \tag{2.1}$$

$$\frac{\partial u_i}{\partial t} + \frac{\partial}{\partial x_j}(u_i u_j) = -\frac{\partial p}{\partial x_i} + \nu \frac{\partial^2 u_i}{\partial x_j \partial x_j}, \tag{2.2}$$

where t is time, $x_i \equiv (x, y, z)$ denotes the coordinate axes, $u_i \equiv (u, v, w)$ denotes the velocity, p is the pressure and ν is the kinematic viscosity. Note that density has been absorbed into the pressure term. Equations 2.1 and 2.2 are the conservation laws for mass and momentum respectively. In Direct Numerical Simulation (DNS), these equations are solved to fully resolve all the scales of turbulence down to the Kolmogorov scale.

2.2 Large eddy simulation

In Large Eddy Simulation (LES), the large energy carrying scales of turbulence are solved for by directly resolving the larger scales and modeling the effect of the smaller scales. The flow variables are decomposed into large scales (denoted by $\overline{(\cdot)}$) and small

scales (denoted by $(\cdot)'$):

$$f(\mathbf{x},t) = \overline{f}(\mathbf{x},t) + f'(\mathbf{x},t). \tag{2.3}$$

This decomposition is analogous to that for obtaining the Reynolds averaged Navier–Stokes (RANS) equations. However, important differences are that, in LES generally $\overline{f}$ is an unsteady field and $\overline{f'} \neq 0$. In LES, this decomposition or scale separation is achieved by applying a low–pass spatial filter G to the flow variable f:

$$\overline{f}(\mathbf{x},\Delta,t) = G * f(\mathbf{x},t) = \int_D G(\mathbf{x},\mathbf{x}-\mathbf{r},\Delta) f(\mathbf{r},t) dr, \tag{2.4}$$

where Δ is the filter width and the integration is over the domain of computation.

Applying the filter operation to the N–S equations yields the filtered N–S equations:

$$\begin{aligned} \frac{\partial \overline{u}_i}{\partial x_i} &= 0, \\ \frac{\partial \overline{u}_i}{\partial t} + \frac{\partial}{\partial x_j}(\overline{u}_i \overline{u}_j) &= -\frac{\partial \overline{p}}{\partial x_i} + \nu \frac{\partial^2 \overline{u}_i}{\partial x_j \partial x_j} - \frac{\partial \tau_{ij}}{\partial x_j}, \end{aligned} \tag{2.5}$$

where $\overline{(\cdot)}$ denotes the filtered flow variable at scale Δ and $\tau_{ij} = \overline{u_i u_j} - \overline{u}_i \overline{u}_j$ is the sub–filter scale (SFS) stress. In general, the filtering and differentiation operators do not commute and there is a commutation error [14]. Assuming a spatially uniform filter, the filtering and differentiation operators are assumed to commute. Note that in the absence of explicit filtering [15], the computational grid followed by the discretization operator constitute the "implicit filter" which is used to obtain the filtered N–S equations (eq. 2.5). Hence for implicitly–filtered or grid–filtered LES, SFS stress is equivalent to sub–grid scale (SGS) stress. This SGS stress τ_{ij} needs to be modeled to close eq. 2.5.

2.3 SGS stress model

It is generally accepted that small scales tend to be more universal and isotropic than large scales. Therefore, simple eddy viscosity type SGS models are widely used in LES to provide dissipation corresponding to the resolved scale energy that would be transferred to the sub–grid scales if they were resolved. The Smagorinsky model [16] relates the

anisotropic residual SGS stress to the filtered strain rate $\overline{S}_{ij}$ by an eddy viscosity ν_t

$$\tau_{ij} - \frac{1}{3}\tau_{kk}\delta_{ij} = -2\nu_t\overline{S}_{ij}. \tag{2.6}$$

The trace $\frac{1}{3}\tau_{kk}\delta_{ij}$ is absorbed in the pressure term. Analogous to the mixing–length hypothesis, the eddy viscosity is modeled as

$$\nu_t = l_s^2|\overline{S}| = -2(C_s\Delta)^2|\overline{S}|, \tag{2.7}$$

leading to the SGS stress model

$$\tau_{ij} - \frac{1}{3}\tau_{kk}\delta_{ij} = -2\nu_t\overline{S}_{ij} = -2(C_s\Delta)^2|\overline{S}|\overline{S}_{ij} \tag{2.8}$$

where C_s is a model coefficient and $|\overline{S}| = (2\overline{S}_{ij}\overline{S}_{ij})^{1/2}$.

In the standard Smagorinsky model, C_s is assumed to be a global adjustable parameter whose value is typically around 0.16. However, problems were encountered in applying a universal C_s to different flow regimes and in obtaining the appropriate behavior near walls.

The Dynamic Smagorinsky model (DSM) due to Germano et al. [1] removes this limitation by dynamically computing the model coefficient C_s from the resolved scales and allowing it to vary in space and time. DSM is based on the Germano identity

$$L_{ij} = T_{ij} - \widehat{\tau}_{ij} \tag{2.9}$$

where

$$L_{ij} = \widehat{\overline{u}_i\overline{u}_j} - \widehat{\overline{u}}_i\widehat{\overline{u}}_j, \qquad T_{ij} = \widehat{\overline{u}_i\overline{u}_j} - \widehat{\overline{u}}_i\widehat{\overline{u}}_j \quad \text{and} \quad \widehat{\tau}_{ij} = \widehat{\overline{u}_i\overline{u}_j} - \widehat{\overline{u}_i}\widehat{\overline{u}_j}. \tag{2.10}$$

Here, $\widehat{(\cdot)}$ denotes test filtering at scale $\widehat{\Delta}$ and is usually taken to be $\widehat{\Delta} = 2\Delta$. T_{ij} is analogous to τ_{ij} and is the corresponding SGS stress at the test filter scale. L_{ij} is the stress due to scales intermediate between Δ and 2Δ and can be computed directly from the resolved field. Similar to τ_{ij}, the deviatoric part (denoted by $()^d$) of T_{ij} is modeled

using the Smagorinsky model at scale and $\widehat{\Delta}$ as

$$T_{ij} - \frac{1}{3}T_{kk}\delta_{ij} = -2(C_s\widehat{\Delta})^2|\widehat{\overline{S}}|\widehat{\overline{S}}_{ij}. \tag{2.11}$$

The dynamic procedure to obtain the SGS model coefficient C_s attempts to minimize the Germano-identity error (GIE),

$$\begin{aligned}\epsilon_{ij} &= T^d_{ij} - \widehat{\tau}^d_{ij} - L^d_{ij} \\ &= 2(C_s\Delta)^2\left[\widehat{|\overline{S}|\overline{S}}_{ij} - \left(\frac{\widehat{\Delta}}{\Delta}\right)^2|\widehat{\overline{S}}|\widehat{\overline{S}}_{ij}\right] - L^d_{ij} \\ &= (C_s\Delta)^2 M_{ij} - L^d_{ij},\end{aligned} \tag{2.12}$$

where $M_{ij} = 2\left[\widehat{|\overline{S}|\overline{S}}_{ij} - \left(\frac{\widehat{\Delta}}{\Delta}\right)^2|\widehat{\overline{S}}|\widehat{\overline{S}}_{ij}\right]$.

Since $\epsilon_{ij}(C_s) = 0$ is a tensor equation, C_s is overdetermined. The standard DSM due to Germano et al. [1] satisfies $\epsilon_{ij}S_{ij} = 0$ to obtain C_s. Lilly [2] found the equations to be regularized when minimizing ϵ_{ij} in a least-square sense. The cost function to be minimized can be expressed in the form

$$\mathcal{J} = \int_\Omega \epsilon_{ij}(\mathbf{x})\epsilon_{ij}(\mathbf{x})d\mathbf{x}, \tag{2.13}$$

where Ω is the averaging domain. This yields

$$(C_s\Delta)^2 = \frac{(L_{ij}M_{ij})_\Omega}{(M_{ij}M_{ij})_\Omega}, \tag{2.14}$$

where $(\cdot)_\Omega$ denotes averaging over Ω. Germano et al. [1] suggested averaging over homogeneous directions for stability. In the absence of homogeneous directions in complex flows, the above terms can be averaged locally.

2.4 Numerical discretization

Eq. 2.5 is solved by a numerical method developed by Mahesh et al. [3] for incompressible flows on unstructured grids. The algorithm discretely conserves not only a first order quantity - momentum, but also a second order quantity - kinetic energy,

simultaneously. Discrete energy conservation ensures that the convective flux of kinetic energy, $\sum_{\text{cvs}} u_i \delta(u_i u_j)/\delta x_j$ has contributions only from the boundary faces. As a result, the algorithm is derived to be robust without numerical dissipation. The algorithm has been validated for a variety of problems over a range of Reynolds numbers [see 3].

The Harlow–Welch algorithm [17] is discretely kinetic energy conserving on staggered, structured grids. The numerical method developed by Mahesh et al. [3] is a finite volume method where the Cartesian velocities u_i and pressure p are stored at the centroids of the cells and the face–normal velocities v_n are stored independently at the centroids of the faces. Henceforth, all resolved flow variables will be denoted simply, without the overbar $\overline{()}$.

A predictor–corrector type, fractional–step method is used to solve eq. 2.5. The non–linear convective term is denoted by NL and the viscous term incorporating the SGS stress term is denoted by $VISC$. Explicit time advancement is performed using the Adams–Bashforth scheme which is $O(\Delta t^2)$. The predicted velocities u_i^* at the control volume centroids are first obtained from the previous time steps k and $k-1$:

$$\frac{u_i^* - u_i^k}{\Delta t} = \frac{1}{2}\left[3(NL + VISC)^k - (NL + VISC)^{k-1}\right], \tag{2.15}$$

and then interpolated using symmetric averaging ($O(\Delta x^2)$) to obtain the predicted face–normal velocities:

$$v_n^* = \left(\frac{u_{i,icv1}^* + u_{i,icv2}^*}{2}\right) n_i, \tag{2.16}$$

where the face–normal $\vec{n}$ and hence v_n points from control volume $icv1$ to $icv2$.
The corrector step

$$\frac{u_i^{k+1} - u_i^*}{\Delta t} = -\frac{\partial p^{k+1}}{\partial x_i} \tag{2.17}$$

is projected onto the face–normal as:

$$\frac{v_n^{k+1} - v_n^*}{\Delta t} = -\frac{\partial p^{k+1}}{\partial n}. \tag{2.18}$$

The continuity equation imposes the constraint

$$\sum_{\text{faces of cv}} v_n^{k+1} A_f = 0, \tag{2.19}$$

where A_f is the face area. Substituting in eq. 2.18 yields a Poisson equation for p^{k+1}:

$$\begin{aligned} \sum_{\text{faces of cv}} v_n^{k+1} A_f - \sum_{\text{faces of cv}} v_n^* A_f &= -\Delta t \sum_{\text{faces of cv}} \frac{\partial p^{k+1}}{\partial n} A_f \\ \Rightarrow \Delta t \sum_{\text{faces of cv}} \frac{\partial p^{k+1}}{\partial n} A_f &= \sum_{\text{faces of cv}} v_n^* A_f, \end{aligned} \tag{2.20}$$

which is solved using the Algebraic Multi-Grid (AMG) method of *hypre* [18].
Once p^{k+1} is known, the pressure gradient $\frac{\partial p}{\partial x_i}$ is computed in a novel least squares formulation which minimizes the conservation error:

$$\sum_{\text{faces of cv}} \left(\frac{\partial p}{\partial x_i} n_i A_f - \frac{\partial p}{\partial n} A_f \right)^2. \tag{2.21}$$

Finally, corrected u_i and v_n are computed from eqns. 2.17 and 2.18 using p^{k+1}.

Most of the simulations in this dissertation are performed with implicit time advancement using the Crank–Nicolson scheme which is $O(\Delta t^2)$:

$$\frac{u_i^* - u_i^k}{\Delta t} = \frac{1}{2} \left[(NL + VISC)^k + (NL + VISC)^{k+1} \right]. \tag{2.22}$$

$(NL + VISC)^{k+1}$ contains u_i^{k+1} which is expressed in terms of u_i^k as

$$u_i^{k+1} = u_i^* - \Delta t \frac{\partial p^{k+1}}{\partial x_i}, \tag{2.23}$$

where p^{k+1} is linearized as $p^{k+1} = p^k + O(\Delta t)$. Eq. 2.22 reduces to a system of linear equations which is solved for u_i^* using SOR.

Note that typically, the face–normal derivatives at a face are computed using

$$\frac{\partial (\cdot)}{\partial n} \Big|_f = \frac{(\cdot)_{nbr} - (\cdot)_{icv}}{d_f}, \tag{2.24}$$

where nbr denotes the neighboring control volume of icv and $d_f = (x_{i,nbr} - x_{i,icv}) n_{i,f}$ is the face–normal distance. For the simulations in chapters 4 and 5 of this dissertation, the face–normal derivatives of p, and u_i in $VISC$ are computed using the Improved Deferred Correction method of Jang [19]. Further details are available in Jang [19].

Chapter 3

LES of a Propeller with Hull in Crashback

3.1 Introduction

A forward moving marine vessel is decelerated by rotating the propeller in reverse. This off-design operating condition where the vessel moves in the forward direction while the propeller rotates in the reverse direction is termed crashback. Flow around the propeller in crashback is characterized by large scale unsteadiness and separation. Low frequency, high amplitude off-axis forces and moments produced by this unsteadiness are transmitted to the vessel, inhibiting its ability to maneuver. Furthermore, the unsteady, separated flow near the control surfaces can reduce the effectiveness of the control surfaces. Also, during this maneuver, the propeller blades experience huge unsteady forces which may cause them to bend, vibrate and even break.

The crashback condition is dominated by the interaction of the free stream flow with the strong reverse flow from reverse propeller rotation (fig. 3.1(a)). This interaction forms an unsteady vortex ring around the propeller and is the most remarkable aspect of the flow during crashback. The vortex ring state (VRS) is also an important topological feature in helicopter aerodynamics, particularly a helicopter rotor in axial descending flight. Analogous to marine vessels, helicopters in VRS may experience loss of altitude, changed control surface effectiveness and low frequency pitch and roll oscillations [20].

Jiang et al. [21] studied the structure of the unsteady vortex ring using Particle Image

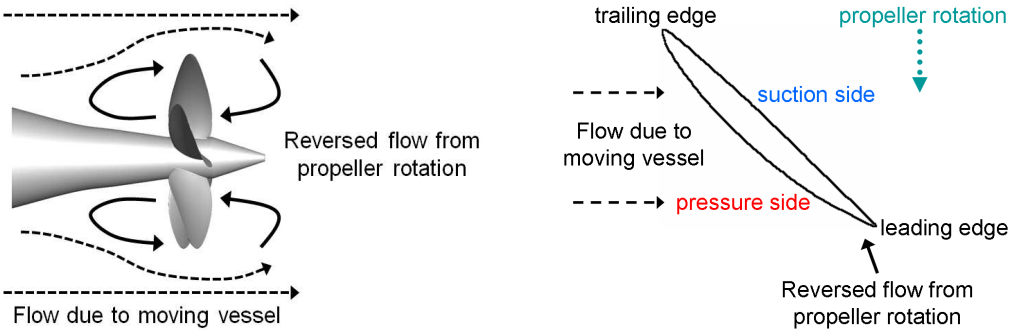

Figure 3.1: Crashback: (a) flow schematic, (b) location of leading, trailing edges, and pressure, suction sides on blade section.

Velocimetry (PIV) measurements. They noted that the asymmetry in the strength and location of the unsteady vortex ring is related to unsteady shaft forces and that the oscillation frequency of the vortex ring is much lower than the propeller rotation rate. Jessup et al. [22] presented more detailed measurements of flow velocity fields using Particle Image Velocimetry (PIV) and Laser Doppler Velocimetry (LDV).

The computational prediction of the flow around marine propellers has been performed using unsteady Reynolds-Averaged Navier-Stokes equations (RANS) by Davoudzadeh et al. [23] and Chen and Stern [24]. They showed that RANS yielded good results for forward ($V > 0$, $\omega > 0$) and backing ($V < 0$, $\omega < 0$) modes (attached flow regime) but produced significant discrepancies in crashback ($V > 0$, $\omega < 0$) and crashahead ($V < 0$, $\omega > 0$) modes (separated flow regime).

A cylindrical cross-section of a propeller blade resembles an airfoil. In the crashback condition, the leading and trailing edges of propeller blades exchange their roles. Hence, what used to be the sharp trailing edge in the forward operating condition becomes the leading edge in crashback and vice-versa. The leading (LE) and trailing edges (TE) of the propeller blades are defined as follows. LE is the downstream edge of the blade which first sees the reverse flow due to propeller rotation and TE is the other end as shown in fig. 3.1(b). The large flow separation at the sharp leading edge may cause high amplitude fluctuation of unsteady loads.

Mahesh et al. [3] developed a non-dissipative and robust finite volume method for

LES on unstructured grids. Vyšohlid and Mahesh [4, 5] performed numerical simulations of propeller in crachback with the same method at an advance ratio of $J = -0.7$. They showed that LES could yield good agreement for mean and rms values of unsteady loads. The computed power spectral density for unsteady loads showed the same peak as the experiment at 5 rev^{-1}. Chang et al. [6] performed LES at other advance ratios, $J = -0.5$ and $J = -1.0$ with the same LES code and computational grid as Vyšohlid and Mahesh [5]. They investigated instantaneous flow fields at a high thrust event and a low thrust event to understand the physics of crashback. They reported that a bi-modal behavior with vortex ring and axial jet modes occurred at low negative J. They also used the LES surface forces to predict shear stress and bending moments on the blades and obtained good agreement with experiments. Jang and Mahesh [7, 8] introduced two quantities for pressure contributions to thrust and side-force to observe that most of the thrust and side-force originated from the suction side of the leading edge of the propeller blades.

In the present work, flow past a propeller attached to an upstream hull, operating in the crashback condition is considered. A schematic of the flow is shown in fig. 3.1; flow is from left to right. The inflow to the propeller is not the freestream but the wake of the hull. Bridges' experiment [9] on an open propeller with an upstream submarine hull in the Large Cavitation Channel (LCC) noted that the side-force increased dramatically below an advance ratio of $J = -0.7$ compared to Jessup's experiment [25] without the hull in a 36 inch Water Tunnel (WT) (shown in fig. 3.2). However the reason for this discrepancy that an upstream hull causes is not well understood. The objectives of the present work are to: (i) evaluate the ability of LES to predict the interaction of an upstream hull with the propeller and (ii) provide a physical explanation for the above mentioned experimental observation.

This chapter is organized as follows. The set-up of the simulation including the numerical method, grid and boundary conditions are given in section 3.2. Results are shown for the effect of upstream hull on a propeller at two advance ratios $J = -1.0$ and $J = -0.5$ in section 3.3. A physical mechanism to explain the results is summarized in section 3.4.

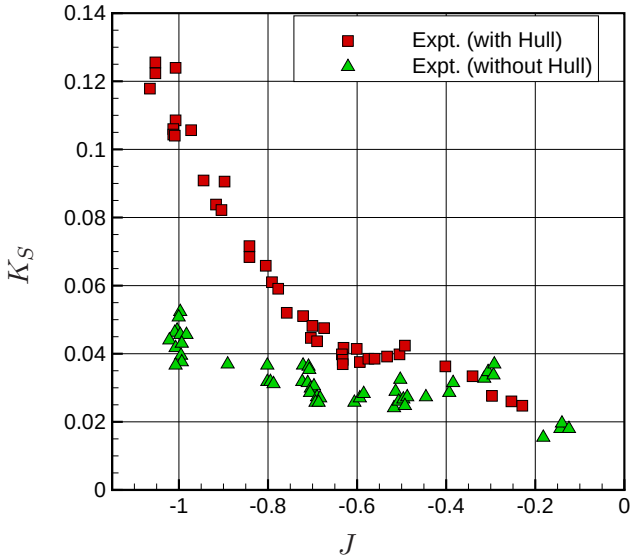

Figure 3.2: Increase in side-force magnitude with hull below $J = -0.7$. Reproduced from Jessup et al. [25].

3.2 Simulation details

3.2.1 Governing equations

Large eddy simulations are performed in a frame of reference that rotates with the propeller. The spatially filtered incompressible Navier–Stokes equations in the rotating frame of reference are formulated for the absolute velocity vector in the inertial frame as follows:

$$\begin{aligned} \frac{\partial \overline{u}_i}{\partial t} + \frac{\partial}{\partial x_j}(\overline{u}_i\overline{u}_j - \overline{u}_i\epsilon_{jkl}\omega_k x_l) &= -\frac{\partial \overline{p}}{\partial x_i} - \epsilon_{ijk}\omega_j\overline{u}_k + \nu\frac{\partial^2\overline{u}_i}{\partial x_j\partial x_j} - \frac{\partial \tau_{ij}}{\partial x_j} \\ \frac{\partial \overline{u}_i}{\partial x_i} &= 0 \end{aligned} \tag{3.1}$$

where u_i is the inertial velocity in the inertial frame, p is the pressure, x_i are coordinates in the rotating non-inertial reference frame, ω_j is the angular velocity of the rotating frame of reference, ν is the kinematic viscosity, ϵ_{ijk} denotes the permutation tensor and the approximation $\overline{u_i\epsilon_{jkl}\omega_k x_l} \approx \overline{u}_i\epsilon_{jkl}\omega_k x_l$ is used. $\tau_{ij} = \overline{u_iu_j} - \overline{u}_i\overline{u}_j$ is the sub-grid stress and is modeled by the Dynamic Smagorinsky Model (eq. 2.14). Eq. 3.1 is solved by the numerical method described in sec. 2.4.

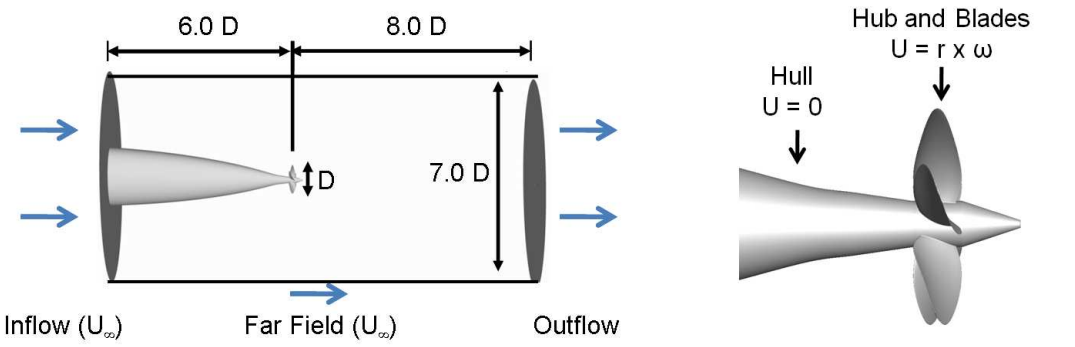

(a) (b)

Figure 3.3: (a) Computational domain and boundary conditions on domain boundaries, (b) boundary conditions on solid walls.

3.2.2 Propeller geometry, grid and boundary conditions

Simulations are performed for a marine propeller DTMB 4381, which is a five-bladed, right-handed propeller with variable pitch, no skew and no rake. The propeller has been used in various experiments [21, 22, 25] and computations [5, 6, 8, 23, 24]. For the hull geometry, a standard axisymmetric hull (DTMB Model 5495-3) is used. In the simulations, half of the hull body is used and stabilizing fins are ignored. Details of the propeller and hull geometry are given in Bridges [9].

The computational domain is a cylinder with diameter $7.0D$ and length $14.0D$ where D is the diameter of the propeller disk. Free-stream velocity boundary conditions are specified at the inlet and the lateral boundaries. Convective boundary conditions are prescribed at the exit. Since the velocities in the governing equations (eq. 5.4) are referred to in the inertial frame, boundary conditions on solid walls are also prescribed in the inertial frame. Thus, boundary conditions on the rotor part, blades and hub are specified as $u = \omega \times r$, while those on that hull or shaft are prescribed as no-slip boundary conditions. A schematic of the computational domain and boundary conditions is shown in fig. 3.3.

In the present work, simulations are performed for the propeller with and without hull at two advance ratios, $J = -1.0$ and $J = -0.5$. The grid for propeller without hull has 7.7 million control volumes and for propeller with hull, 7.3 million control volumes.

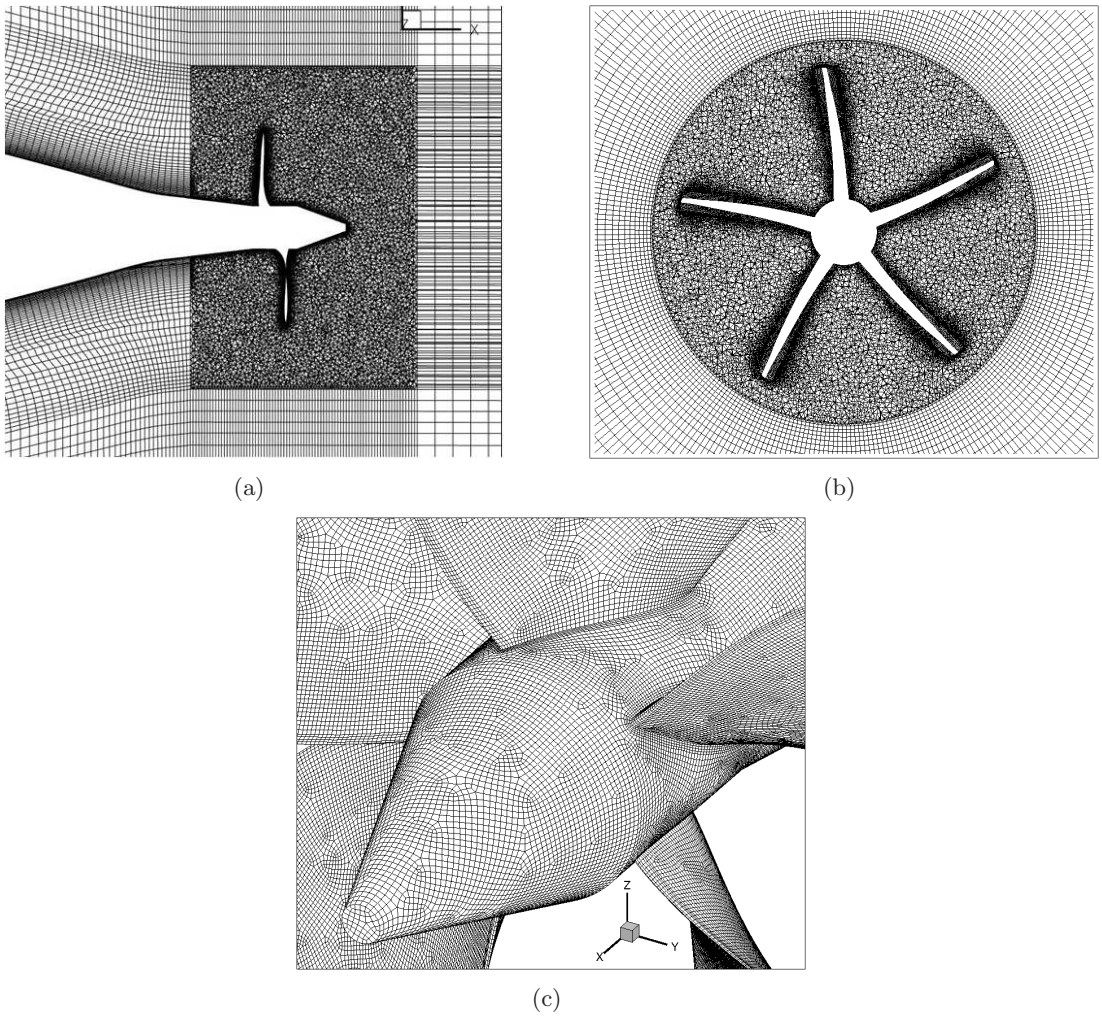

(a) (b)

(c)

Figure 3.4: Computational grid: (a) xy plane of grid for propeller with hull, (b) $x = 0$ plane of grid, (c) surface mesh.

The unstructured grid for the propeller with hull is shown in fig. 3.4. The surface of the propeller is meshed by quadrilateral elements. Four layers of prisms are extruded from the surface with a minimum wall–normal spacing of $0.0017D$ and a growth ratio of 1.05. A compact cylindrical region around the propeller is meshed with tetrahedral volumes while hexahedral volumes are used in the rest of the domain.

3.3 Results

Large Eddy Simulations are performed under the crashback condition at two negative advance ratios and Reynolds number $Re = 480,000$. The advance ratio J and Reynolds number Re are defined as

$$J = \frac{U}{nD}, \quad Re = \frac{UD}{\nu}$$

where U is the free-stream velocity, n is the propeller rotational speed, and D is the diameter of the propeller disk.

The notation used throughout the dissertation is as follows. Thrust T is the axial component of force, torque Q is the axial component of the moment of force, and F_H and F_V denote the horizontal and vertical components of the force respectively. The vector sum of F_H and F_V is the projection of the force onto the direction perpendicular to the propeller axis and is termed the side-force S. Since computations are performed in a rotating frame of reference, the side-force is transformed to the inertial reference frame. The horizontal and vertical components of the side-force, F_H and F_V, respectively, can be obtained from a rotational transformation using the angle between the rotating frame and the inertial frame.

Non-dimensional thrust coefficient K_T, torque coefficient K_Q and side-force magnitude coefficient K_S are given by

$$K_T = \frac{T}{\rho n^2 D^4}, \quad K_Q = \frac{Q}{\rho n^2 D^5}, \quad K_S = \frac{\sqrt{F_H^2 + F_V^2}}{\rho n^2 D^4},$$

where ρ is the density of the fluid. Henceforth, $\langle \cdot \rangle$ denotes the mean value and $\sigma(\cdot)$ denotes standard deviation. RMS of the side-force is defined as

$$\sigma(K_F) = \frac{1}{2}\big(\sigma(K_H) + \sigma(K_V)\big),$$

where

$$K_H = \frac{F_H}{\rho n^2 D^4}, \quad K_V = \frac{F_V}{\rho n^2 D^4}.$$

Side-force angle θ is defined as

$$\theta = tan^{-1}(\frac{F_V}{F_H}).$$

	$\langle K_T \rangle$	$\langle K_Q \rangle$	$\langle K_S \rangle$
LES [8]	-0.37	-0.074	0.023
WT [22]	-0.33	-0.065	0.024
OW [25]	-0.41	-0.078	

Table 3.1: **J=-0.7**. Mean values of thrust, torque and side-force magnitude given by previous computation and experiments.

Instead of using the advance ratio J, the experimental data of Bridges [9] and Bridges et al. [26] primarily use the similarity parameter η, defined as

$$\eta = \frac{n}{n_{sp}},$$

where n_{sp} is the propeller rotational speed for self–propulsion; which is the propeller speed at a given forward velocity such that the thrust produced by the propeller is equal to the drag of the vessel.

3.3.1 Propeller without hull at $J = -0.7$

The validity of the current LES methodology for propeller crashback is established by the LES of propeller without hull at $J = -0.7$ by Jang and Mahesh [8] which is in good agreement with the experimental results of Jessup et al. [22, 25]. Computed mean K_T and K_Q are located between 36 inch water tunnel (WT) and open water towing-tank (OW) results as shown in table 3.1. Fig. 3.5 shows that the computed circumferentially averaged flow fields also compare favorably with those measured with LDV by Jessup et al. [22]. Jang and Mahesh [8] also obtain frequency spectra of blade loads and time averaged velocity profiles to be in good agreement with experiment.

3.3.2 Effect of hull at $J = -1.0$

The flow for propulsor with and without hull at $J = -1.0$ is validated with available experimental data and then studied using time averaged flow statistics. This is followed by a physical mechanism to explain the occurrence of higher side-force in the presence of the hull in section 3.3.3.

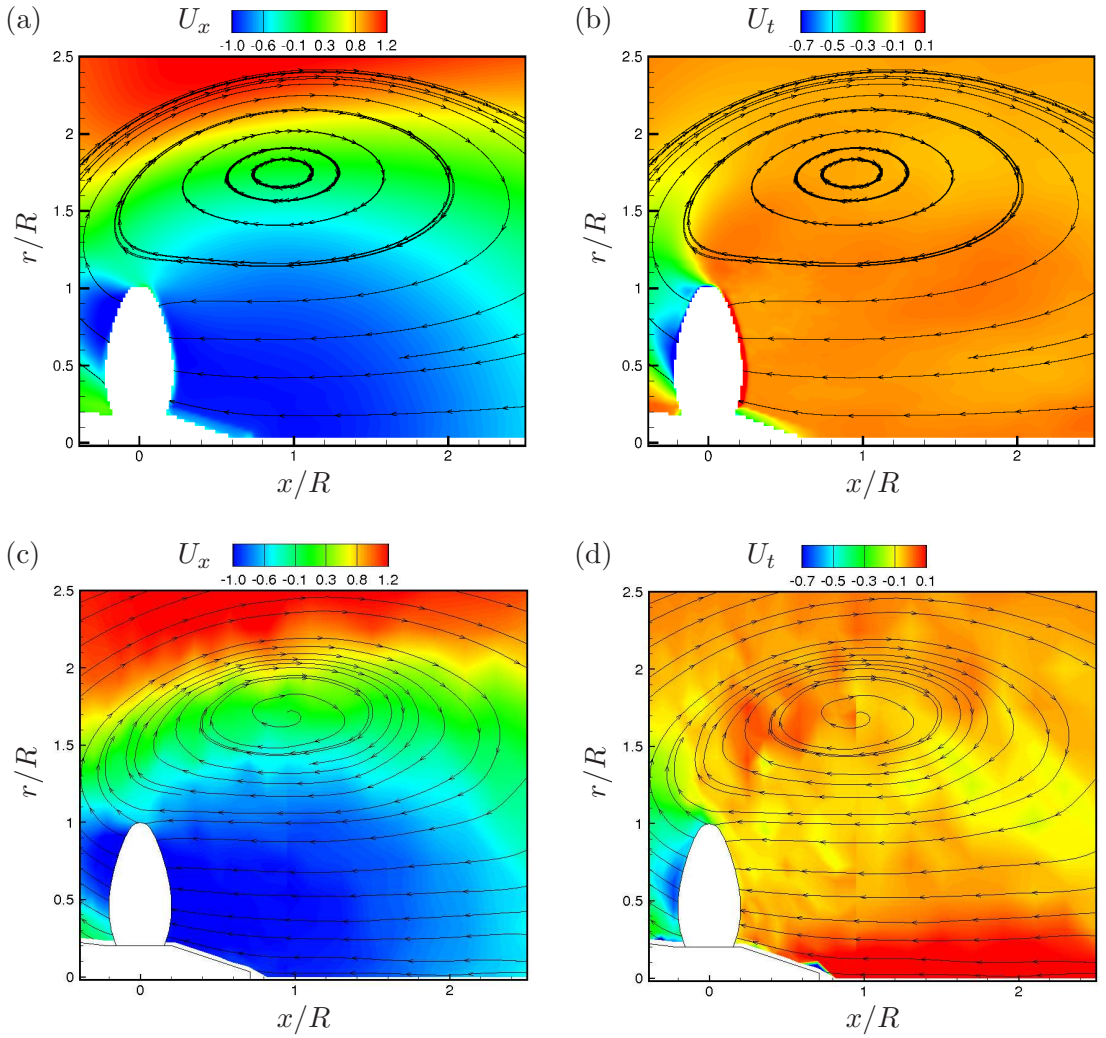

Figure 3.5: **J=-0.7**. Circumferentially averaged flow fields: (a) axial velocity and (b) tangential velocity (LES; [8]), (c) axial velocity and (d) tangential velocity (experiment; [22]).

Time history and spectra of loads

The time history of K_S shown in fig. 3.6 is over 259 propeller rotations for propeller with hull and 214 rotations without hull. The horizontal lines in fig. 3.6 are the mean and the mean plus or minus 1.5 times the standard deviation. $K_S - \sigma(K_S)$ represents low side-force magnitude and $K_S + \sigma(K_S)$ represents high side-force magnitude. As shown in table 3.2, computed mean and rms of side-force show agreement with the experimental

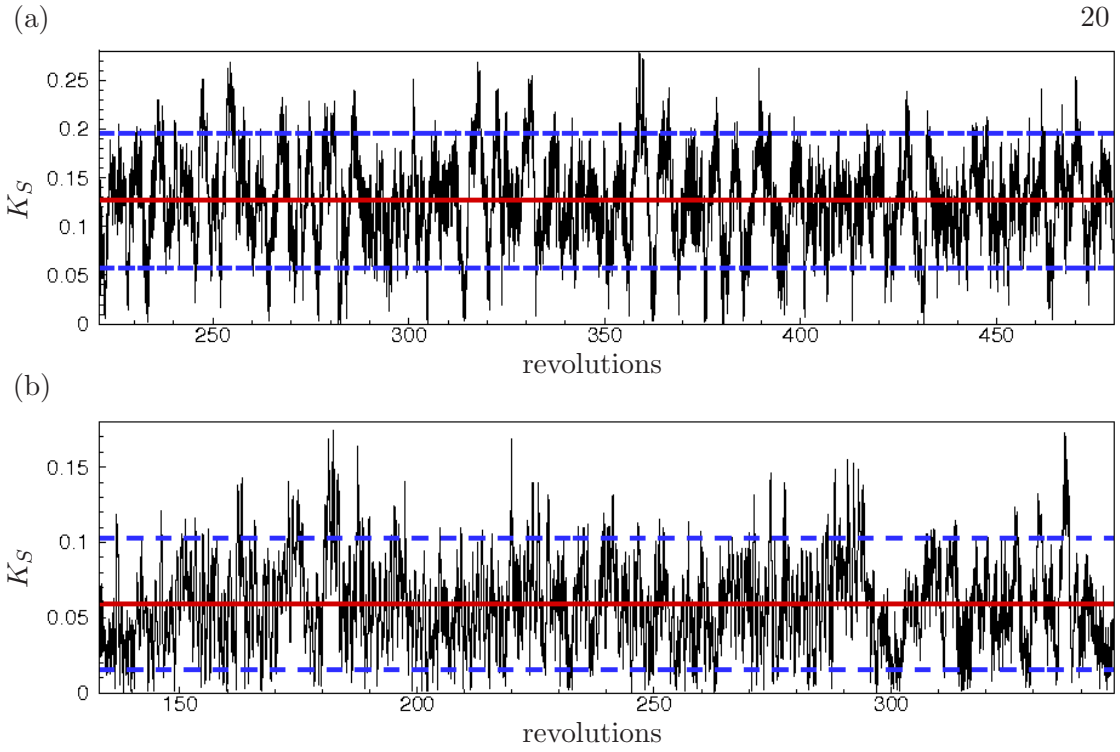

Figure 3.6: **J=-1.0**. Time history of unsteady loads on the propeller blades. —— $\langle K_S \rangle$, ---- $\langle K_S \rangle \pm 1.5\sigma(K_S)$; (a) w/ hull, (b) w/o hull.

		$\langle K_S \rangle$	$\sigma(K_F)$	$\sigma(K_S)$
Hull	LES	0.126	0.095	0.046
	Experiment [26]	0.105 - 0.126	0.096 - 0.104	0.042 - 0.047
Without Hull	LES	0.059	0.046	0.029
	Experiment [22]	0.036 - 0.052	-	0.022

Table 3.2: **J=-1.0**. Computed and experimental values of mean of side-force magnitude and rms of side-force on the blades with and without hull.

results for propeller with and without hull at $J = -1.0$. Very importantly, the LES predicts the experimentally observed increase in side-force in the presence of the hull. Table 3.3 compares the mean and rms of thrust and axial torque with available data.

The frequency spectra of the loads are computed by dividing the time history into a finite number of segments with 50% overlap, applying a Hann window for low aliasing and rescaling to maintain the input signal energy. Each such segment is then transformed into the frequency domain by taking a Fast Fourier Transform (FFT). The

		$\langle K_T \rangle$	$\sigma(K_T)$	$\langle K_Q \rangle$	$\sigma(K_Q)$
Hull	LES	-1.007	0.068	-0.188	0.013
	Experiment [26]	-0.835	0.173	-0.138	-
Without Hull	LES	-0.614	0.064	-0.116	0.011
	Experiment [22]	-0.64 – -0.53	0.059	-0.115 – -0.097	0.010

Table 3.3: **J=-1.0**: Computed and experimental values of mean and rms of thrust and axial torque on the blades with and without hull.

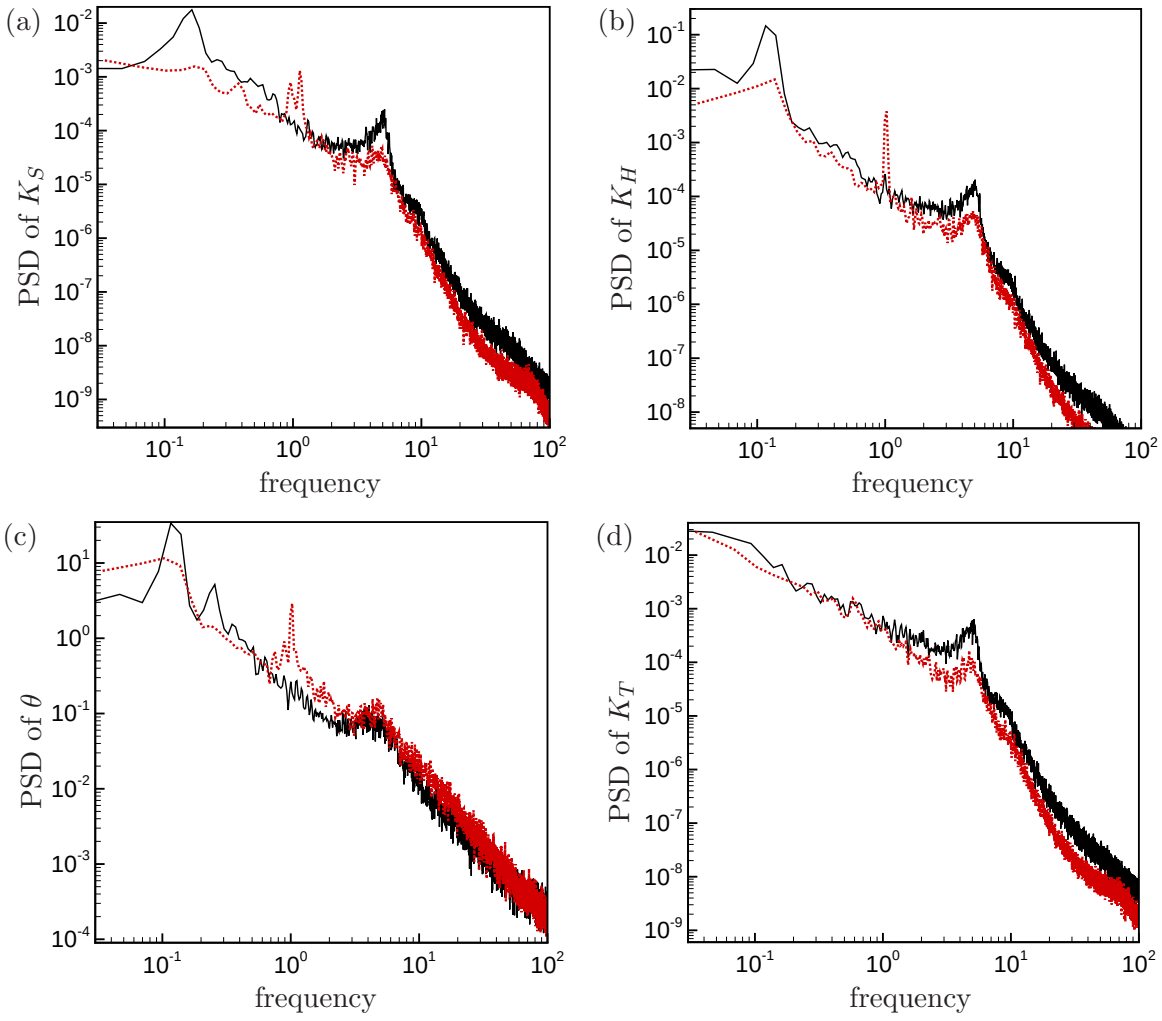

Figure 3.7: **J=-1.0**. Power spectral density: —— w/ hull, ---- w/o hull; (a) K_S, (b) K_H, (c) θ, (d) K_T.

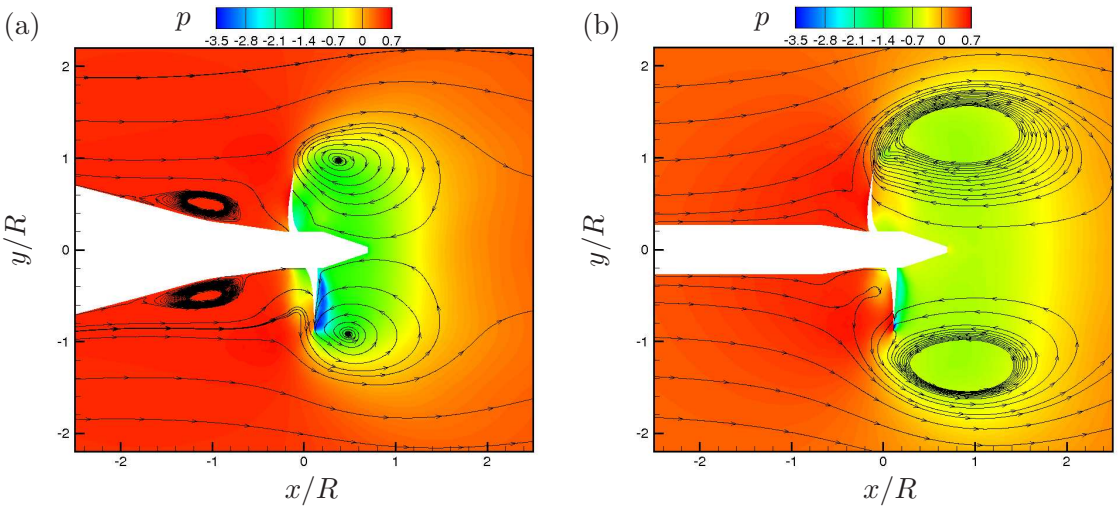

Figure 3.8: **J=-1.0**. Time averaged pressure contours with streamlines: (a) w/ hull, (b) w/o hull.

power spectral density (PSD) is then averaged over all the segments to provide a relatively smooth curve. Fig. 3.7 shows the PSD of the coefficient of side-force magnitude K_S, horizontal force K_H, side-force angle θ and torque K_T with and without hull. The most important peak is at $f = 5\ rev^{-1}$ which has also been observed by Vyšohlid and Mahesh [5],Chang et al. [6] and Jang and Mahesh [8]. This corresponds to the passage of the blades of the five-bladed propeller. Note that the magnitude of this peak is higher in presence of the hull.

A low frequency, high amplitude modulation of the side-force has important ramifications for the maneuverability of the vessel. For the K_S spectra in fig. 3.7(a), there is a peak at a lower frequency of $f = 0.16\ rev^{-1}$ with the hull. It must be noted that Bridges et al. [26] report a non-dimensional frequency of peak propeller horizontal force at $\eta = -0.9$ to be $f \sim 0.12\ rev^{-1}$. This agrees well with a low frequency of $f = 0.11\ rev^{-1}$ seen for K_H (fig. 3.7(b)). Note that $\eta = -0.9$ in Bridges et al. [26] approximately corresponds to $J = -1.0$. The corresponding low frequency peak without the hull is at $f = 1\ rev^{-1}$, in agreement with experiments [22]. Only the non-axial force quantities (K_H, K_V, K_S, θ) exhibit these low frequencies as they are absent for K_T and K_Q.

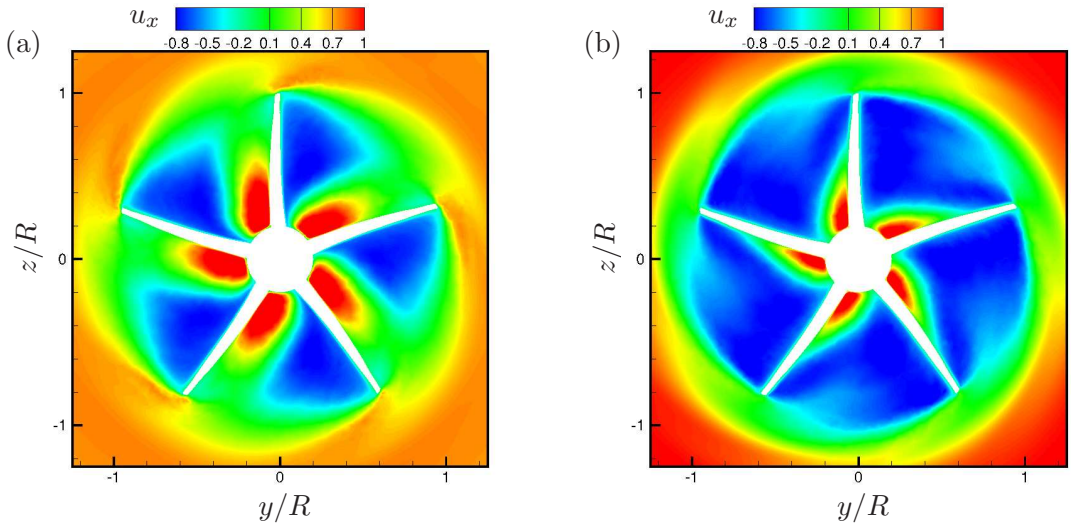

Figure 3.9: **J=-1.0**. Time averaged axial velocity at $x/R = 0$: (a) w/ hull, (b) w/o hull.

Time averaged flow field

Time averaged statistics of flow field are computed over 170 propeller rotations for propeller with hull and 172 rotations without hull which is included in the time window for which the time history of K_S is shown. Figure 3.8 shows an xy plane slice cutting the center and along the length of the shaft/hull. Time averaged pressure contours and velocity streamlines are plotted. Flow features distinguishing the presence of the hull are clearly observed. The velocity streamlines in fig. 3.8 reveal a recirculation zone upstream of the blades in the presence of the hull. No such recirculation zone appears near the shaft without hull. This region of high circulation is created by the interaction between the wake of the hull and reverse flow produced by propeller rotation. In the presence of the hull, the vortex ring appears to be more compact and its center is closer to the blades compared to the more elongated and stretched out vortex ring without the hull. The suction side of the blades with the hull see lower levels of pressure than without hull. Reverse rotation also causes reverse flow without the hull. However in this case, the flow interacts with a freestream which enters the propeller disk with higher momentum than the hull wake.

Fig. 3.9 illustrates the effect of the hull on axial velocity in the yz plane at the x-location $x/R = 0$. The perspective in these figures is such that the hull/shaft are

going into the plane of the paper and the freestream is coming out of the plane of the paper. It can be inferred that reverse flow decreases between the propeller blades with hull but note that the velocity becomes higher near the root of the blades. This point will be re-inforced in fig. 3.12 in the next section.

Circumferentially averaged flow field

The time averaged flow statistics are further averaged along lines of constant radius to yield circumferentially averaged statistics in the $x - r$ plane. Fig. 3.10 compares the circumferentially averaged fields obtained from LES with the LDV data available from Bridges et al. [26] at $\eta = -0.877$. The LDV field in the experiment excludes a rectangular region around the propeller. The grid used to obtain the LDV data is coarse and the data clearly lacks adequate samples for averaging. Fig. 3.11 shows contours of axial velocity with streamlines with and without hull. The blanked out zone is where the hull/shaft and the propeller blade would be. The upstream recirculation zone is nestled between the blades and the rising contours of the hull centered at the coordinates $(x/R, r/R) \equiv (-1.03, 0.51)$. Note that the vortex ring is much closer to the tip of the blade when the hull is present. The wake of the hull has lower streamwise momentum which causes the vortex ring to form closer to the blade when a hull is present. There is also increased reverse flow entering the propeller disk in the absence of a hull. Table 3.4 compares the locations of the center of the vortex ring with and without hull obtained using the current LES. The distances are measured relative to the propeller center. Table 3.5 shows good agreement for the distance of the center of the vortex ring between LES and experiment at $\eta = -0.9$ [see 9].

Axial velocity profiles are extracted from six x-locations spanning one radius upstream to half a radius downstream of the blade. The solid line is for the propeller with hull while the dotted line is without hull. Fig. 3.12 clearly shows the difference that the presence of a hull makes. Lower velocity is observed for $r/R > 1.4$ at all x-locations in the presence of the hull. This supports our assertion that lower momentum of the incoming upstream flow causes the center of the vortex ring to be located closer to the blades with hull. The first of these locations ($x/R = -1.0$) passes close to the center of the recirculation region ($x/R = -1.03$) in the simulation with hull and the velocity profile at this location is shown in fig. 3.12(a). The velocity profile with hull clearly

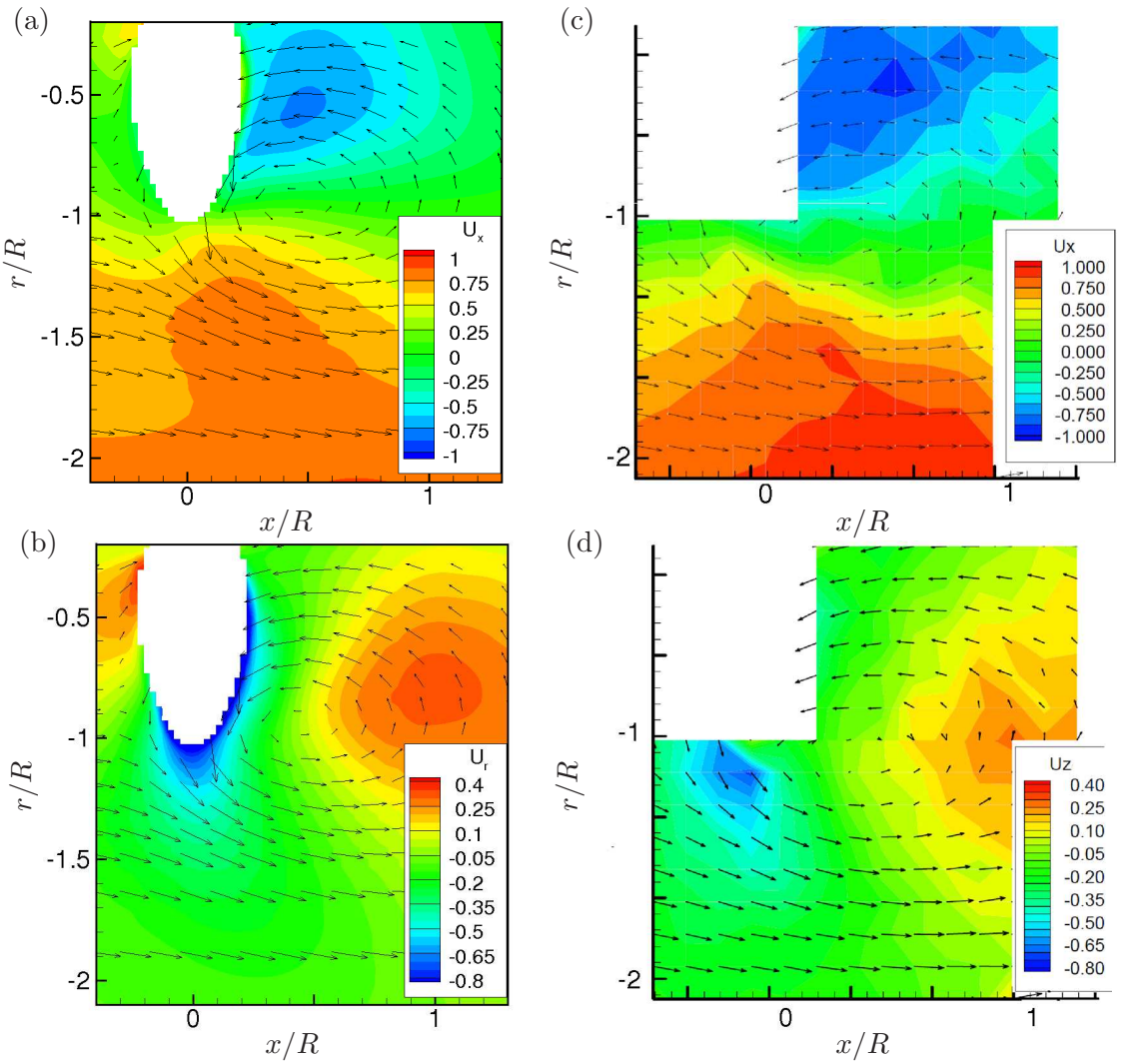

Figure 3.10: **J=-1.0**. Circumferentially averaged flow fields (a) axial velocity and (b) radial velocity (LES), (c) axial velocity and (d) tangential velocity (experiment; [9]).

indicates a low momentum velocity profile compared to without hull, almost similar to that obtained behind a backward-facing step close to the center of the primary vortex [see 27]. In fact, there is even a slight reverse velocity close to the hull body ($r/R < 0.5$). Not surprisingly, this is close to the center of the recirculation zone. Fig. 3.12(c) shows that in the near-field of trailing edge of the blade at ($x/R = -0.2$), the blade root ($r/R < 0.4$) sees a higher velocity with the hull. This is consistent with higher velocity near the blade root as seen in fig. 3.9(a). Without the hull, figs. 3.12(d)-(f) clearly

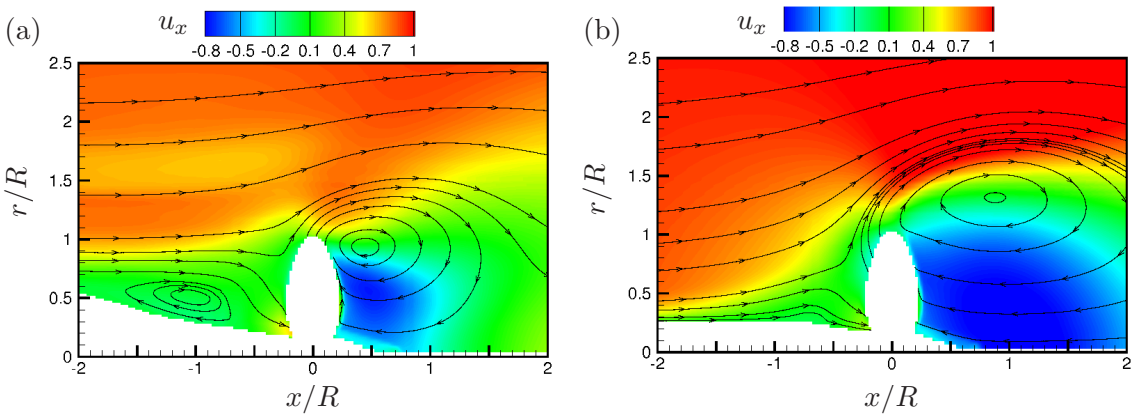

Figure 3.11: **J=-1.0**. Circumferentially averaged axial velocity with streamlines: (a) w/ hull, (b) w/o hull.

	x_{cen}/R	r_{cen}/R
Hull	0.45	0.94
Without hull	0.88	1.32

Table 3.4: **J=-1.0**. Locations of centers of vortex rings with and without hull from circumferentially averaged flow fields.

Hull	d_{cen}/R
LES	1.04
Experiment [9]	1.10

Table 3.5: **J=-1.0**. Distance of center of vortex ring from LES and experiment with hull.

show increased reverse inflow from downstream into the propeller disk. The closer vortex ring is responsible for the rather high velocity gradient with hull in fig. 3.12(e) near $0.7 < r/R < 0.9$. The line plot for u_x at $(x/R = 0.45)$ shown in fig. 3.12(f) passes through the center of the vortex ring with the hull.

Fig. 3.13(a) shows smaller outward radial velocity near the tip of the blade with the hull, thus pulling the center of the vortex ring closer to the blade. However, fig. 3.13(c) shows that the radial velocity near the leading edge of the blade $(x/R = 0.2)$ is much higher with hull due to induction by the closer vortex ring. Fig. 3.14 compares tangential velocity profiles with and without hull. It is useful to note that the blade

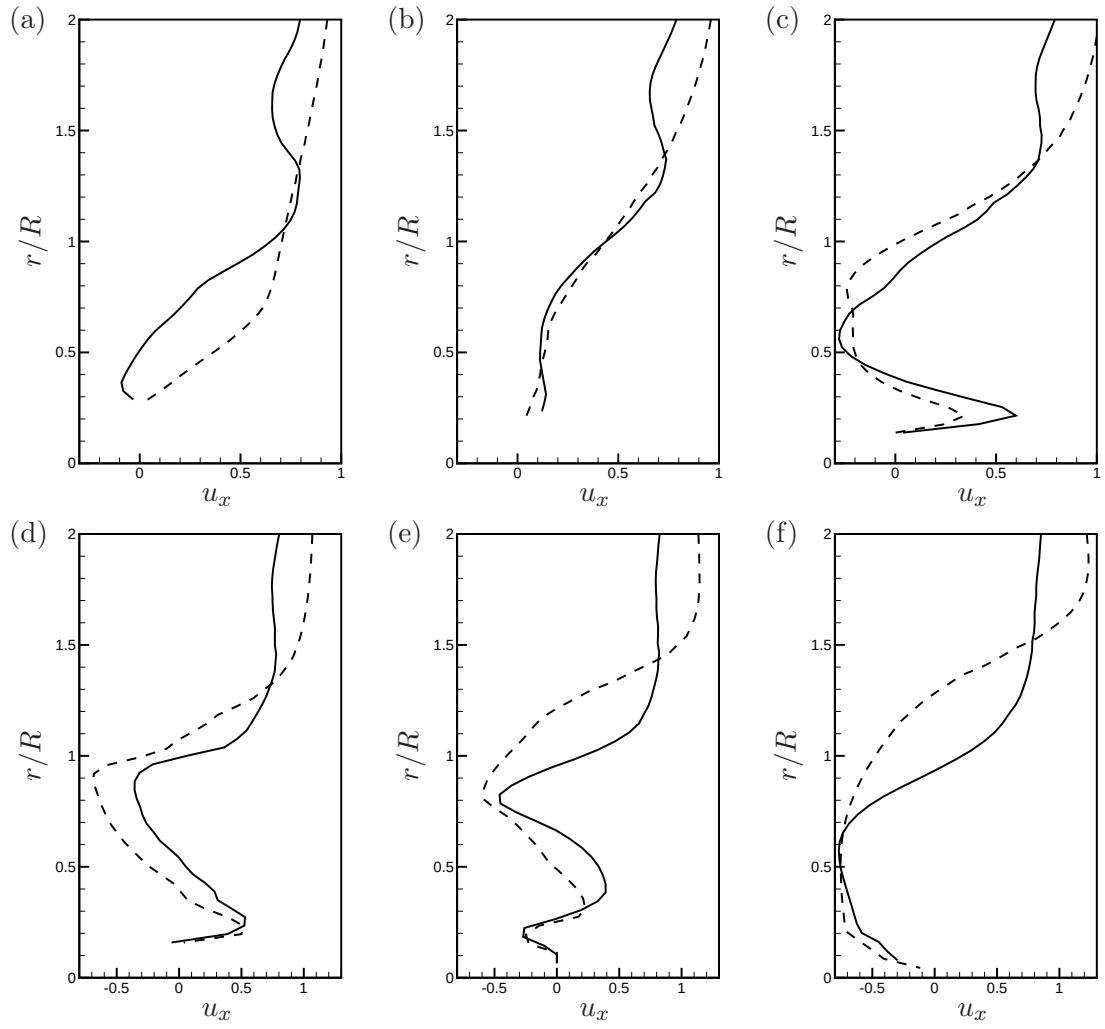

Figure 3.12: **J=-1.0**. Circumferentially averaged axial velocity profiles from 6 x-locations: —— w/ hull, −−− w/o hull; (a) $x/R = -1.0$, (b) $x/R = -0.5$, (c) $x/R = -0.2$, (d) $x/R = 0.0$, (e) $x/R = 0.2$, (f) $x/R = 0.45$.

tangential velocity $u_\theta = \pi(r/R)/J$ at any radial section r/R on the blade surface. Mean u_θ is primarily negative due to the reverse propeller rotation in crashback. The tangential velocity is always higher in the presence of the hull within the blade passage ($x/R = 0.0$) and near the leading edge of the blades ($x/R = 0.2$). In fig. 3.14(b), the slope of the solid line (w/hull), denoting u_θ, is almost π/J indicating that the flow tends to move along with the blade tangential velocity. It will be shown in section 3.3.3 that

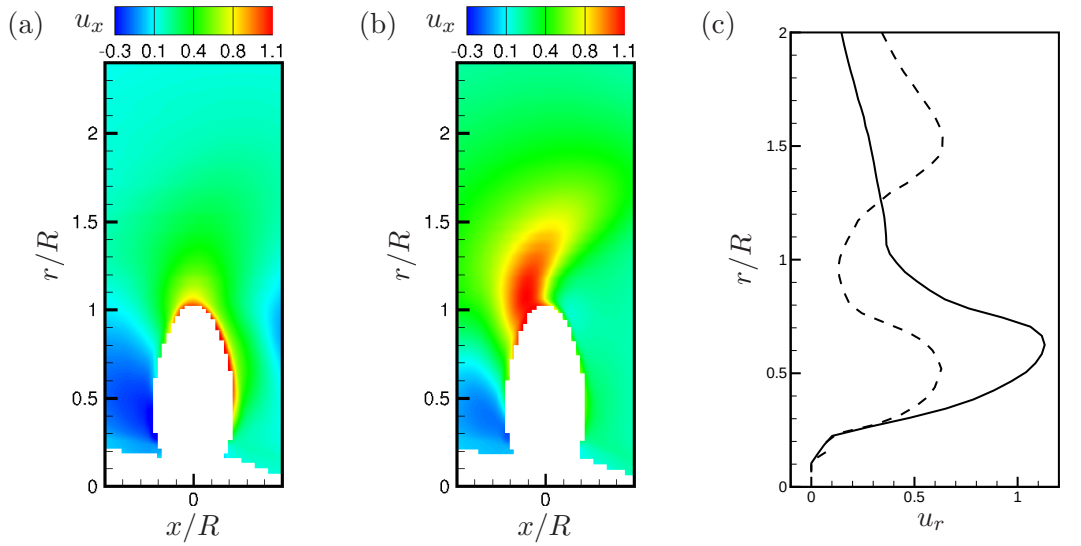

Figure 3.13: **J=-1.0**. Circumferentially averaged radial velocity. Contours: (a) w/ hull, (b) w/o hull. (c) Profile from $x/R = 0.2$, —— w/ hull, −−− w/o hull.

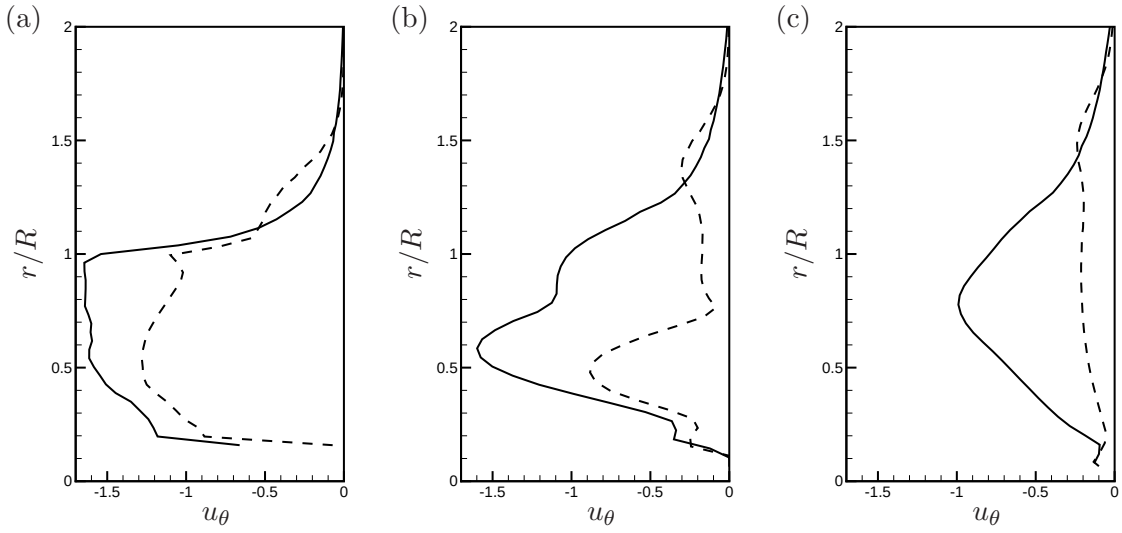

Figure 3.14: **J=-1.0**. Circumferentially averaged tangential velocity profiles from 3 x-locations: —— w/ hull, −−− w/o hull; (a) $x/R = 0.0$, (b) $x/R = 0.2$, (c) $x/R = 0.45$.

the leading edge of the blade (around $x/R = 0.2$) is a region of great flow separation. The swirl is so much higher with the hull that it persists even at a downstream distance of ($x/R = 0.45$) whereas it is almost absent without hull.

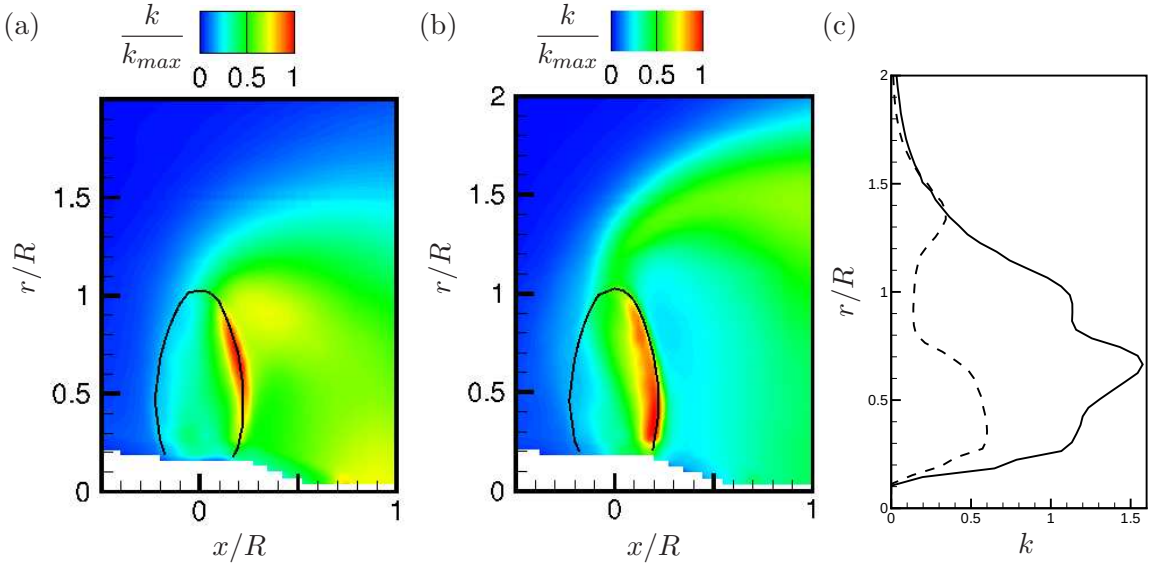

Figure 3.15: **J=-1.0**. Circumferentially averaged turbulent kinetic energy. Contours for $\frac{k}{k_{max}}$: (a) w/ hull, (b) w/o hull. (c) k profile from $x/R = 0.2$, —— w/ hull, −−− w/o hull.

Turbulent kinetic energy (k) is a measure of three-dimensional unsteadiness and turbulence in the flow. Figs. 3.15(a)-(b) show k normalized by the maximum turbulent kinetic energy k_{max} in each case. With hull, $k_{max} = 1.6$ whereas $k_{max} = 0.6$ without hull. Hence, k is much higher in the presence of hull. In figs. 3.15(a)-(b), the solid line outlines where the propeller blade would be. It is observed that k is highest near the leading edge of the blades for both the cases, possibly related to the unsteadiness caused by the reverse flow separating at the sharp leading edge. There are two important effects of the hull worth mentioning (fig. 3.15(a)). Firstly, k is relatively high in the near-field of the blade ($0.2 < x/R < 0.5$) and this is directly attributable to greater unsteadiness stirred up by the closer unsteady vortex ring. Secondly, the distribution of k near the leading edge is highest in the outward half of the propeller blade ($r/R > 0.5$) compared to the inward half ($r/R < 0.5$) of the blade without hull. This can be seen more clearly in the line plot of k obtained from the leading edge (fig. 3.15(c)) where maximum k occurs near $r/R \sim 0.65$ with hull and $r/R \sim 0.3$ without hull. Also, the magnitude of this maximum k with hull is almost three times that without hull. Thus, it can be concluded that a greater peak velocity fluctuation acting through a greater moment arm

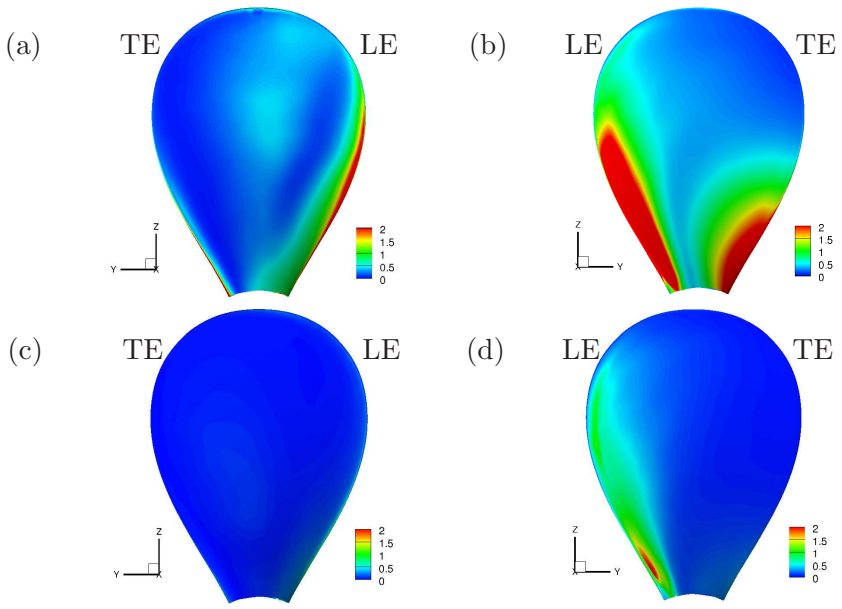

Figure 3.16: **J=-1.0**. Pressure contribution to side-force on (a) pressure side w/ hull, (b) suction side w/ hull, (c) pressure side w/o hull, (d) suction side w/o hull.

must exert greater forces and moments on the propeller.

Propeller loads

At high Reynolds numbers, viscous effects are smaller in comparison to pressure effects. Hence pressure force is the dominant term in blade loadings. Jang and Mahesh [8] introduced a quantity for pressure contribution to side-force magnitude (F_S) on a unit surface which is

$$F_S = \sqrt{F_H^2 + F_V^2} = \sqrt{(\vec{F}\cdot\vec{j})^2 + (\vec{F}\cdot\vec{k})^2} = |p|\sqrt{(\vec{n}_f\cdot\vec{j})^2 + (\vec{n}_f\cdot\vec{k})^2} = |p|\beta_f \qquad (3.2)$$

where p is the pressure, $\vec{n}_f$ is the outward normal vector of the face, $\vec{j}$ and $\vec{k}$ are base unit vectors in the plane normal to the axial direction. β_f is invariant with rotation and hence compatible with our rotating system. $|p|\beta_f$ is the pressure contribution to side-force magnitude K_S and $\sigma(p)\beta_f$ is the pressure contribution to rms of side-force $\sigma(K_F)$.

$\sigma(p)\beta_f$ on the propeller blades is examined in fig. 3.16 to reveal the location of

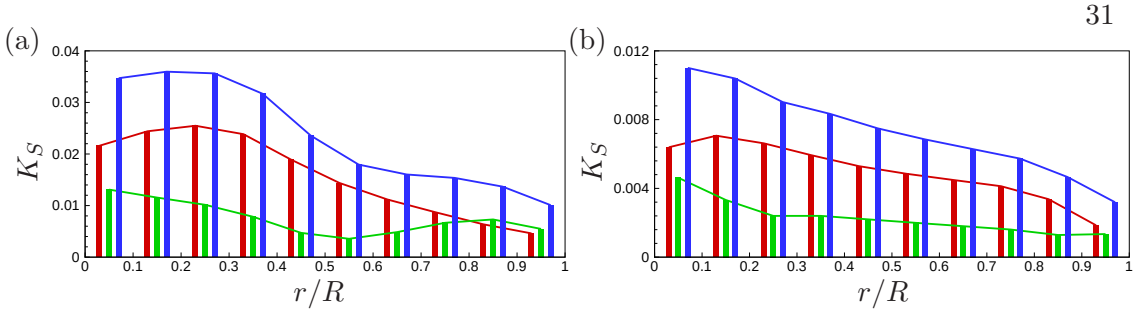

Figure 3.17: **J=-1.0**. Side-force magnitude loading on blade-sections: —— suction side, —— pressure side, —— total on blade; (a) w/ hull, (b) w/o hull.

generation of side-force at $J = -1.0$. For clarification, the face of the propeller blade towards the incoming hull wake or freestream is the pressure side and the other face towards the reverse flow is the suction side. Fig. 3.16 shows that the pressure contribution to side-force is significantly higher with hull. On the pressure side, propeller with hull (fig. 3.16(a)) has higher $\sigma(p)\beta_f$ than without hull (fig. 3.16(c)), especially on the leading edge. The biggest pressure contribution to the side-force, though, comes from the suction side. As had been observed by Jang and Mahesh [8] at $J = -0.7$, the leading edge on the suction side is responsible for most side-force without hull (fig. 3.16(d)). This observation can now also be extended to $J = -1.0$ with hull (fig. 3.16(b)). In fact, with hull, even the trailing edge on suction side shows pressure contribution to side-force. A closer look at the trailing edge of the suction reveals that most of the pressure contribution towards side-force comes from near the blade root.

The above observations are re-inforced more quantitatively in fig. 3.17. The blade surface is divided into ten constant-radius sections. The mean side-force magnitude experienced by these ten sections on both the pressure and suction sides of the blade are plotted as histograms. The force is averaged over 59 rotations for propeller with hull and 55 rotations without hull. Note the higher relative magnitude of K_S for the case with hull (fig. 3.17(a)) than without hull (fig. 3.17(b)). For both cases, the pressure side generates lesser side-force than the suction side. Most of the side-force is generated from close to the blade root without hull. However, with the hull, the blade area upto $r/R = 0.4$ is responsible for high side-force magnitude. This blade root-ward trend in the radial location of generation of high side-force is in contrast with the more traditional elliptical blade loading for K_T with a peak around $r/R = 0.7$.

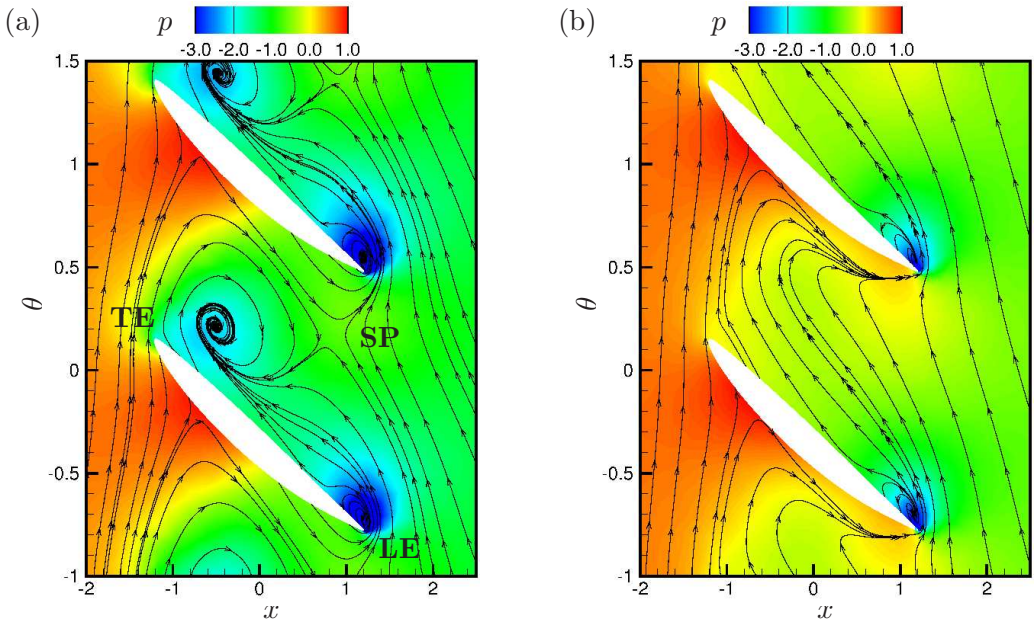

Figure 3.18: **J=-1.0**. Time averaged pressure field with streamlines at a constant radial plane of $r/R = 0.4$: (a) w/ hull, (b) w/o hull.

3.3.3 Mechanism of higher side-force with hull

In order to understand the mechanism behind the generation of higher side-force at the leading and trailing edge of the blades with hull, a closer look is taken at the flow around blade sections. Fig. 3.18 shows time averaged pressure field with streamlines at a constant radial plane of $r/R = 0.4$. This radial plane shows flow past blade sections, allowing an examination of the blade passage as well. Here the inflow is from left to right and propeller blades rotate in the direction of negative θ in the crashback mode. The leading and trailing edges are denoted on the figure. It is observed that the LE for propeller with hull (fig. 3.18(a)) shows lower pressure than without hull (fig. 3.18(b)). In fact, there is a low pressure region even on the TE with hull. Streamlines reveal a separation region in all these locations of low pressure.

Fig. 3.19 attempts to explain the existence and formation of the separation zones near the TE and LE of the blades with hull. It has been established earlier (in secs. 3.3.2 and 3.3.2) that the axial velocity near the blade root with hull is greater than without hull. This would imply a higher incoming flow towards the TE of the blade

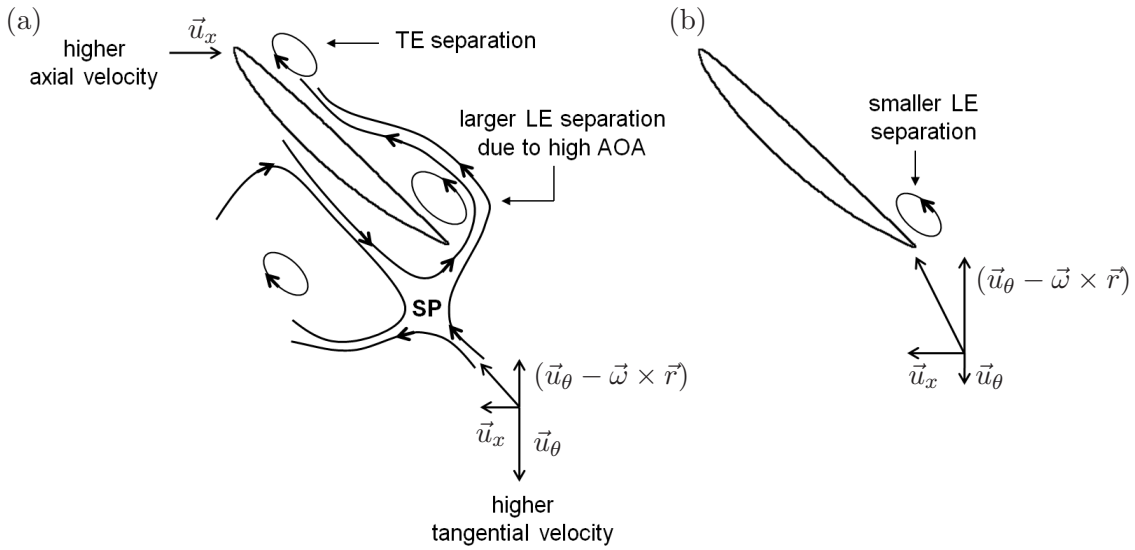

Figure 3.19: **J=-1.0**. Schematic to explain formation of separation zones on blades near blade root for propeller: (a) with hull, (b) without hull.

near the blade root, resulting in a TE separation zone with hull as is seen in 3.18(a).

Even though the LE of the blade with hull sees a lower reverse (negative) axial velocity ($\vec{u}_x$) than without hull, it does however see higher radial and tangential velocities (ref to secs. 3.3.2 and 3.3.2). The velocity vector $\vec{v}$ in the radial plane in the rotating frame of reference is formed by $\vec{v} = \vec{u}_x + (\vec{u}_\theta - \vec{\omega} \times \vec{r})$ where $\vec{\omega}$ is the rotational rate of the blades and $\vec{r}$ is the radial vector to the radial plane about the center of rotation (propeller hub). A higher $-\vec{u}_x$, combined with lower $-\vec{u}_\theta$ makes $\vec{v}$ more akin to a backing condition inflow to the blades. This rather benign backing-type reverse inflow is what impinges on the LE of the blades without hull, causing a small LE separation region (fig. 3.18(b)). The reverse inflow seen by the LE of the blades with hull deviates from this. To compound matters further, the TE separation region affects the flow pattern inside the blade passage in such a way that a saddle point (SP) is formed (3.18(a)). The streamlines emerging from SP appear to impinge the LE of the blades with hull at a very high angle of attack, leading to a larger LE separation region.

The TE separation region with hull might serve another purpose than just to aid in the formation of a saddle point. It is probable that this separation region traps fluid within the blade passage. This confined fluid is then more likely to rotate with the

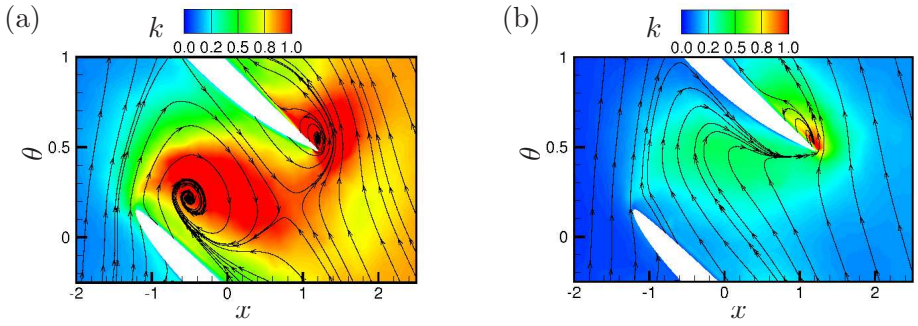

Figure 3.20: **J=-1.0**. Time averaged turbulent kinetic energy field with streamlines at a constant radial plane of $r/R = 0.4$: (a) w/ hull, (b) w/o hull.

blades. Evidence of this is obtained from fig. 3.14(a) where the tangential velocity of the flow with hull closely follows the tangential velocity of a blade section ($\vec{\omega} \times \vec{r}$; not shown) till $r/R < 0.5$. $\vec{\omega} \times \vec{r}$ varies linearly from $(u_\theta, r/R) \equiv (0, 0)$ to $(-1.57, 0.5)$. This implies that the tangential flow in the rotational frame of reference ($\vec{u}_\theta - \vec{\omega} \times \vec{r}$) is essentially stationary in the mean. But this fluid trapped within the blade passage is still very unsteady instantaneously and leads to high turbulent kinetic energy as shown in fig. 3.20(a).

To summarize, propeller blades in the presence of a hull have greater LE separation, existence of a TE separation region and possibly trapped fluid within the blade passage. LE separation directly contributes to higher side-force originating on the suction and pressure side of the LE. TE separation is responsible for higher side-force originating on the suction side of the TE. Higher levels of turbulent kinetic energy within the blade passage and in the near-field of the blades also contributes to higher side-force.

3.3.4 Effect of hull at $J = -0.5$

Simulations are performed for the propeller with and without hull at $J = -0.5$. $J = -0.5$ is chosen because it is higher than the critical advance ratio of $J = -0.7$ mentioned by Jessup et al. [25]. According to the experiments the presence of an upstream hull is not expected to make much of a difference to the performance of the propeller in crashback at this advance ratio.

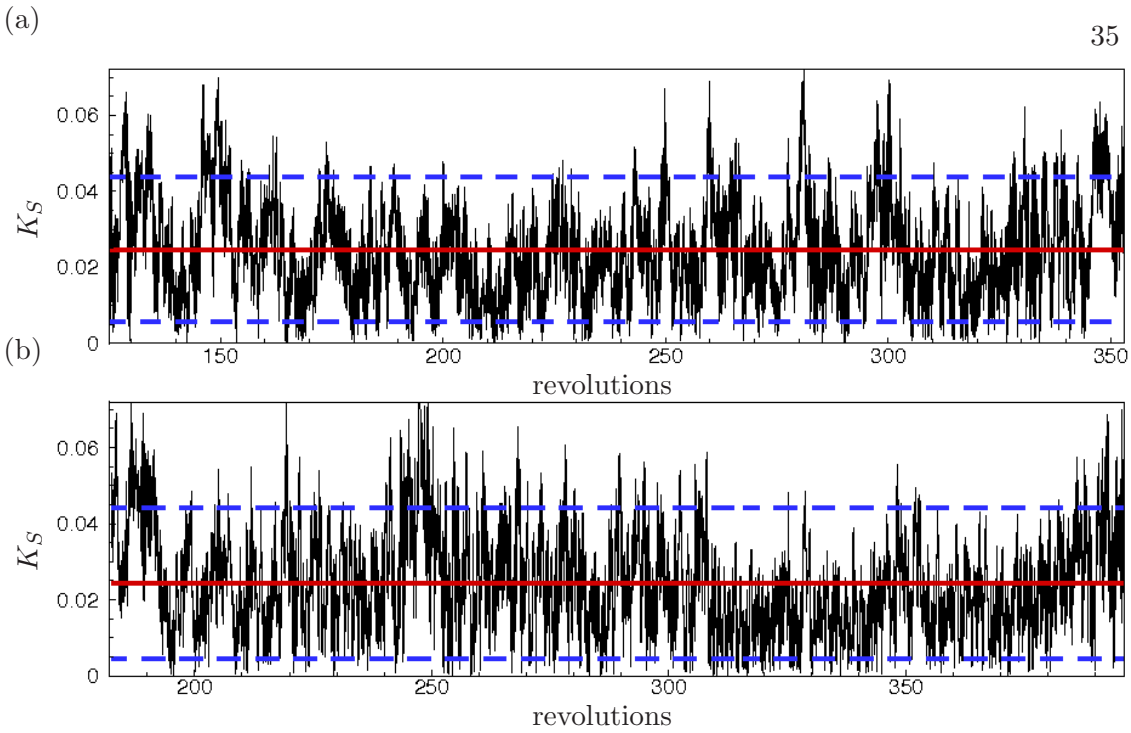

Figure 3.21: **J=-0.5**. Time history of unsteady loads on the propeller blades. —— $\langle K_S \rangle$, ---- $\langle K_S \rangle \pm 1.5\sigma(K_S)$; (a) w/ hull, (b) w/o hull.

Time history and spectra of loads

The time history of K_S shown in fig. 3.21 is over 228 propeller rotations for propeller with hull and 214 rotations without hull. The horizontal lines in fig. 3.21 are $K_S \pm 1.5\sigma(K_S)$. Table 3.6 shows that consistent with experiments, for the current LES, the hull does not significantly affect the mean of the side-force magnitude and rms of side-force at $J = -0.5$. Also the computed quantities for side-force are in agreement with the experiments. Table 3.7 compares the mean and rms of thrust and axial torque with available data.

Fig. 3.22 shows the PSD of the coefficient of side-force magnitude K_S and thrust K_T with and without hull. The blade passage peak at $f = 5\ rev^{-1}$ is again observed as it has been in previous computations and experiments. Noticeably, this peak is more prominent than at $J = -1.0$. The magnitude of this peak is not significantly higher in presence of the hull. A low frequency at $f = 1\ rev^{-1}$ is observed without hull for K_S but not with K_T, similar to the LES at $J = -1.0$ and experiments (see section

		$\langle K_S \rangle$	$\sigma(K_F)$	$\sigma(K_S)$
Hull	LES	0.025	0.020	0.013
	Experiment [26]	0.030	0.025 – 0.031	0.015 – 0.022
Without Hull	LES	0.025	0.020	0.013
	Experiment [22]	0.025 - 0.033	-	0.017

Table 3.6: **J=-0.5**. Computed and experimental values of mean of side-force magnitude and rms of side-force on the blades with and without hull.

		$\langle K_T \rangle$	$\sigma(K_T)$	$\langle K_Q \rangle$	$\sigma(K_Q)$
Hull	LES	-0.259	0.042	-0.052	0.008
	Experiment [9]	-0.307	0.061	-0.070	-
Without Hull	LES	-0.302	0.051	-0.061	0.010
	Experiment [22]	-0.033 – -0.27	0.056	-0.065 – -0.057	0.011

Table 3.7: **J=-0.5**: Computed and experimental values of mean and rms of thrust and axial torque on the blades with and without hull.

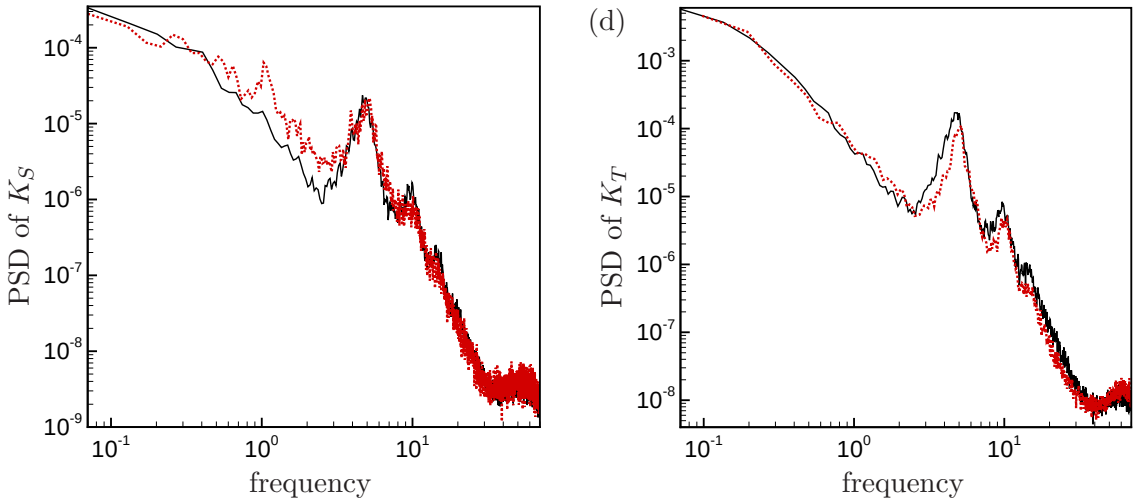

Figure 3.22: **J=-0.5**. Power spectral density: —— w/ hull, ---- w/o hull; (a) K_S, (b) K_T.

3.3.2). Higher harmonics at $f = 10, 15\ rev^{-1}$ are also visible at this advance ratio but are significantly lower in amplitude.

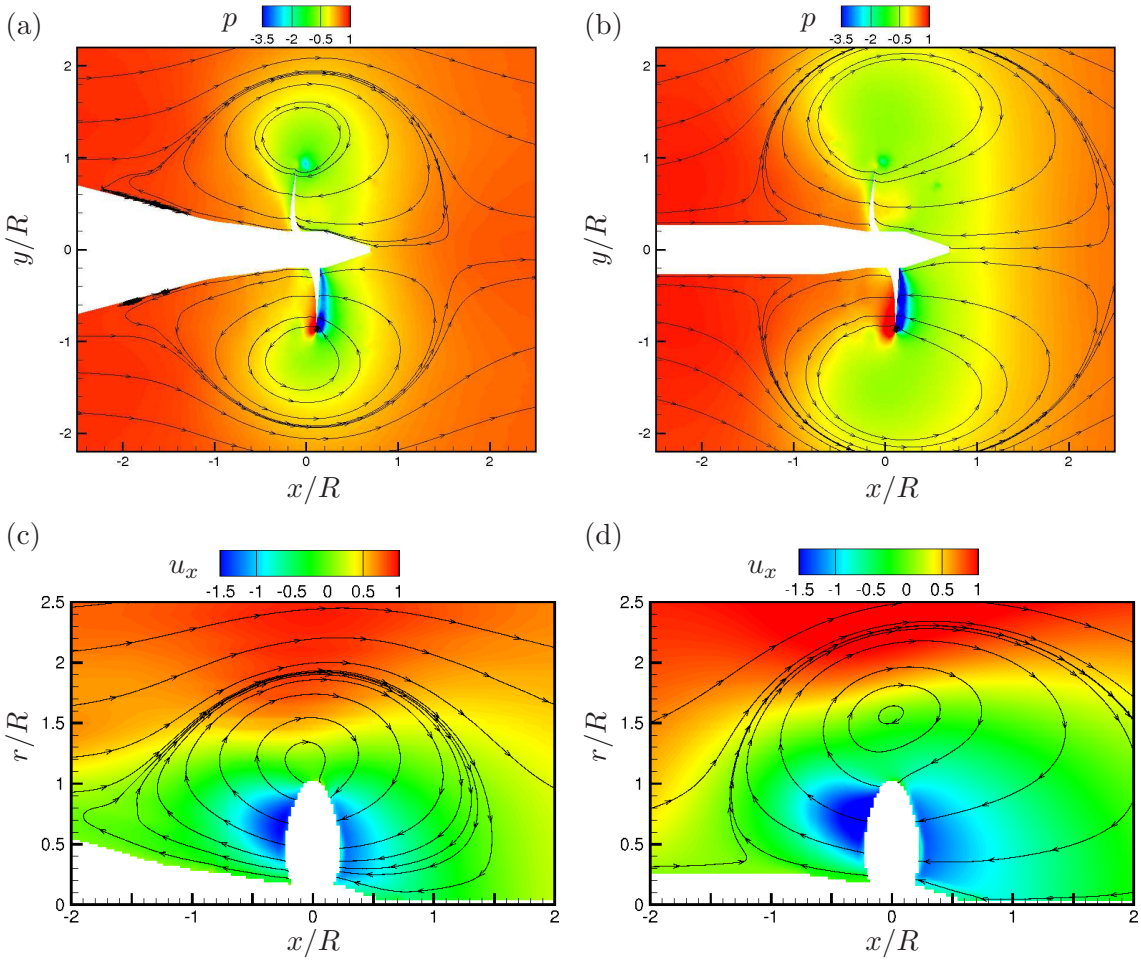

Figure 3.23: **J=-0.5**. Time averaged pressure contours with streamlines: (a) w/ hull, (b) w/o hull; Circumferentially averaged axial velocity with streamlines: (c) w/ hull, (d) w/o hull.

Time averaged flow field

The time averaged statistics shown in fig. 3.23 are computed over 153 rotations for propeller with the hull and 200 rotations without hull. Figs. 3.23(a)-(b) show the time averaged pressure contours with streamlines. Note that compared to fig. 3.8 earlier for $J = -1.0$, there is a much smaller recirculation zone and it is located further upstream of the blades now. The vortex ring is also located closer to the blades. Figs. 3.23(c)-(d) show that there is only a slight radially inward displacement in the location of the center

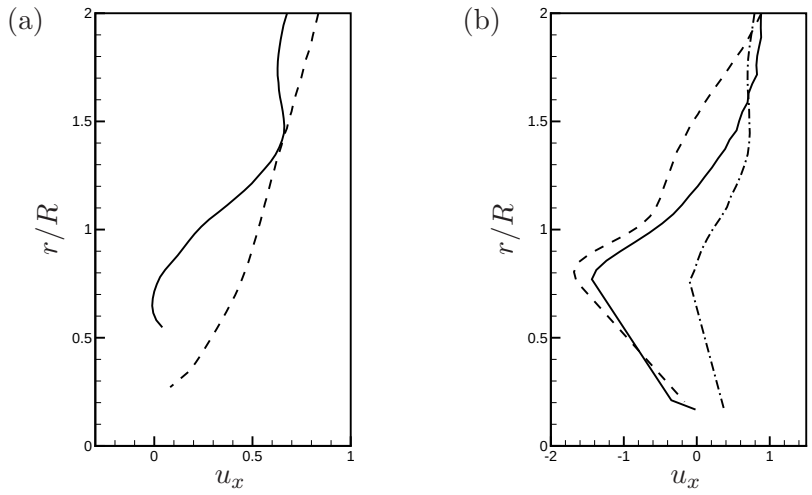

Figure 3.24: Axial velocity profiles from two x-locations upstream of the blades; $J = -0.5$: —— w/ hull, −−− w/o hull; $J = -1.0$: —·— w/ hull; (a) $x/R = -2.0$, (b) $x/R = -0.2$.

of the vortex ring with hull. Importantly, it is observed that the propeller blades see a higher velocity reverse flow compared to that at $J = -1.0$ and this increased reverse flow extends from about a radius downstream of the blades to about a radius upstream.

Fig. 3.24 shows the effect of the hull on the axial velocity profiles at $J = -0.5$. The profile is taken at an x-location ($x/R = -2.0$) upstream on the hull/shaft which passes through the small recirculation zone when the hull is present. Note the similarity of this profile to fig. 3.12(a) which was also taken at an x-location which passed through the center of the recirculation zone for $J = -1.0$. Fig. 3.24(b) shows axial velocity profiles in the near-field of the propeller blades ($x/R = -0.2$). The velocity profile for propeller with hull at $J = -1.0$ (dash-dotted here; solid in fig. 3.12) is also plotted along with those with and without hull at $J = -0.5$. Note that in the near-field of the blades, the hull does not make much of a difference till the blade radius ($r/R < 1$) at $J = -0.5$ and the axial velocities are much more negative than in the presence of the hull at $J = -1.0$. Compared to fig. 3.11(a), this was not the case at $J = -1.0$ where immediately upstream of the blades, the wake of the hull interacts with the reverse flow to produce the recirculation zone. Also, looking at fig. 3.11(a), it can be said that even without the influence of the hull, the reverse flow is not strong enough to extend

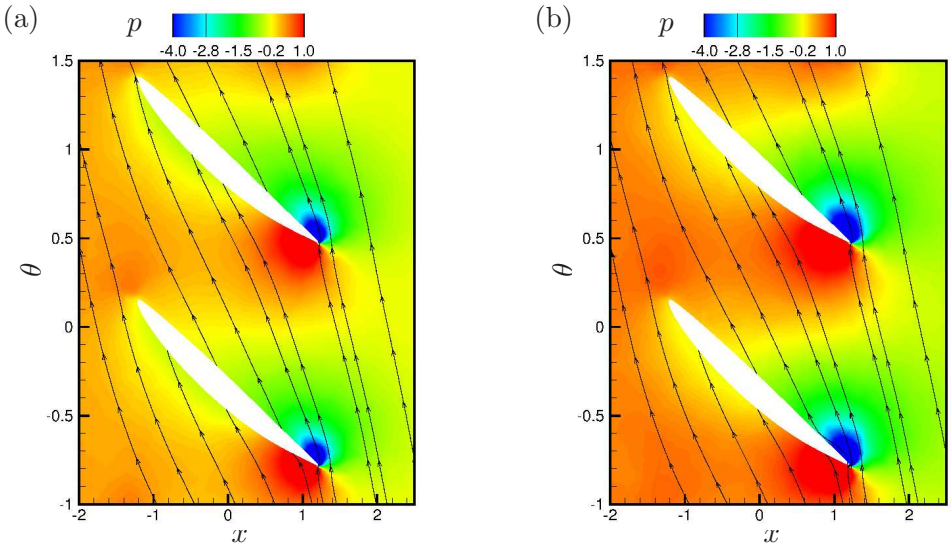

Figure 3.25: **J=-0.5**. Time averaged pressure field with streamlines at a constant radial plane of $r/R = 0.4$: (a) w/ hull, (b) w/o hull.

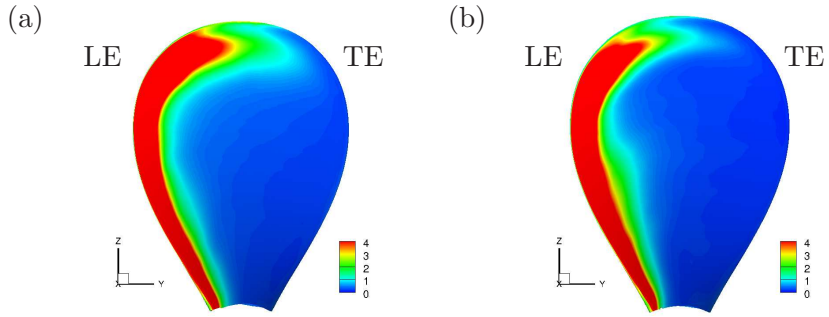

Figure 3.26: **J=-0.5**. Pressure contribution to side-force on suction side (a) w/ hull, (b) w/o hull.

upstream beyond the blades.

As has been explained earlier in section 3.3.3, a recirculation zone and closer vortex ring ultimately leads to greater separation on the TE and LE respectively on the suction side of the blade. At $J = -0.5$, the vortex ring is relatively close to the blades and this causes separation on the LE of the suction side leading to the low pressure region seen in fig. 3.25. But there is no corresponding low pressure region on the TE with hull and this could be attributed to the absence of the recirculation region. Since there is no TE separation, the flow inside the blade passage essentially continues along the direction

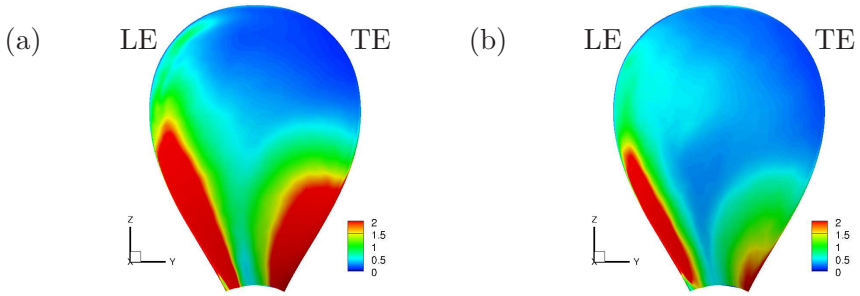

Figure 3.27: **J=-1.0**. Pressure contribution to side-force w/ hull on suction side; during (a) high K_S, (b) low K_S.

of the reverse flow and doesn't get trapped. Fig. 3.26 shows that at $J = -0.5$, the distribution of pressure contribution to side-force is almost the same for both with and without hull. Most of the pressure contribution to side-force comes from the LE on the suction side. The TE of the blade with hull does not provide any higher side-force as it did at $J = -1.0$.

3.3.5 High and low amplitude events

The propeller blades are subject to a wide range of loads during crashback. Being an off-design condition, the blades must be able to withstand extreme structural loading during the duration of this maneuver. Hence studying the extreme loading events is essential from the perspective of performance and structural robustness. However it is also useful in understanding the relative significance of flow features during different loading conditions. Chang et al. [6] tried to explain the physics of crashback by investigating high and low amplitude loading events. They looked at instantaneous snapshots of the flow field during the extreme events to give a qualitative understanding of those events. Jang and Mahesh [8] used the technique of conditional averaging [28] to give a more quantitative picture of the physics of crashback for a propeller without hull during extreme loading events. Conditionally sampled flow fields are analyzed in the current section to reveal the impact of the recirculation region and vortex ring towards production of extreme thrust and side-force in the presence of a hull at $J = -1.0$ and $J = -0.5$.

Firstly, the flow field is conditionally averaged at $J = -1.0$ with hull for $K_S \pm$

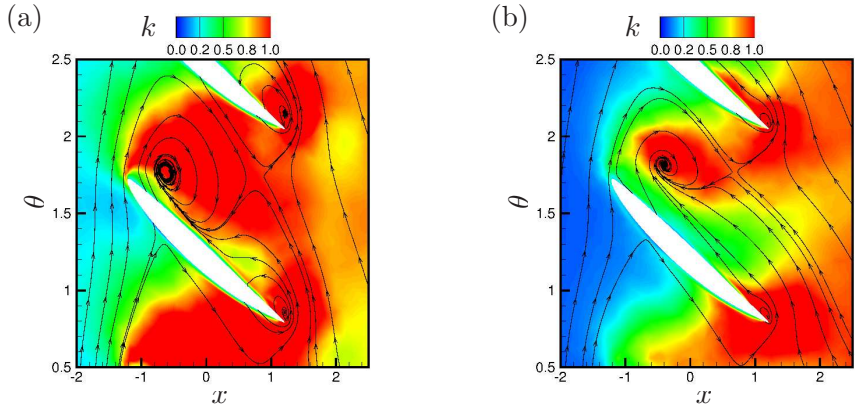

Figure 3.28: **J=-1.0**. Turbulent kinetic energy field with streamlines at a constant radial plane of $r/R = 0.4$ w/ hull during (a) high K_S, (b) low K_S.

$1.5\sigma(K_S)$ to represent high and low side-force events. Time averaged conditional statistics of flow field are computed over 65 propeller rotations which is included in the time window for which the time history of K_S is shown in 3.6(a). Fig. 3.27 shows that the location of generation of higher side-force during high K_S events is consistent with fig. 3.16. Though not shown here, the pressure side LE has slightly more contribution during high K_S events but most of the side-force originates from the suction side.

Noticeably, TE of the suction side plays a greater role during high K_S events. This points towards greater TE separation leading to higher TE unsteadiness as shown in fig. 3.28. Also note the higher LE unsteadiness as is to be expected during high K_S events. Greater TE separation in the presence of a hull at $J = -1.0$ was ascribed to higher axial velocity near the blade root in section 3.3.2. That assertion is re-affirmed through fig. 3.29 which shows the axial velocity profiles at different x-locations leading upto the blade. The axial velocity during high K_S events is always higher below $r/R = 0.5$. It is believed that a slightly upstream recirculation region allows the flow to accelerate through a larger axial distance to cause a higher axial velocity in the near-field of the propeller blades. Table 3.8 shows that the recirculation region is located slightly further upstream (x_{cen}/R is lesser) and is also slightly bigger in size (r_{cen}/R is greater) during high K_S events. Lower side-force originating from the suction side LE during low K_S events is due to lesser LE separation which is consistent with greater reverse flow (which reduces the angle of attack as shown in section 3.3.3). This greater reverse flow during low K_S events is also apparent from fig. 3.29 at $x/R = 0$. In fact, the TE

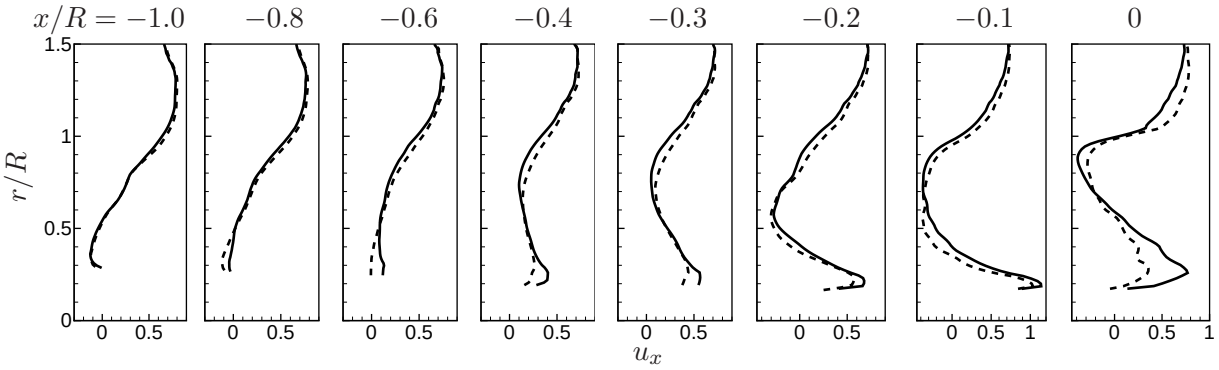

Figure 3.29: **J=-1.0**. Circumferentially averaged axial velocity profiles from 8 x-locations leading upto the blades w/ hull. —— : high K_S, ---- : low K_S.

	x_{cen}/R	r_{cen}/R
High K_S	-1.101	0.549
Low K_S	-0.996	0.529

Table 3.8: **J=-1.0**. Location of center of recirculation region w/ hull during (a) high K_S, (b) low K_S.

is also responsible for higher K_T during high K_S events. It can be concluded that the recirculation region near the inflow of the propeller blades plays a greater role towards generation of high forces at $J = -1.0$.

The flow field is conditionally averaged at $J = -0.5$ with hull. At this advance ratio, thrust and side-force are correlated. More particularly, high and low thrust events are correlated with high and low side-force events respectively, as shown in table 3.9. To demonstrate that this is also the case with hull, results are shown with conditionally averaging at $J = -0.5$ with hull for $K_T \pm 1.5\sigma(K_T)$ to represent high and low thrust events over 47 propeller rotations which is included in the time window for which the time history of K_S is shown in 3.21(a). Fig. 3.30 shows that both the thrust and side-force are higher during the high K_T events when compared with the low K_T events. Consistently, most of the side-force is generated from the LE of the suction side and hence is attributable to greater LE separation.

There is a very small recirculation region far upstream on the hull during high K_T(fig. 3.31) located at $x_{cen}/R = -2.15$. During low K_T, it is almost absent and could be located further upstream at $x_{cen}/R = -2.75$. But even during high K_T, the

	$J = -1.0$	$J = -0.5$
w/ Hull	0.443	-0.304
w/o hull	-0.247	-0.353

Table 3.9: Correlation for $\langle K_S K_T \rangle$ on propeller blades.

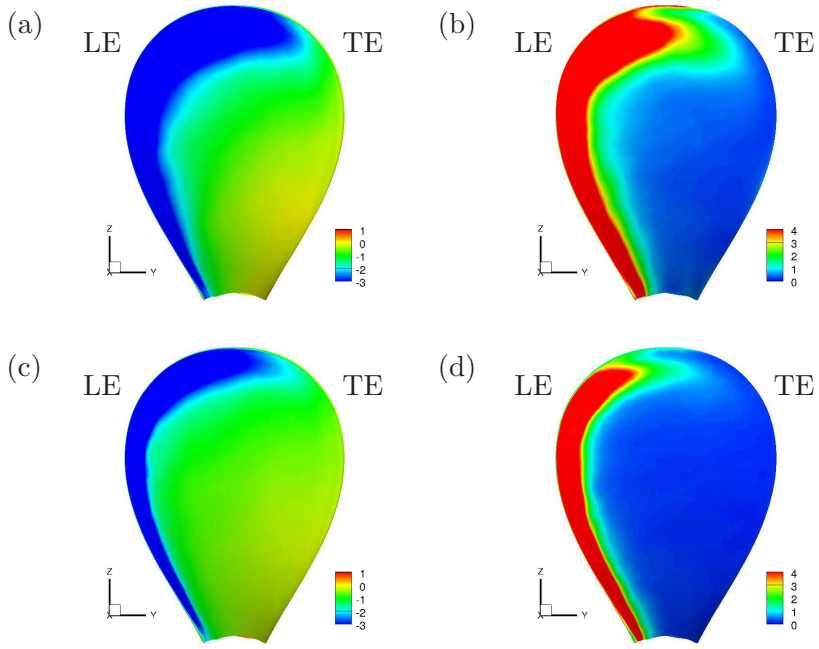

Figure 3.30: **J=-0.5**. Pressure contribution to thrust and side-force w/ hull on the suction side during : high K_T (a) thrust, (b) side-force; low K_T (c) thrust, (d) side-force.

recirculation region is far upstream to have any effect near the TE of the blade root as it does at $J = -1.0$. As expected from the absence of appreciable side-force generated from the TE on the suction side of the blade, there is no noticeable TE separation. It can be concluded that the recirculation region does not impact the flow in the near-field of the propeller blades at $J = -0.5$.

Figs. 3.31(a)-(b) also show that for high K_T, the center of the vortex ring is located closer to the tip of the propeller blades as listed in table 3.10. Higher unsteadiness is observed near the tip and LE of the blade (figs. 3.31(c)) which translates into relatively higher forces near the blade tip during high K_T (and K_S) events. Thus proximity of

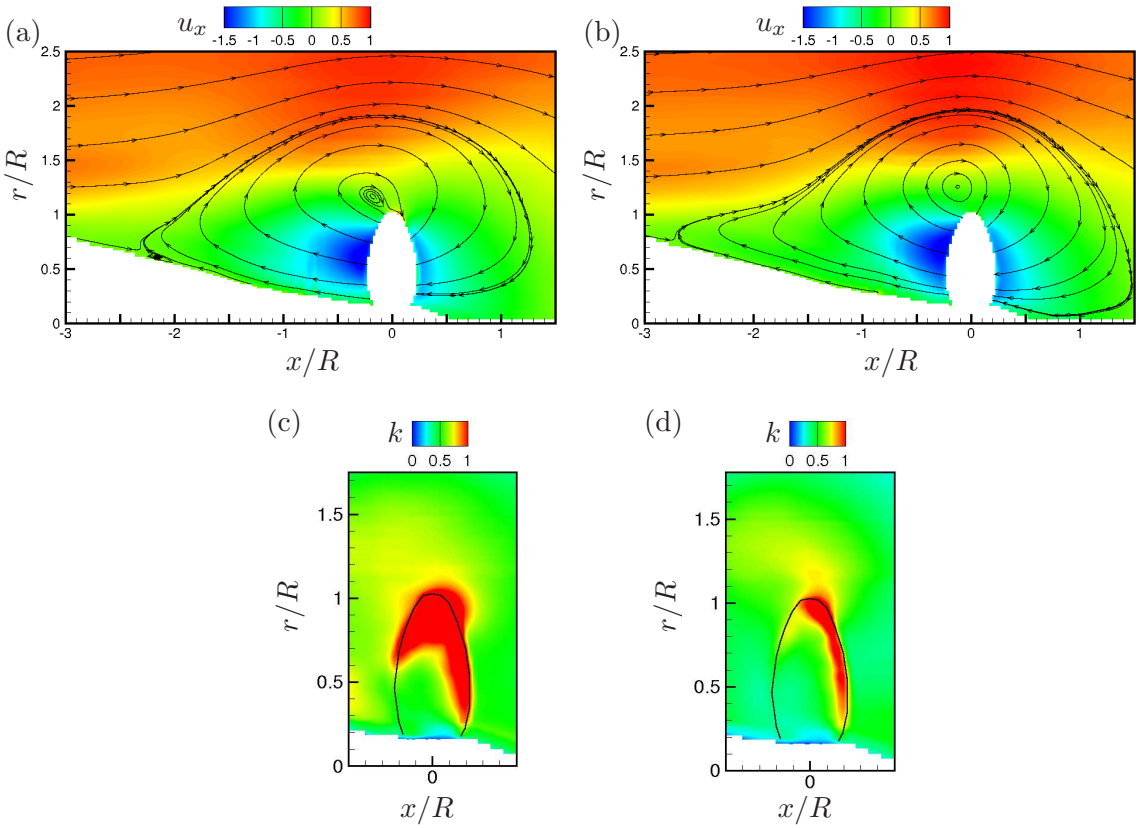

Figure 3.31: **J=-0.5**. Circumferentially averaged field w/ hull: Axial velocity with streamlines for (a) high K_T, (b) low K_T; Turbulent kinetic energy for (c) high K_T, (d) low K_T.

	$J = -1.0$	$J = -0.5$
High K_T	0.988	1.178
Low K_T	1.009	1.268

Table 3.10: Distance of center of vortex ring from the center of the propeller w/ hull during high and low K_T events at $J = -1.0$ and $J = -0.5$.

the vortex ring to the propeller blades plays a greater role towards generation of higher forces at this advance ratio.

Table 3.10 also points out that the vortex ring is closer at $J = -1.0$ than at $J = -0.5$. However, there is only a slight difference between high and low K_T at $J = -1.0$. This re-affirms that even though a closer vortex ring will lead to higher forces at any advance

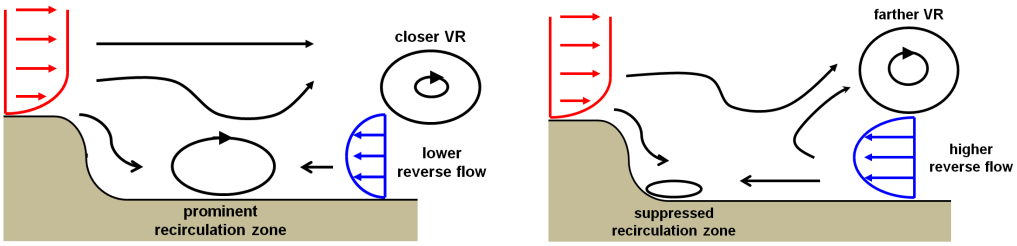

(a) (b)

Figure 3.32: **J=-0.5**. Schematic to explain flow in the presence of a hull at (a) high negative advance ratio ($J = -1.0$), (b) low negative advance ratio ($J = -0.5$).

ratio, it is not as dominant a mechanism of force generation at $J = -1.0$ as it is at $J = -0.5$. This can also be gauged by observing that the outboard half of the blade is not the major contributor to side-force at $J = -1.0$.

3.4 Mechanism of different side-force at different advance ratios with hull

The above results suggest the following model to explain the mechanism of different side-force at different advance ratios (fig 3.32). At lower negative advance ratio, such as $J = -0.5$, the higher rotational rate of the propeller blades causes a higher reverse flow into the blades. Higher reverse flow is closer to an attached flow like condition and hence LE separation is small compared to $J = -1.0$. This reverse flow also interacts with the hull at a greater upstream distance from the propeller, thus suppressing the recirculation zone. Velocities upstream of the blades are still high enough and so the vortex ring does not form too close to the blades as expected, with the hull. As a result, the hull does not make much of a difference to the flow in the near-field of the blades when the propeller rotation rate is higher which is same as a lower negative advance ratio. Hence results with and without hull are very similar at $J = -0.5$.

Whereas, at a higher negative advance ratio like $J = -1.0$, the reverse flow is not high enough. This causes larger LE separation compared to $J = -0.5$ and a recirculation zone forms upstream of the blades with the hull. The close recirculation region accelerates the flow approaching the blades from the pressure side. This causes

a closer vortex ring but much more importantly, TE separation near the root of the blade. The near-field of the blades is affected to the extent of causing higher side-force at a higher negative advance ratio.

3.5 Summary

Crashback simulations for a propeller with and without hull have been performed at the advance ratios $J = -0.5$ and $J = -1.0$. According to Bridges' experiment [9] with an upstream hull, side-force increase dramatically as J is reduced below -0.7. At both advance ratios, computed mean, rms and spectra of side-force show reasonable agreement with the experimental data for both with and without hull. At $J = -1.0$, two new noticeable flow features are found with the hull. A recirculation zone is found to exist upstream of the propeller blades and the center of the vortex ring is located much closer to the blades. The presence of the recirculation zone decreases the momentum of the flow which causes the vortex ring to be located closer to the blades. The recirculation zone and the closer vortex ring alter the flow in the near-field of the propeller blades with hull. At $J = -0.5$, the upstream recirculation zone with the hull is suppressed because the reverse flow from propeller rotation is higher and there is not much difference in the location of vortex ring with and without hull. The pressure contribution to side-force with hull is significantly higher than without hull at $J = -1.0$. For both advance ratios, the side-force with hull is mostly generated from leading edge separation on suction side. However, at $J = -1.0$, higher side-force is also generated from trailing edge separation on suction side. At $J = -1.0$, propeller blades with hull have greater LE separation, existence of a TE separation region and possibly trapped fluid within the blade passage. LE separation directly contributes to higher side-force originating on the suction and pressure side of the LE. TE separation is responsible for higher side-force originating on the suction side of the TE. Higher levels of turbulent kinetic energy within the blade passage and in the near-field of the blades also contributes to higher side-force. At low negative advance ratios ($J = -0.5$), the vortex ring is the dominant flow feature affecting blade forces through suction side LE. At high negative advance ratios ($J = -1.0$), the recirculation region is an additional and more dominant flow feature increasing blade forces through the suction side TE.

Chapter 4

Lagrangian SGS Model with Dynamic Lagrangian Time Scale

4.1 Background

Without any kind of averaging, the local dynamic model (eq. 2.14) is known to predict a highly variable eddy viscosity field. More so, the eddy viscosity can be negative, which causes solutions to become unstable. It was found that C_s has a large auto-correlation time which caused negative eddy viscosity to persist for a long time, thereby causing a divergence of the total energy [29]. Hence averaging and/or clipping C_s (setting negative values of C_s to 0) was found to be necessary to stabilize the model. Positive C_s from eq. 2.14 provides dissipation thereby ensuring the transfer of energy from the resolved to the subgrid scales. Also, clipping is almost never required when averaging over homogenous directions. Ghosal et al. [30] showed this averaging and/or clipping operation to be essentially a constrained minimization of eq. 2.12.

However the requirement of averaging over at least one homogeneous direction is impractical for complex inhomogeneous flows. To circumvent the problems of lack of homogeneous direction(s) and undesirable clipping, Ghosal et al. [30] proposed a 'dynamic localization model (k-equation)' to allow for backscatter by including an equation for subgrid scale kinetic energy budget. Ghosal's formulation entails further computational expense as well as additional model coefficients. To enable averaging in inhomogeneous flows, Meneveau et al. [11] developed a Lagrangian version of DSM (LDSM) where C_s is

averaged along fluid trajectories. Lagrangian averaging is physically appealing considering the Lagrangian nature of the turbulence energy cascade [31, 32]. Meneveau et al. [11] provide further justifications about the validity of averaging and the motivation for Lagrangian averaging.

In essence, the Lagrangian DSM attempts to minimize the pathline average of the local GIE squared. The objective function to be minimized is given by

$$E = \int_{pathline} \epsilon_{ij}(\mathbf{z})\epsilon_{ij}(\mathbf{z})d\mathbf{z} = \int_{-\infty}^{t} \epsilon_{ij}(\mathbf{z}(t'),t')\epsilon_{ij}(\mathbf{z}(t'),t')W(t-t')dt' \tag{4.1}$$

where $\mathbf{z}$ is the trajectory of a fluid particle for earlier times $t' < t$ and W is a weighting function to control the relative importance of events near time t, with those at earlier times.

Choosing the time weighting function of the form $W(t-t') = T^{-1}e^{-(t-t')/T}$ yields two transport equations for the Lagrangian average of the tensor products $L_{ij}M_{ij}$ and $M_{ij}M_{ij}$ as $\mathcal{I}_{LM}$ and $\mathcal{I}_{MM}$ respectively:

$$\begin{aligned} \frac{D\mathcal{I}_{LM}}{Dt} &\equiv \frac{\partial \mathcal{I}_{LM}}{\partial t} + \overline{u}_i \frac{\partial \mathcal{I}_{LM}}{\partial x_i} = \frac{1}{T}\big(L_{ij}M_{ij} - \mathcal{I}_{LM}\big) \quad \text{and} \\ \frac{D\mathcal{I}_{MM}}{Dt} &\equiv \frac{\partial \mathcal{I}_{MM}}{\partial t} + \overline{u}_i \frac{\partial \mathcal{I}_{MM}}{\partial x_i} = \frac{1}{T}\big(M_{ij}M_{ij} - \mathcal{I}_{MM}\big). \end{aligned} \tag{4.2}$$

whose solutions yield

$$(C_s\Delta)^2 = \frac{\mathcal{I}_{LM}}{\mathcal{I}_{MM}}. \tag{4.3}$$

Here T is a time scale which represents the 'memory' of the Lagrangian averaging. Meneveau et al. [11] proposed the following time scale:

$$T = \theta\Delta(\mathcal{I}_{LM}\mathcal{I}_{MM})^{(-1/8)}; \qquad \theta = 1.5. \tag{4.4}$$

This procedure for Lagrangian averaging has also been extended to the scale-similar model by Anderson and Meneveau [33] and Sarghini et al. [34] and the scale-dependent dynamic model by Stoll and Porté-Agel [35].

Note that the time scale for Lagrangian averaging in eq. 4.4 contains an adjustable parameter which is typically chosen to be $\theta = 1.5$. The need for a 'dynamic' Lagrangian time scale is motivated in sec. 4.2. Park and Mahesh [10] introduced a procedure

for computing a dynamic Lagrangian time scale. However the Park and Mahesh [10] formulation was in the context of a spectral structured solver, and considered their dynamic Lagrangian time scale model along with their proposed control-based Corrected DSM. They proposed a correction step to compute the eddy viscosity using Fréchet derivatives, leading to further reduction of the Germano-identity error. Computing Fréchet derivatives of the objective function (in this case, the GIE) can involve significant computational overhead in an unstructured solver. The present work considers the dynamic Lagrangian time scale model in the absence of control-based corrections. Also, Park and Mahesh [10] computed their time scale for isotropic turbulence and turbulent channel flow by averaging along directions of homogeneity. The present work considers the time scale model in the absence of any spatial averaging.

The extension of the Lagrangian averaged DSM with a dynamic time scale to an unstructured grid framework requires modifications to the model proposed by Park and Mahesh [10] and is described in sec. 4.2.1. The Lagrangian DSM with this dynamic time scale T_{SC} is applied to three problems - turbulent channel flow (sec. 4.3.1), flow past a cylinder (sec. 4.3.2), and flow past a marine propeller in an off-design condition (sec. 4.3.3), on unstructured grids at different Reynolds numbers. It is shown that the procedure works well on unstructured grids and shows improvement over existing averaged DSM methods. Sec. 4.3.1 discusses the variation of T_{SC} with grid resolution, Reynolds numbers, and the practical advantages of this procedure in ensuring positive eddy viscosities and negligible computational overhead. Differences in the performance of the dynamic time scale and the original time scale due to Meneveau et al. [11] for the cylinder flow are analyzed in sec. 4.3.2. In 4.3.3, the model is applied to a challenging complex flow and it is shown that T_{SC} is a physically consistent time scale whose use yields good results.

4.2 Dynamic Lagrangian time scale

The time scale for Lagrangian averaging proposed by Meneveau et al. [11] (henceforth, T_{LDSM}) contains an adjustable parameter which is typically chosen to be $\theta = 1.5$. This value was chosen based on the autocorrelation of $L_{ij}M_{ij}$ and $M_{ij}M_{ij}$ from DNS of forced isotropic turbulence. This arbitrariness is acknowledged to be undesirable by

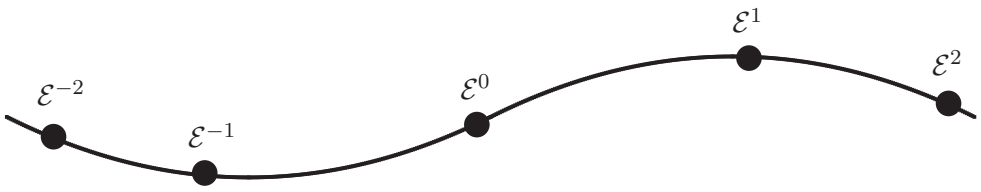

Figure 4.1: $\epsilon_{ij}\epsilon_{ij}$ at five events along a pathline.

the authors and in fact they document results of turbulent channel flow at $Re_\tau = 650$ to be marginally sensitive to the value of θ, with $\theta = 1.5$ appearing to yield the best results. You et al. [36] tested three different values of the relaxation factor θ and concluded T_{LDSM} was 'reasonably robust' to the choice of θ for a $Re_\tau = 180$ channel flow. Over the years, choosing a value for θ has demanded significant consideration by many practitioners who have found the results to be sensitive to θ, especially in complex flows [37].

The extension of the Lagrangian averaging procedure to other models has also presented the same dilemma. In simulations of turbulent channel flow at $Re_\tau = 1050$ using a two-coefficient Lagrangian mixed model [33], Sarghini et al. [34] note that a different parameter in T_{LDSM} might be required for averaging the scale similar terms. Vasilyev et al. [38] proposed extensions to the Lagrangian dynamic model for a wavelet based approach and used $\theta = 0.75$ for incompressible isotropic turbulence.

Park and Mahesh [10] note that T_{LDSM} has a high dependence on the strain rate through the L_{ij} and M_{ij} terms. They however show that the time scale of the GIE near the wall and the channel centerline are similar. Thereby they argue that strain rate may not be the most appropriate quantity for defining a time scale for Lagrangian averaging of the GIE. It seems only natural that the averaging time scale should be the time scale of the quantity being averaged which in this case is the GIE. Park and Mahesh [10] therefore, proposed a dynamic time scale T_{SC}, called "surrogate-correlation based time scale" T_{SC}.

4.2.1 Surrogate-correlation based time scale

Assuming knowledge of the local and instantaneous values of the GIE squared ($\mathcal{E} = \epsilon_{ij}\epsilon_{ij}$) at five consecutive events along a pathline as shown in fig. 4.1, where

$$\mathcal{E}^0 = \mathcal{E}(\mathbf{x}, t), \qquad \mathcal{E}^{\pm 1} = \mathcal{E}(\mathbf{x} \pm \mathbf{u}\Delta t, t \pm \Delta t), \qquad \mathcal{E}^{\pm 2} = \mathcal{E}(\mathbf{x} \pm 2\mathbf{u}\Delta t, t \pm 2\Delta t). \quad (4.5)$$

At each location, the following surrogate Lagrangian correlations for three separation times $(0, \Delta t, 2\Delta t)$ can be defined :

$$\begin{aligned} \mathcal{C}(l\Delta t) &= \frac{1}{5-l} \sum_{k=-2}^{2-l} (\mathcal{E}^k - \overline{\mathcal{E}})(\mathcal{E}^{k+l} - \overline{\mathcal{E}}); \qquad (l = 0, 1, 2) \\ \text{where} \quad \overline{\mathcal{E}} &= \frac{1}{5} \sum_{k=-2}^{2} \mathcal{E}^k \quad \text{is the average value.} \end{aligned} \tag{4.6}$$

To increase the number of samples, Park and Mahesh [10] averaged $\mathcal{C}(l\Delta t)$ and $\overline{\mathcal{E}}$ along directions of homogeneity. This is not practical for extension to inhomogeneous flows on unstructured grids. No further averaging of $\overline{\mathcal{E}}$ is a straightforward option; however, this approach results in a negative value for $\mathcal{C}(2\Delta t)$ and constant value for T_{SC} (not shown), which is unacceptable. To alleviate this, a running time average of the above terms upto the current time t_n is computed:

$$\begin{aligned} \mathcal{C}(l\Delta t) &= \sum_{t=0}^{t_n} \left(\frac{1}{5-l} \sum_{k=-2}^{2-l} (\mathcal{E}^{k,t} - \overline{\mathcal{E}}^t)(\mathcal{E}^{k+l,t} - \overline{\mathcal{E}}^t) \right); \qquad (l = 0, 1, 2) \\ \text{where} \quad \overline{\mathcal{E}}^t &= \sum_{\tau=0}^{t_n} \left(\frac{1}{5} \sum_{k=-2}^{2} \mathcal{E}^{k,\tau} \right) \quad \text{is the average value.} \end{aligned} \tag{4.7}$$

This leads to converged correlations after sufficiently long times and is a consistent and general method to compute the surrogate Lagrangian correlations. These correlations are then normalized by the zero-separation correlation $\mathcal{C}(0)$ to obtain

$$\rho(0) = 1, \qquad \rho(\Delta t) = \frac{\mathcal{C}(\Delta t)}{\mathcal{C}(0)}, \qquad \rho(2\Delta t) = \frac{\mathcal{C}(2\Delta t)}{\mathcal{C}(0)}. \tag{4.8}$$

An osculating parabola can be constructed passing through these three points and it can be described by

$$\rho(\delta t) = a(\delta t)^2 + b(\delta t) + 1, \tag{4.9}$$

where a, b can be written in terms of $\rho(0) = 1, \rho(\Delta t), \rho(2\Delta t)$ and Δt. Note that $\rho(\delta t)$ is an approximate correlation function (of separation time δt) for the true Lagrangian correlation. Thus the time scale based on the surrogate correlation T_{SC} is defined as the time when $\rho(\delta t) = 0$ *i.e.* the positive solution

$$T_{SC} = \frac{-b - \sqrt{b^2 - 4a}}{2a}. \tag{4.10}$$

If the surrogate Lagrangian correlations $\mathcal{C}$ have enough samples, $1 > \rho(\Delta t) > \rho(2\Delta t)$ is satisfied which leads to $a < 0$. As a result T_{SC} is always positive. In the initial stages of a simulation, there are not enough time samples. $1 > \rho(\Delta t) > \rho(2\Delta t)$ may not be satisfied and a could be positive. In such cases, T_{SC} is obtained by constructing the osculating parabola to be of the form $1 + a(\delta t)^2$ and passing through either of the two points $\rho(\Delta t), \rho(2\Delta t)$:

$$T_{SC} = min(\frac{dt}{\sqrt{1 - \rho(\Delta t)}}, \frac{2dt}{\sqrt{1 - \rho(2\Delta t)}}). \tag{4.11}$$

The minimum of the time scales is chosen so that the solution has lesser dependence on past values and can evolve faster from the initial transient stage. Note that the true Lagrangian correlation can be modeled by an exponential function $f(\delta t) = e^{(-\delta t/T)^2}$. Assuming $\Delta t \ll T$ and that $f(\delta t)$ passes through $\rho(0) = 1, \rho(\Delta t), \rho(2\Delta t)$, then $T_{SC} = \delta t = T$ is also the time when the modeled exponential correlation becomes e^{-1}.

4.2.2 Lagrangian approximation

The proposed dynamic time scale requires the values of the Germano-identity error (GIE) squared $\mathcal{E}$ at five events along a pathline. Rovelstad et al. [39] and Choi et al. [32] suggest the use of Hermite interpolation for computing turbulent Lagrangian statistics. However, Hermite interpolation requires third order derivatives in every direction of the tracked quantity, rendering it prohibitively expensive. Meneveau et al. [11] use multilinear interpolation to obtain the values of $\mathcal{I}_{LM}$ and $\mathcal{I}_{MM}$ at a Lagrangian location.

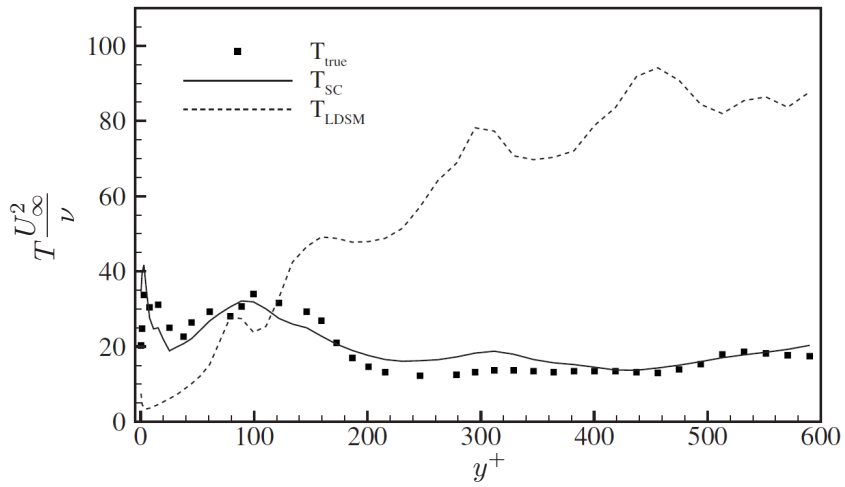

Figure 4.2: Lagrangian time scales of the GIE for turbulent channel flow at $Re_\tau = 590$. Reproduced with permission from Park and Mahesh [10].

Even multilinear interpolation gets expensive in an unstructured grid setting. The use of an expensive interpolation method just to compute the time scale for Lagrangian averaging may be unnecessary. As a result, a simple material derivative relation as proposed by Park and Mahesh [10] is used to approximate Lagrangian quantities in an Eulerian framework :

$$\frac{D\mathcal{E}}{Dt} = \frac{\partial \mathcal{E}}{\partial t} + \overline{u}_i \frac{\partial \mathcal{E}}{\partial x_i}. \tag{4.12}$$

A simple first order in time and central second order in space, finite-volume approximation for the convective term is used to approximate values of $\mathcal{E}$ in eqn. 4.5 in terms of the local $\mathcal{E}(\mathbf{x}, t) = \mathcal{E}^{0,n}$ and $\mathcal{E}(\mathbf{x}, t - \Delta t) = \mathcal{E}^{0,n-1}$. The Green-Gauss theorem is used to express the convective term in conservative form and evaluate it as a sum over the faces of a computational volume.

Park and Mahesh [10] show that the dynamic time scale T_{SC} agrees well with the true Lagrangian correlation time scale, whereas T_{LDSM} exhibits opposite behavior near the wall (fig. 4.2). They also show that the Lagrangian correlations at different wall normal locations collapse when normalized with T_{SC} while such collapse is not observed with T_{LDSM}.

LES							
Case	Re_τ	$N_x \times N_y \times N_z$	$L_x \times L_z$	Δx^+	Δz^+	Δy^+_{min}	$\Delta y_{cen}/\delta$
590f		$160 \times 150 \times 200$		23.2	9.3	1.8	0.03
590tl	590	$160 \times 84 \times (200, 100)$		23.2	9.3,18.5	1.8	0.04
590c		$64 \times 64 \times 64$	$2\pi \times \pi$	58	29	1.6	0.08
1ktl	1000	$160 \times 84 \times (200, 100)$		39.3	15.8,31.4	3.1	0.04
2ktl	2000	$320 \times 120 \times (400, 200, 100)$		39.3	15.7,31.4,62.8	2.0	0.04
DNS							
Moser et al. [40]	587	$384 \times 257 \times 384$	$2\pi \times \pi$	9.7	4.8	-	0.012
del Alamo et al. [41]	934	$- \times 385 \times -$	$8\pi \times 3\pi$	11	5.7	-	-
Hoyas and Jimenez [42]	2003	$- \times 633 \times -$	$8\pi \times 3\pi$	12	6.1	-	-

Table 4.1: Grid parameters for turbulent channel flow.

4.3 Results

The unstructured finite-volume method (sec. 2.4) is used to solve eq. 2.5. The Lagrangian DSM (eq. 4.3) with dynamic time scale T_{SC} (eq. 4.10) is applied to three problems - turbulent channel flow (sec. 4.3.1), flow past a cylinder (sec. 4.3.2), and flow past a marine propeller in crashback (sec. 4.3.3).

4.3.1 Turbulent channel flow

Results are shown for a turbulent channel flow at three Reynolds numbers; $Re_\tau = 590, 1000, 2000$ and different grid resolutions. Here $Re_\tau = u_\tau \delta/\nu$ where u_τ, δ and ν denote the friction velocity, channel half-width and viscosity respectively. Table 4.1 lists the Re_τ and grid distribution for the various simulations. All LES have uniform spacing in x. The cases with 'tl' indicate that a $4:2$ transition layer has been used in z along y as shown in fig. 4.3. As shown, a transition layer allows transition between two fixed edge ratio computational elements. It allows a finer wall spacing to coarsen to a fixed ratio coarser outer region spacing. All other cases have a uniform spacing in z. The LES results are compared to the DNS of Moser et al. [40] for $Re_\tau = 590$, del Alamo et al. [41] for $Re_\tau = 1000$, and Hoyas and Jimenez [42] for $Re_\tau = 2000$ whose grid parameters are also included in the table for comparison. Note that the LES have employed noticeably coarse resolutions and hence contribution from the SGS model is expected to be significant.

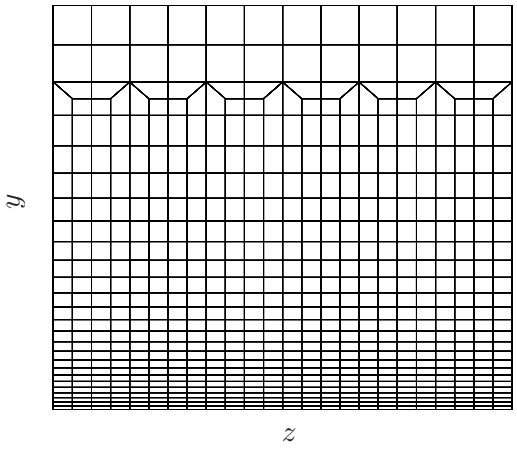

Figure 4.3: Transition layer.

Validation at $Re_\tau = 590$

Fig. 4.4(a) shows good agreement for the mean velocity which indicates that the wall stress is well predicted. The velocity fluctuations in fig. 4.4(b) are in reasonable agreement with unfiltered DNS as is to be expected at coarse resolutions. The Lagrangian DSM is active at this resolution and ν_t/ν peaks at 0.21 around $y^+ \sim 76$ (not shown). Fig. 4.4(c) compares the dynamic Lagrangian time scale T_{SC} to T_{LDSM} which is calculated a posteriori. Note that T_{SC} is much higher near the wall than T_{LDSM}. Since T_{SC} is calculated from $\rho(\delta t)$, this behavior is consistent with the high correlation of GIE near the wall observed from fig. 4.4(d). For such relatively coarse near-wall resolution, GIE is expected to be high near the wall and in addition, remain correlated longer because of the near-wall streaks. Figs. 4.5(a)-(b) show that GIE is high near the wall in the form of near-wall streaks. Such behavior is consistent with the physical nature of the flow; the DNS of Choi et al. [32] shows higher streamwise Lagrangian time scale near the wall due to streaks and streamwise vortices.

Next, an unstructured zonal grid is used, which has a transition layer in Z along Y (case 590tl). Figs. 4.6(a)-(b) show that the results are in good agreement, similar to case 590f. The statistics (fig. 4.6(b)) have a small kink around $y^+ \sim 140$ where the grid transitions. This kink in the statistics is an artifact of numerical discretization and grid skewness, and is present even when no SGS model is used. Overall, the results indicate

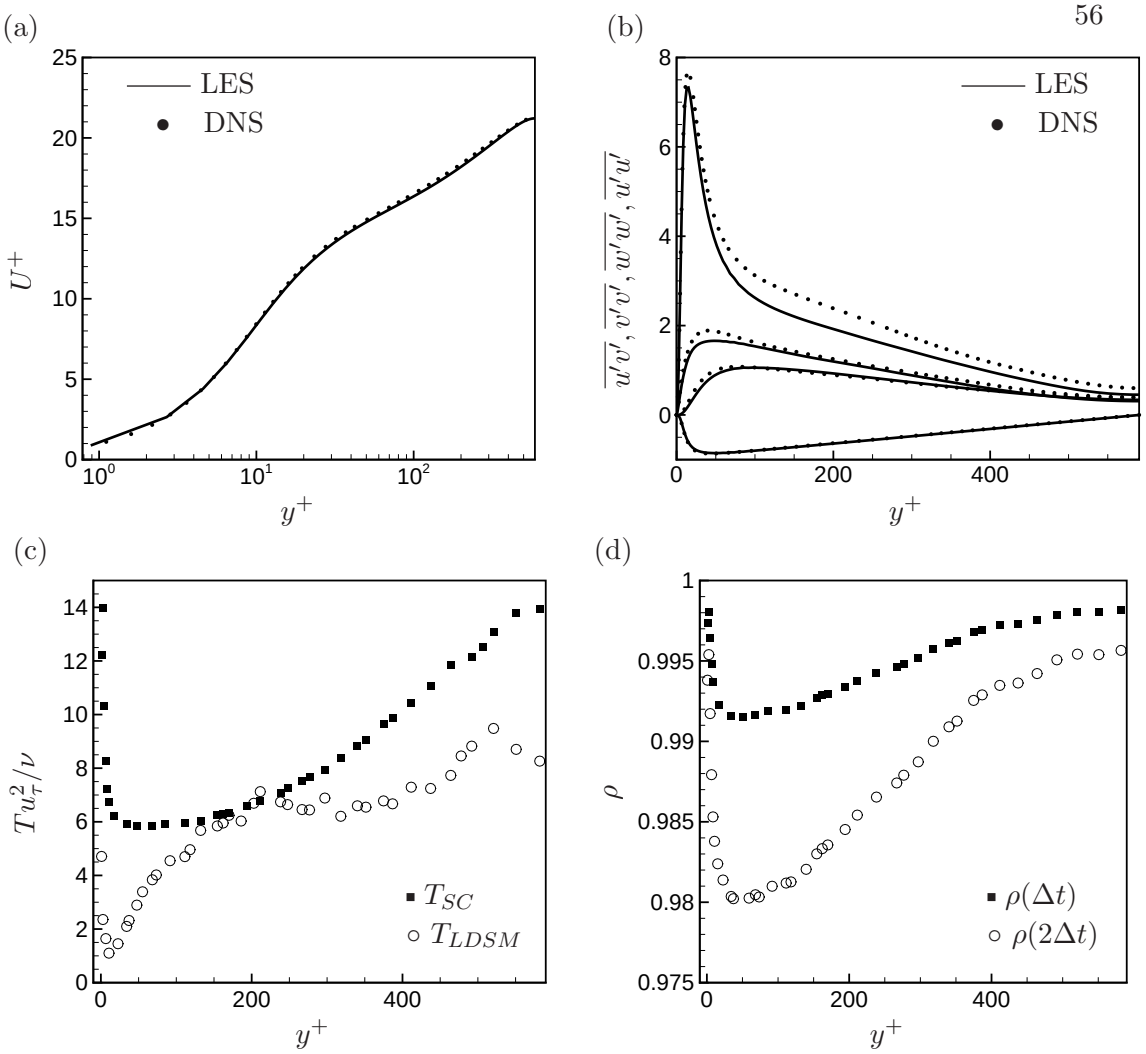

Figure 4.4: Turbulent channel flow - Case 590f: (a) mean velocity, (b) rms velocity fluctuations, (c) time scales, (d) normalized surrogate Lagrangian correlations.

that the Lagrangian DSM with T_{SC} works well on a grid where non-orthogonal elements are present and plane averaging is not straightforward.

Variation with grid resolution at $Re_\tau = 590$

Figs. 4.7(a)-(b) provide an interesting insight into the variation of T_{SC} and ν_t with grid resolution. The coarsest grid (590c) has the highest GIE (not shown) and consequently, highest T_{SC}. The SGS model compensates for the coarse grid by increasing ν_t. Cases

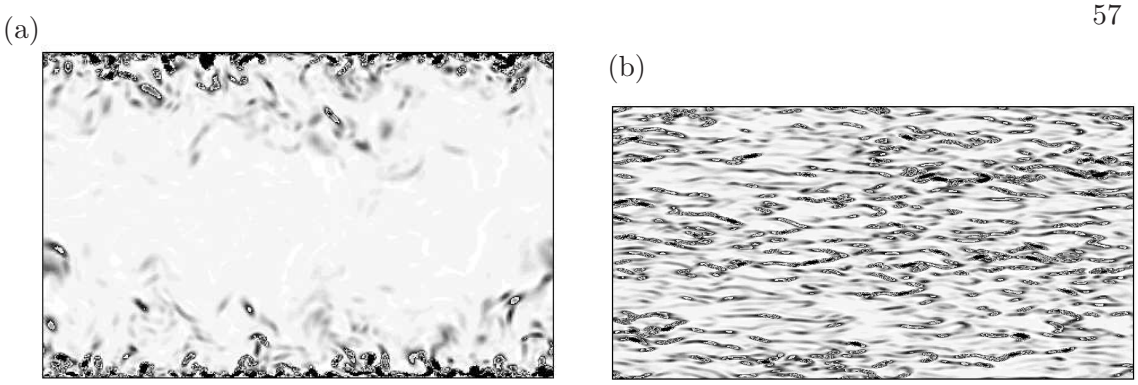

Figure 4.5: Turbulent channel flow - Case 590f: Instantaneous contours of Germano-identity error $g = (GIE/u_\tau^2)^2$, (a) yz plane, contours vary as $0 \leq g \leq 3$, (b) xz plane at $y^+ = 12$, contours vary as $0 \leq g \leq 40$.

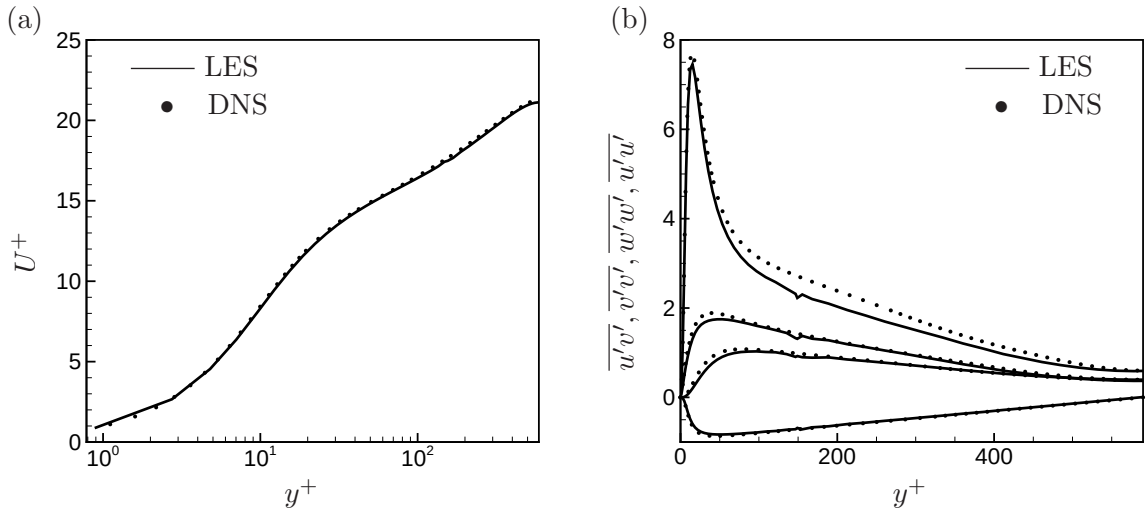

Figure 4.6: Turbulent channel flow - Case 590tl: (a) mean velocity, (b) rms velocity fluctuations.

590f and 590tl have almost the same near-wall grid resolution. As a result, T_{SC} and ν_t are similar for the two cases until $y^+ \sim 50$. The y-distribution then begins to change slightly but the biggest change is in Δz which doubles due to the transition layer in case 590tl. The GIE also increases in the coarse region which subsequently increases the GIE correlations, resulting in higher T_{SC}.

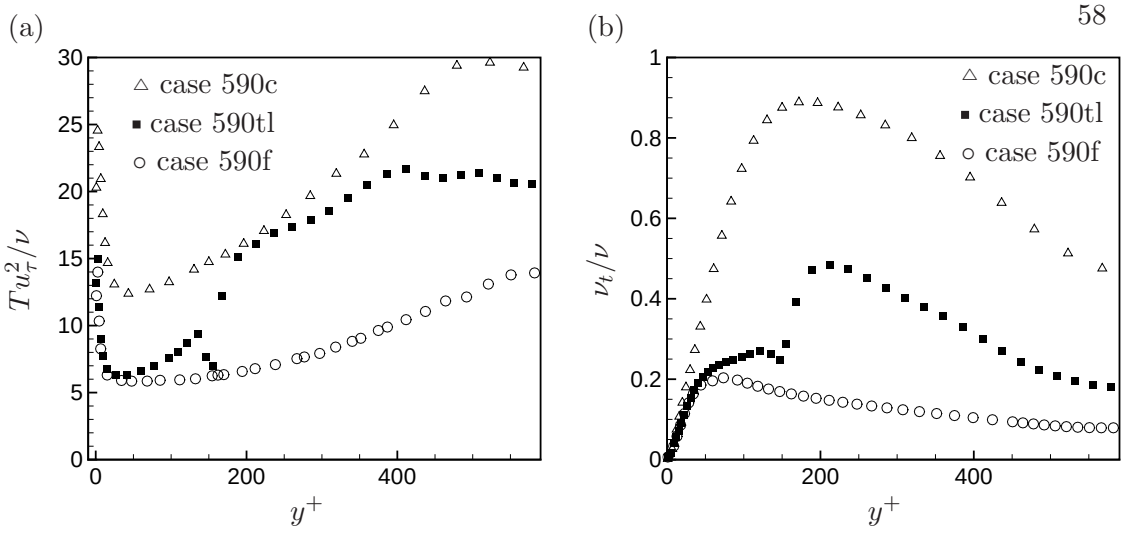

Figure 4.7: Turbulent channel flow : Comparison of (a) Lagrangian time scales T_{SC}, (b) eddy viscosity.

Variation of T_{SC} with Reynolds numbers

The Lagrangian DSM with dynamic time scale T_{SC} (eq. 4.10) is applied to turbulent channel flow at higher Reynolds numbers of $Re_\tau = 1000$ and $Re_\tau = 2000$. The grid used for case 1ktl is the same as used for case 590tl and hence the resolution in wall units is almost twice as coarse, as shown in table 4.1. Fig. 4.8(a) shows good agreement for the mean velocity which indicates that the wall stress is well predicted. The velocity fluctuations in fig. 4.8(b) are in reasonable agreement with unfiltered DNS. The grid used for case 2ktl is based on similar scaling principles as case 590tl, which is to enable a wall-resolved LES. Hence, it has 2 transition layers to coarsen from a fine near-wall Δz to a coarser outer region Δz as listed in table 4.1. Fig. 4.8 also shows good agreement for the mean velocity and rms velocity fluctuations with unfiltered DNS. These examples show that the Lagrangian DSM with T_{SC} also works well for high Reynolds numbers on unstructured grids.

Fig. 4.9 compares the computed Lagrangian time scales, plotted in inner and outer scaling, for the three cases - 590tl, 1ktl, and 2ktl which correspond to $Re = 590, 1000, 2000$ respectively. Note that the grid away from the wall is similar in all the cases. As Reynolds number increases, the normalized surrogate correlations of the GIE increase, which results in increasing T_{SC}^+ (fig. 4.9(a)). This trend of increasing

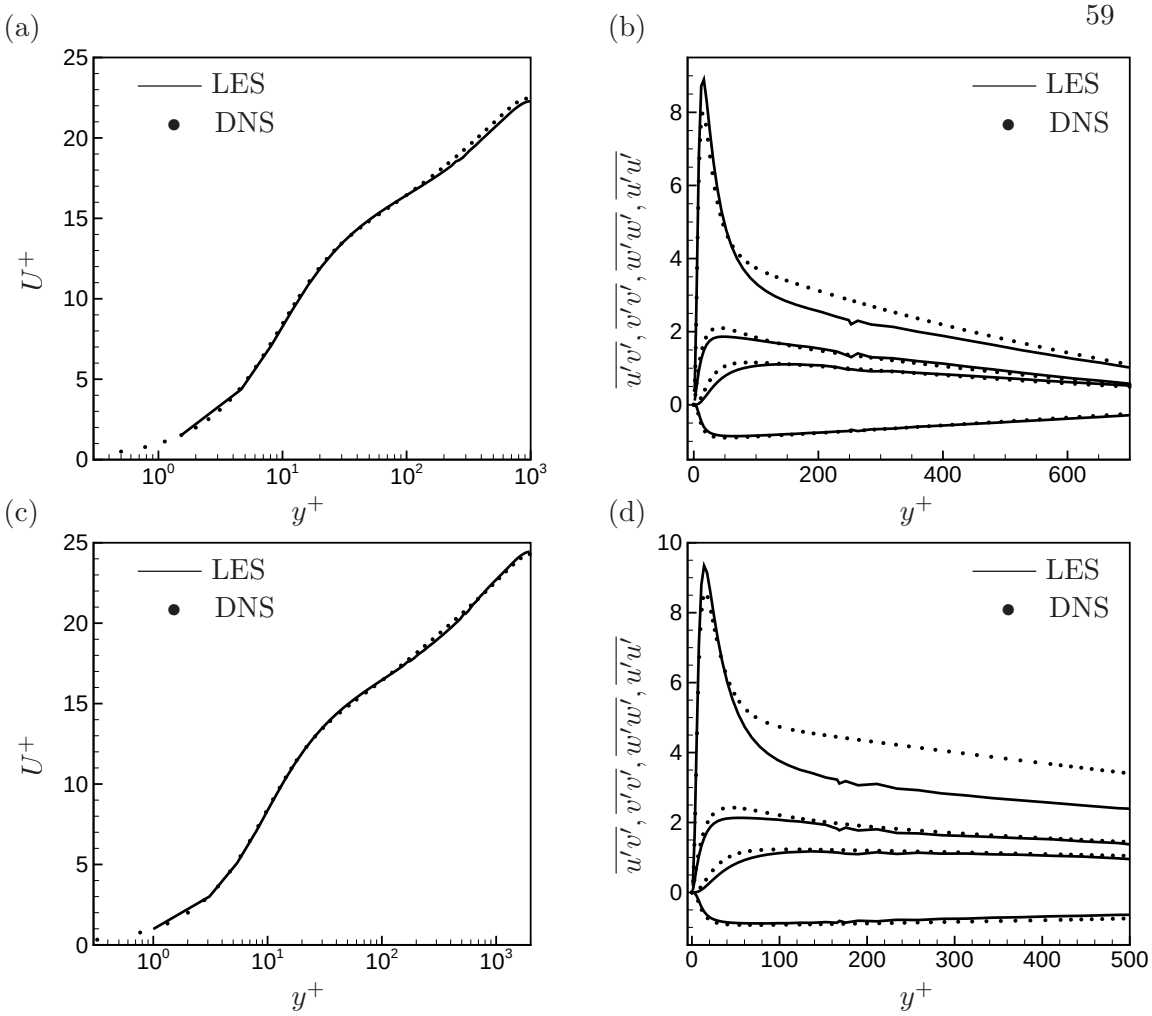

Figure 4.8: Turbulent channel flow - Case 1ktl: (a) mean velocity, (b) rms velocity fluctuations; Case 2ktl: (c) mean velocity, (d) rms velocity fluctuations.

Lagrangian time scale is also consistent with the observations of Choi et al. [32] who noticed an increase in the time scale of Lagrangian streamwise velocity correlations with Reynolds number in their DNS of turbulent channel flow. The jumps correspond to the locations where the grid transitions ($y/\delta \sim 0.3$).

Comparison between different averaging methods

For a given problem, as the grid becomes finer, the results obtained using different averaging schemes for DSM tend to become indistinguishable from one another [43].

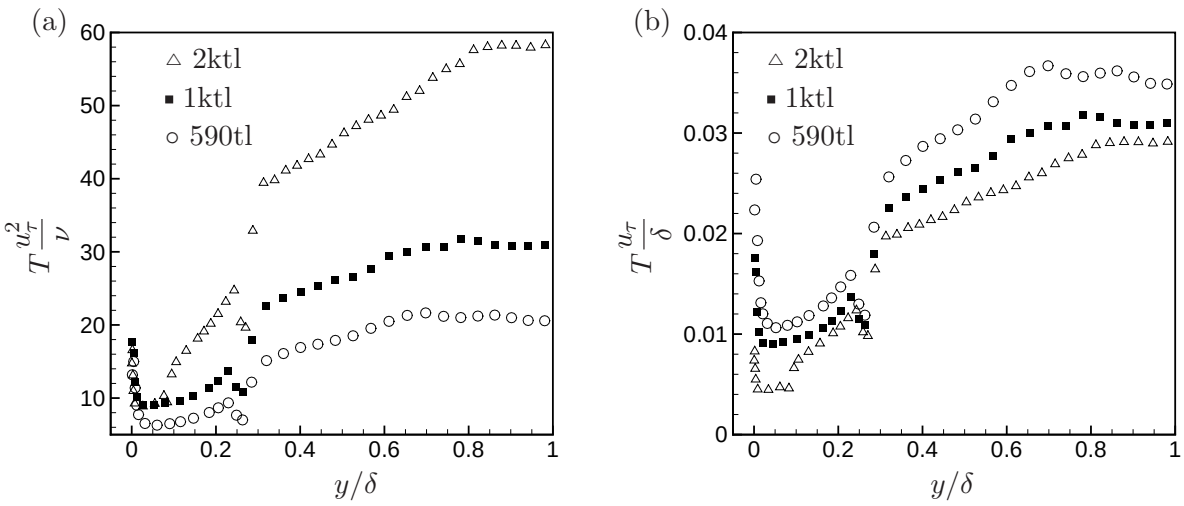

Figure 4.9: Turbulent channel flow : Comparison of Lagrangian time scales T_{SC}. (a) scaled in viscous units T^+_{SC}, (b) scaled in outer units T_{SC}.

On a finer grid such as case 590f, the effect of averaging and Lagrangian averaging time scale is small. Hence, in what follows, results are shown for case 590c which is a very coarse grid but which shows difference between the different averaging schemes. For all the averaging runs considered, statistics are collected over $96\delta/u_\tau$. Fig. 4.10(a) shows that the mean velocity shows increasingly improving agreement with DNS as the averaging scheme changes from averaging along homogeneous directions (plane) to Lagrangian averaging using T_{LDSM} and finally T_{SC}. Fig. 4.10(b) shows that the rms velocity fluctuations are in a slightly better agreement with unfiltered DNS using T_{SC} over T_{LDSM}. $\overline{u'u'}$ is not plotted here as it is not much different for the two time scales. The fact that Lagrangian averaging performs better than plane averaging has been demonstrated by Meneveau et al. [11] and Stoll and Porté-Agel [43]. The present results show that using T_{SC} as the time scale for Lagrangian averaging can predict even better results.

Figs. 4.10(c)-(f) compare the differences between the time scales T_{SC} and T_{LDSM} in more detail. In general, increasing the extent of averaging by either increasing averaging volume (plane averaging) or increasing the averaging time scale (Lagrangian) will decrease the variance of the model coefficient. T_{LDSM} with $\theta = 3.0$ implies a larger averaging time scale than $\theta = 1.5$ and hence the eddy viscosity with $\theta = 3.0$ has a

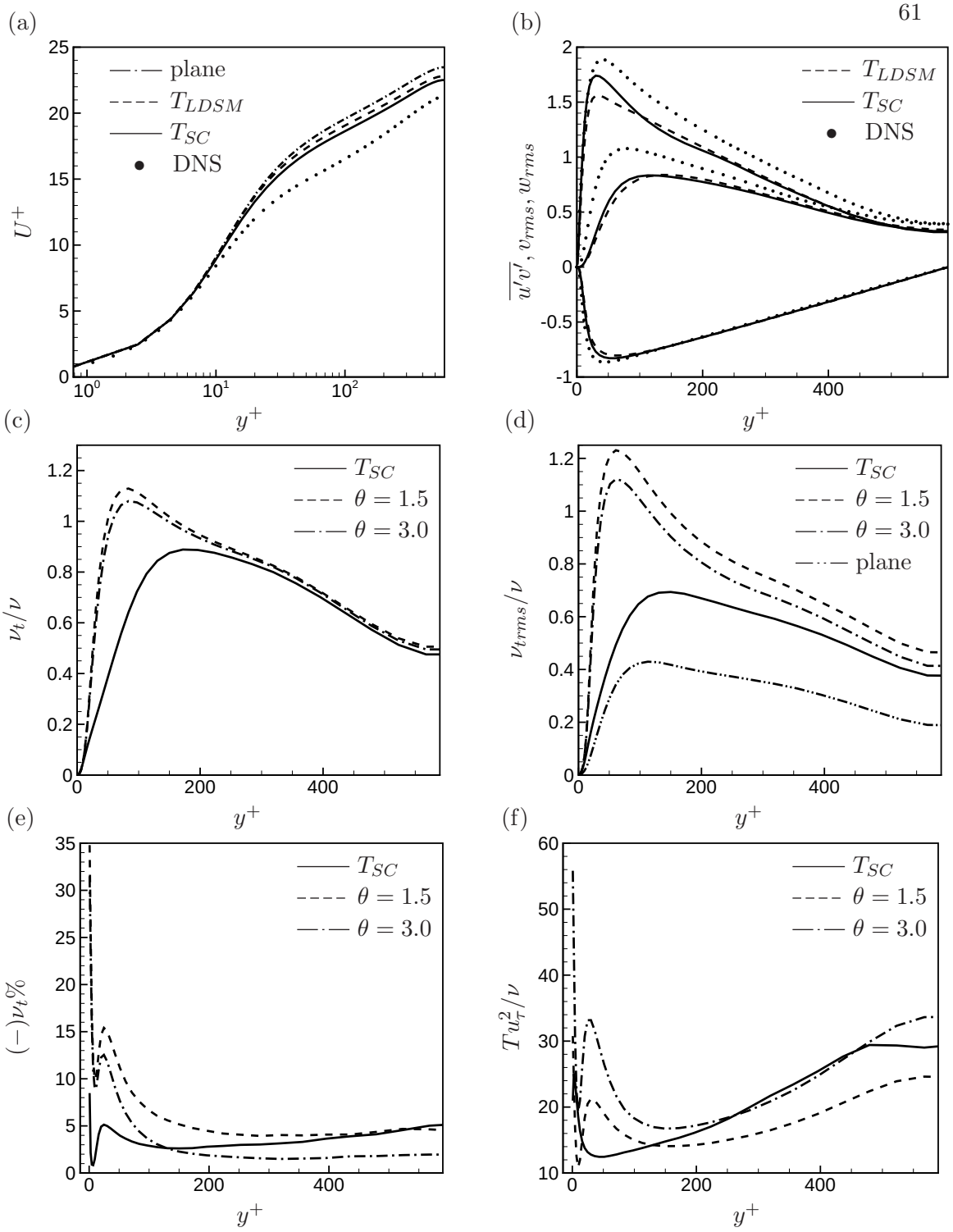

Figure 4.10: Comparison of time scales from case 590c: (a) mean velocity, (b) rms velocity fluctuations, (c) mean eddy viscosity, (d) rms of eddy viscosity, (e) percentage of negative ν_t values, (f) time scales.

slightly lower mean and variance (fig. 4.10(c)-(d)) when compared to $\theta = 1.5$. The Lagrangian model with T_{SC} has a lower mean compared to T_{LDSM} and this is consistent with lower dissipation leading to higher resolved turbulence intensities shown earlier in fig. 4.10(b). Fig. 4.10(d) shows that T_{SC} produces an eddy viscosity field that has much less variation than T_{LDSM} but more than plane averaging.

Stoll and Porté-Agel [43] report that the Lagrangian averaged model using T_{LDSM} has approximately 8% negative values for ν_t compared to 40% for the locally smoothed (neighbor-averaged) model in their simulations of a stable atmospheric boundary layer. The percentage of time that negative ν_t values are computed is shown in fig. 4.10(e). Plane averaged ν_t never became negative and hence is not plotted. Clearly, ν_t averaged using T_{SC} has the least amount of negative values up until $y^+ \sim 100$ (which contains 50% of the points). Even after $y^+ \sim 100$, percentage of negative ν_t values computed by T_{SC} is less than T_{LDSM} with $\theta = 1.5$. It is also observed that increasing θ reduced the number of negative values, as expected intuitively. Therefore, T_{SC} is able to achieve the smoothing effect of plane averaging while retaining spatial localization.

When the time scales are compared (4.10(f)), it is found that T_{SC} actually overlaps with $T_{LDSM}, \theta = 3.0$ for almost half the channel width. For this particular computation, $\theta = 3.0$ is therefore preferable to $\theta = 1.5$. This makes it entirely reasonable to suppose that other flows might prefer some other θ than just 1.5. The dynamic procedure proposed in this paper alleviates this problem.

Finally, computing a dynamic T_{SC} for Lagrangian averaging the DSM terms does not incur a significant computational overhead. For case 590c, the total computational time required for computing T_{SC} and then using it for Lagrangian averaging of the DSM terms is just 2% more than that when no averaging of the DSM terms is performed.

4.3.2 Flow past a cylinder

The Lagrangian DSM with dynamic time scale T_{SC} (eq. 4.10) is applied to flow past a circular cylinder. Cylinder flow is chosen as an example of separated and free-shear flow. Also, cylinder flow varies significantly with Reynolds number, and is therefore a challenging candidate for validation. LES is performed at two Reynolds numbers (based on freestream velocity U_∞ and cylinder diameter D); $Re_D = 300$ and $Re_D = 3900$. The flow is transitional at $Re_D = 300$ and turbulent at $Re_D = 3900$. LES results

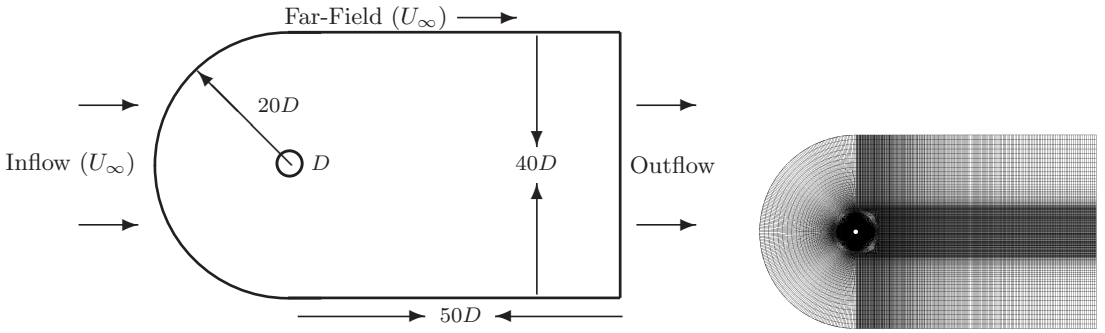

Figure 4.11: Computational domain with boundary conditions and grid for a cylinder.

are validated with available experimental data and results from past computations on structured and zonal grids at both these Reynolds numbers. An additional simulation is performed at $Re_D = 3900$ using Meneveau et al.'s [11] time scale T_{LDSM}. Results using T_{SC} are found to be in better agreement than using T_{LDSM}; the differences between the two time scales are discussed later.

Grid and boundary conditions

The computational domain and boundary conditions used for the simulations are shown in fig. 4.11. The domain height is $40D$, the spanwise width is πD and the streamwise extent is $50D$ downstream and $20D$ upstream of the center of the cylinder. An unstructured grid of quadrilaterals is first generated in a plane, such that computational volumes are clustered in the boundary layer and the wake. This two-dimensional grid is then extruded in the spanwise direction to generate the three-dimensional grid; 80 spanwise planes are used for both the simulations and periodic boundary conditions are imposed in those directions. Uniform flow is specified at the inflow, and convective boundary conditions are enforced at the outflow.

Validation at $Re_D = 300$

The $Re_D = 300$ computations are performed on a grid where the smallest computational volume on any spanwise station of the cylinder is of the size $2.0e^{-3}D \times 5.2e^{-3}D$ and stretches to $8.3e^{-2}D \times 8.3e^{-2}D$ at a downstream location of $5D$. Comparing this to the DNS of Mahesh et al. [3], their control volumes adjacent to the cylinder were of size

	$\langle C_D \rangle$	$\sigma(C_D)$	$\sigma(C_L)$	St	$-C_{P_b}$
Current	1.289	0.0304	0.39	0.203	1.02
Kravchenko et al. [44]	1.28	-	0.40	0.203	1.01
Mittal and Balachandar [45]	1.26	-	0.38	0.203	0.99
Babu and Mahesh [46]	1.26	0.0317	0.41	0.206	-
Williamson [47]	1.22	-	-	0.203	0.96

Table 4.2: Flow parameters at $Re_D = 300$. Legend for symbols : mean drag coefficient $\langle C_D \rangle$, rms of drag and lift coefficient ($\sigma(C_D), \sigma(C_L)$), Strouhal number St and base pressure C_{P_b}.

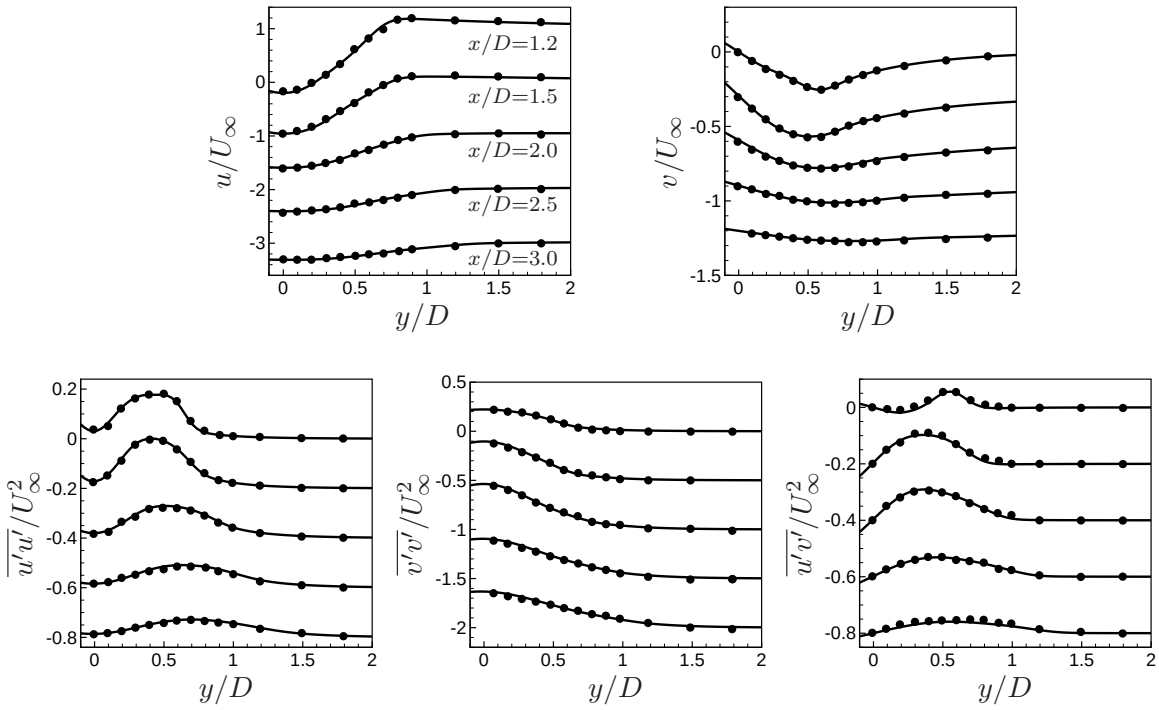

Figure 4.12: Vertical profiles at streamwise stations downstream of the cylinder at $Re_D = 300$. —— : current solution; • : spectral solution of Mittal and Balachandar [45].

$2.2e^{-3}D \times 1.0e^{-2}D$. As expected at this resolution, DSM is found to be dormant in the near-field. The wake of the cylinder is also well-resolved such that $\nu_t/\nu \sim 0.06$ even around $x/D = 30$. It can be safely assumed that SGS contribution from DSM is not significant in this case.

	$\langle C_D \rangle$	$\sigma(C_L)$	St	$-C_{P_b}$	θ°_{sep}	L_{rec}/D
T_{SC}	1.01	0.139	0.210	1.00	88.0	1.40
T_{LDSM}	0.99	0.135	0.208	1.00	87.0	1.63
Kravchenko and Moin [48]	1.04	-	0.210	0.94	88.0	1.35
Lourenco and Shih (taken from [3])	0.99	-	0.215	-	86.0	1.40

Table 4.3: Flow parameters at $Re_D = 3900$. Legend for symbols : mean drag coefficient $\langle C_D \rangle$, rms of drag and lift coefficient $(\sigma(C_D), \sigma(C_L))$, Strouhal number St and base pressure C_{P_b}, separation angle θ°_{sep}, recirculation length L_{rec}/D.

Integral quantities show good agreement with previous computations and experiment as shown in table 4.2. For comparison, the previous computations are the B-spline zonal grid method of Kravchenko et al. [44], spectral solution of Mittal and Balachandar [45], unstructured solution of Babu and Mahesh [46] and experimental results of Williamson [47]. Converged statistics are obtained over a total time of $360D/U_\infty$. Mean flow and turbulence statistics show excellent agreement with the spectral computations of Mittal and Balachandar [45] as shown in fig. 4.12.

Validation at $Re_D = 3900$

The same computational domain as fig. 4.11 and a similar grid topology is used to simulate turbulent flow past a cylinder at $Re_D = 3900$. The wake is slightly more refined than the $Re_D = 300$ grid. The smallest computational volume on any spanwise station of the cylinder is still of the size $2.0e^{-3}D \times 5.2e^{-3}D$ but stretches to $3.9e^{-2}D \times 2.9e^{-2}D$ at a downstream location of $5D$. To compare the performance of different Lagrangian averaging based methods, LES is performed using both the proposed dynamic time scale T_{SC} and Meneveau et al.'s [11] time scale T_{LDSM}. Integral quantities using T_{SC} show good agreement with the B-spline computation of Kravchenko and Moin [48] and the experiments of Lourenco and Shih (taken from [3]) as shown in table 4.3. Note that T_{LDSM} also shows similar agreement for the wall quantities; however, L_{rec}/D which depends on the near-field flow, shows discrepancy. This points towards a difference in the values of the time scales away from the cylinder.

The time averaged statistics for flow over a cylinder have been computed by different authors using different time periods for averaging. Franke and Frank [49] studied this

issue in detail and noted that more than 40 shedding periods are required to obtain converged mean flow statistics in the neighborhood of the cylinder. In the current work, statistics are obtained over a total time of $404D/U_\infty$ ($\sim$ 85 shedding periods) and then averaged over the spanwise direction for more samples. To our knowledge, this is the most amount of time, the statistics have been averaged over for this flow. Converged mean flow and turbulence statistics using T_{SC} show good agreement with the B-spline computations of Kravchenko and Moin [48] and the experimental data of Ong and Wallace [50] upto $x/D = 10$ as shown in figs. 4.13 and 4.14. The experimental data of Ong and Wallace [50] is also plotted for v/U_∞ in fig. 4.13 as the data of Kravchenko and Moin [48] has a bit of scatter at $x/D = 6, 7, 10$. It is presumed that not enough averaging time is the primary reason for the slight difference in the results, particularly further downstream ($x/D > 6$). Results using T_{LDSM} are also shown for comparison. Difference in the statistics between the two time scales are seen to be significant in the near-wake upto $x/D \sim 4.0$, and decrease further downstream.

The power spectral density (PSD) of streamwise, cross-flow velocity and pressure at two downstream locations $(x/D, y/D, z/D) \equiv (5, 0, 0), (10, 0, 0)$ are plotted in fig. 4.15. Time history of u, v, p are obtained over an interval of $456D/U_\infty$ with $304,000$ evenly spaced samples and PSD is computed using Fast Fourier Transformation (FFT). The frequency is non-dimensionalized by the Strouhal shedding frequency ω_{st}. The power spectra for u and v show good agreement with the experimental data of Ong and Wallace [50]. Consistent with previous studies [48], the peaks in u are not very well defined and so the p spectra are shown. The present LES shows peaks at twice the shedding frequency for the u and p spectra and peaks at the shedding frequency for v spectra, as expected at centerline locations of the wake. An inertial subrange can be clearly observed for the u, v spectra for both the current LES and experiment. As noted by Kravchenko and Moin [48] the spectra are consistent with the presence of small scales that remain active far from the cylinder and hence also consistent with the instantaneous flow shown in fig. 4.16. They also noticed that the effect of excessive dissipation leads to a rapid decay of the spectra at the higher wave numbers and that spectra obtained by LES based on non-dissipative schemes better match the experiments. The agreement between current LES and experiment for a large spectral range, especially at high frequencies, confirms this trend while suggesting that the SGS model is not overly dissipative. The agreement

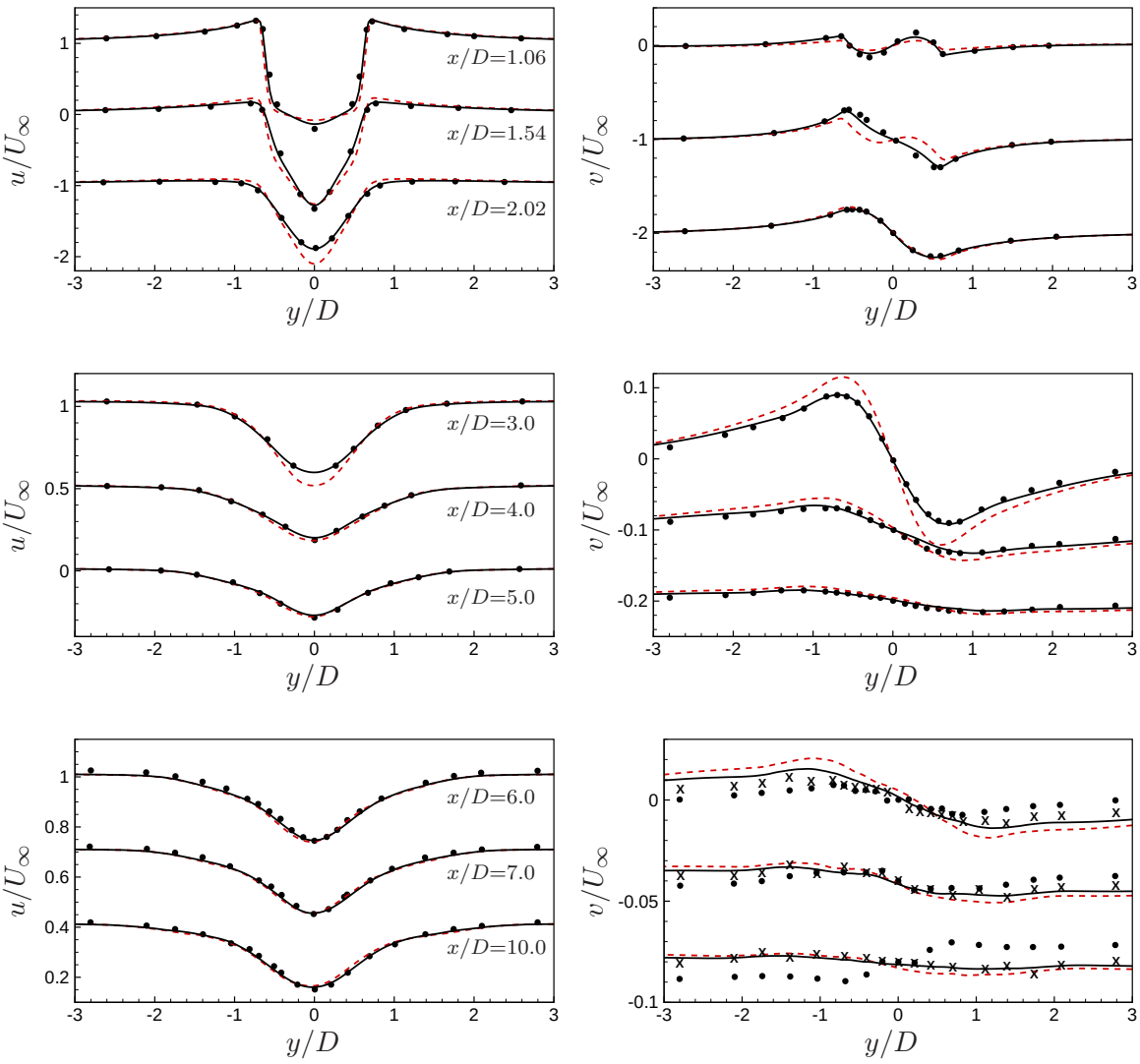

Figure 4.13: Vertical profiles at streamwise stations downstream of the cylinder at $Re_D = 3900$. —— : T_{SC}; - - - - : T_{LDSM}; • : B-spline solution of Kravchenko and Moin [48]; × : Experiment of Ong and Wallace [50].

with experimental spectra even at fairly small scales is encouraging. At $x/D = 5$ the highest frequency from the current LES which matches the experiment is almost three times that of Kravchenko and Moin [48] while at $x/D = 10$, it is almost the same. Note that decay in the PSD at $x/D = 10$ is faster than the upstream location, consistent with coarsening streamwise resolution downstream.

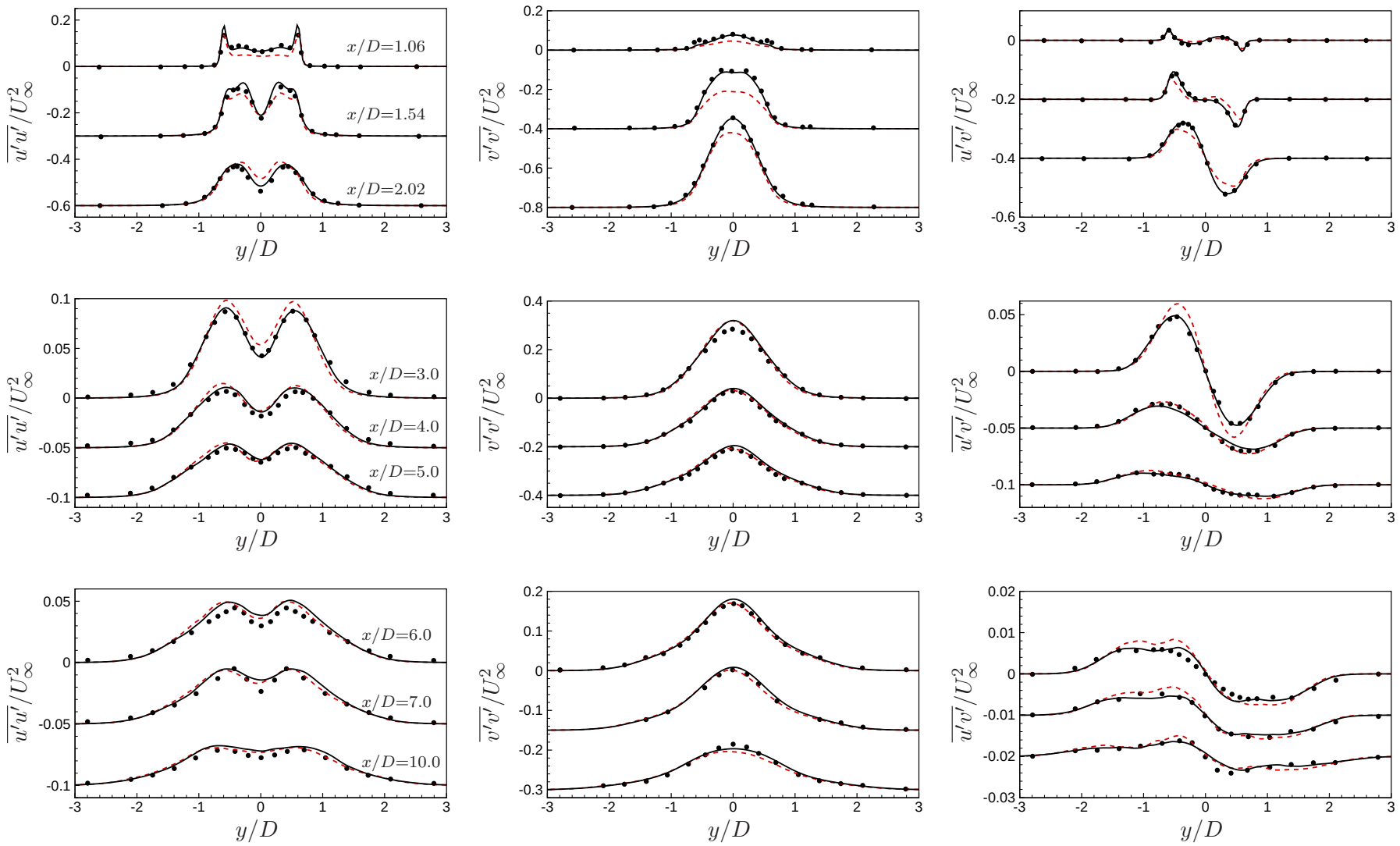

Figure 4.14: Vertical profiles at streamwise stations downstream of the cylinder at $Re_D = 3900$. —— : T_{SC}; ---- : T_{LDSM}; • : B-spline solution of Kravchenko and Moin [48].

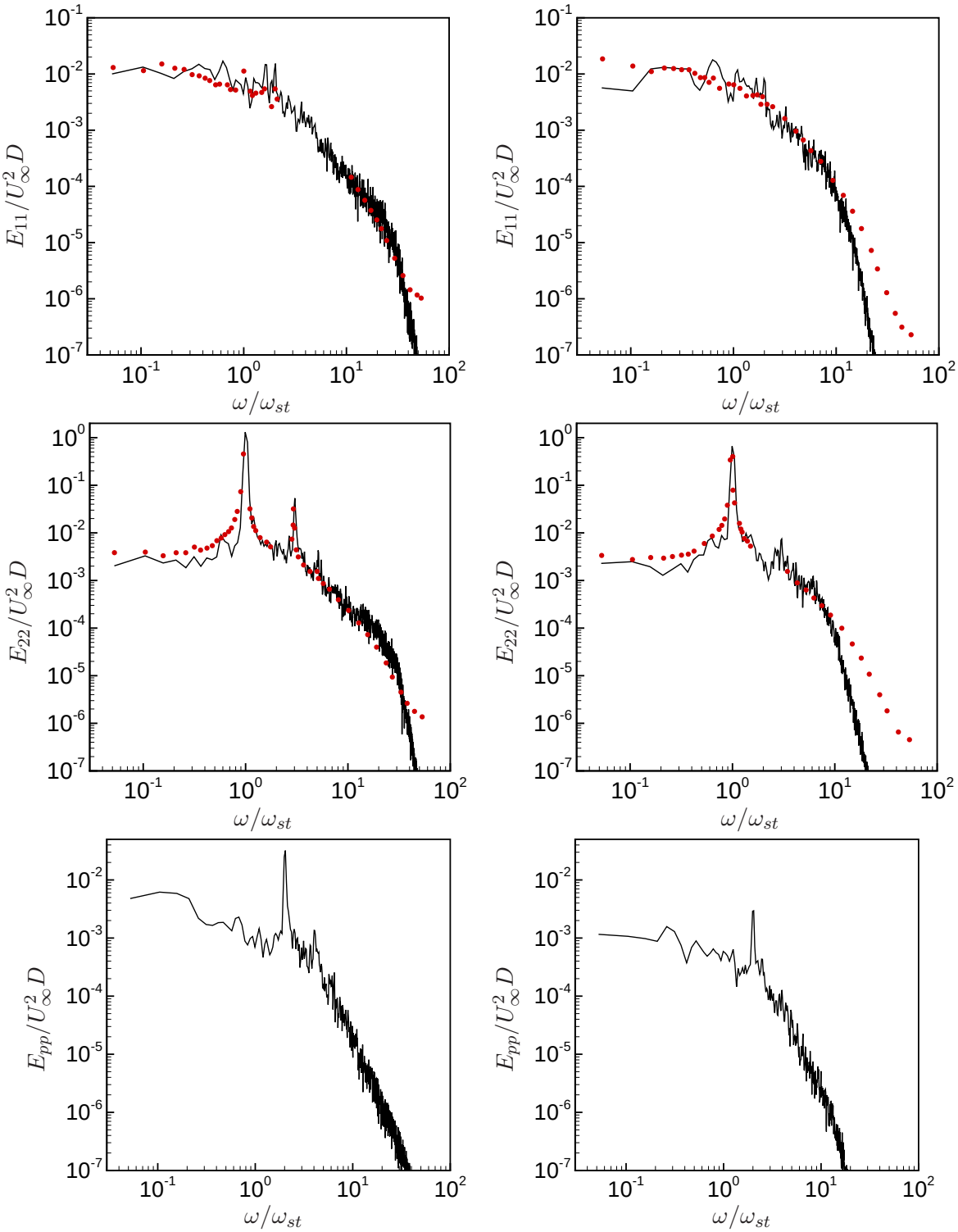

Figure 4.15: Power density spectra at $x/D = 5.0$ (left), $x/D = 10.0$ (right); —— current LES, • experiment of Ong and Wallace [50].

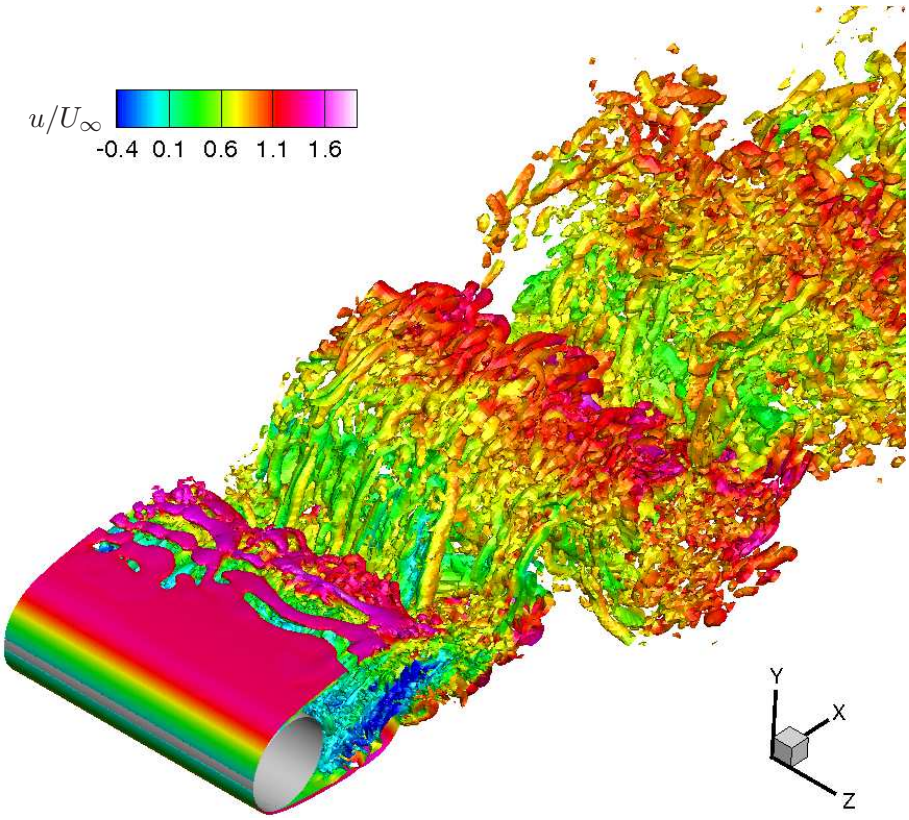

Figure 4.16: Cylinder flow - $Re_D = 3900$: Instantaneous iso-surfaces of Q-criterion [51] ($Q = 2$) colored by u-velocity.

Instantaneous flow and GIE

Three-dimensional flow structures of varying scale are observed in fig. 4.16. The separating shear layer transitions to turbulence, breaking up into smaller spanwise structures which then mix in the primary Karman vortex. An unsteady recirculation region with small scales is trapped between the shear layers. The figure also shows quasi-periodic longitudinal vortical structures as observed by previous studies [44, 52]) that are associated with vortex stretching in the vortex street wake [52]. Fig. 4.17 shows that the instantaneous GIE also follows the pattern of the Karman vortex street. The top shear layer can be seen to roll up (within one diameter) to form the primary vortex. The GIE is highest in the turbulent shear layers where scales are smaller. As the grid becomes coarser downstream, DSM plays a more dominant role, providing a higher value of ν_t

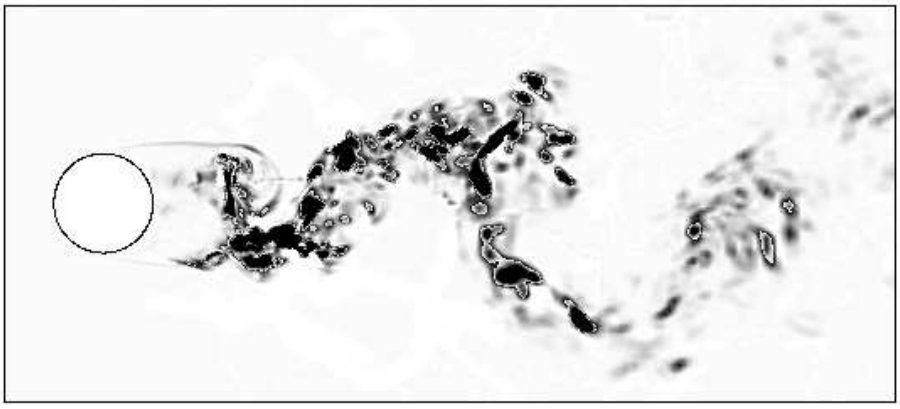

Figure 4.17: Cylinder flow - $Re_D = 3900$: Instantaneous contours of Germano-identity error whose contours vary as: $0 \leq (GIE/U_\infty^2)^2 \leq 0.001$.

which reduces GIE. Note that GIE follows the dominant structures in the flow and hence it is reasonable that Lagrangian averaging uses a time scale based on a correlation of the GIE.

Comparison between T_{SC} and T_{LDSM}

The differences between statistics computed using T_{SC} and T_{LDSM} can be attributed to the contribution of the SGS model. Typically, in the near wake of the cylinder (upto $x/D \sim 2$), the cross-extent of eddy viscosity is within two diameters but the peak value around the centerline is still significant (fig. 4.18). It spreads beyond three diameters after $x/D = 5$ and has a significant impact on the computed flow at $x/D = 10$ and beyond. Figs. 4.18-4.19 also show differences in the computed eddy viscosity using different Lagrangian time scales. Eddy viscosity computed using T_{LDSM} (dashed) is consistently higher than using T_{SC} (solid). This explains the underprediction of the mean u-velocity in the near-field and hence the overprediction of the recirculation region (L_{rec}/D in table 4.3) using T_{LDSM}. Fig. 4.19 shows that the centerline eddy viscosity is significant in the near wake and keeps increasing almost linearly with downstream distance after $x/D = 10$. The centerline eddy viscosity computed using T_{LDSM} is also greater than that using T_{SC} for $x/D > 1.5$. Hence increased accuracy of the results using T_{SC} could be attributed to reduced eddy viscosity in the shear layer. A similar observation was also made by Meneveau et al. [11] attributing the improved accuracy

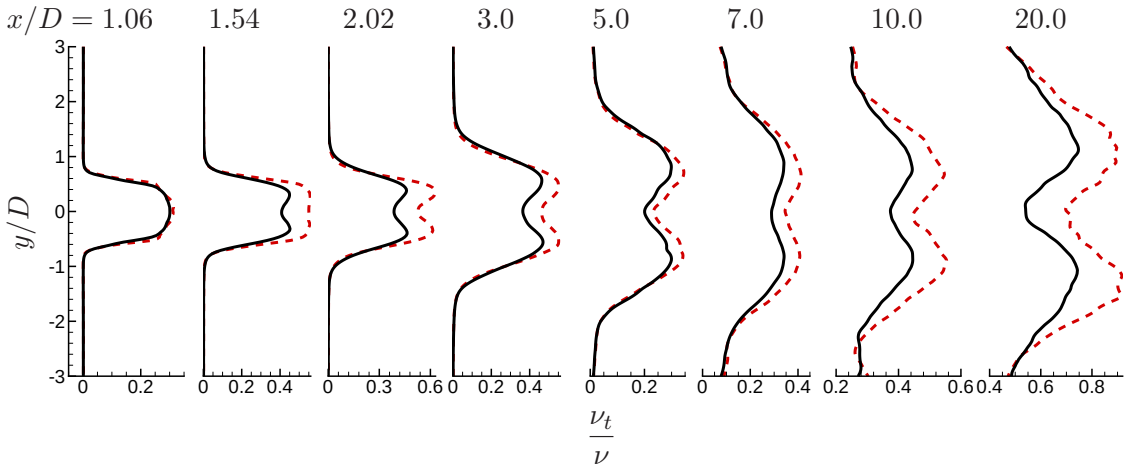

Figure 4.18: Profiles of the mean eddy viscosity at streamwise stations in the cylinder wake at $Re_D = 3900$. ——— : T_{SC}; - - - - : T_{LDSM}.

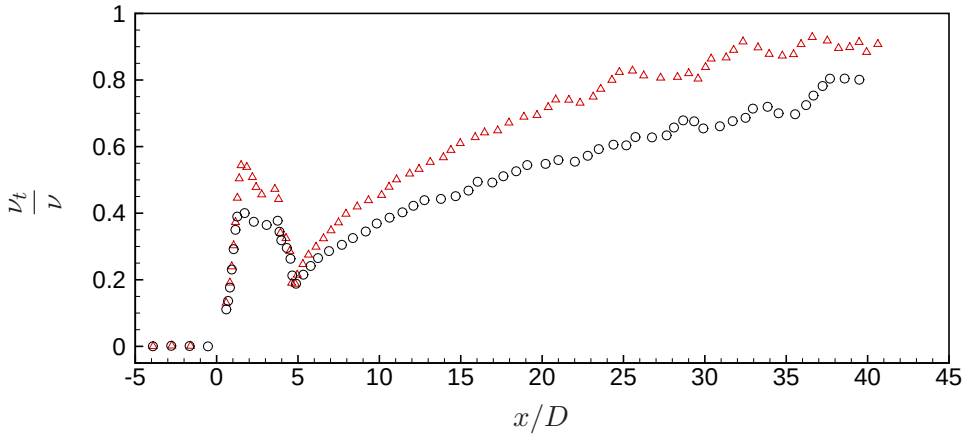

Figure 4.19: Downstream evolution of the mean eddy viscosity on the centerline of the cylinder wake at $Re_D = 3900$. ○ : T_{SC}; △ : T_{LDSM}.

of Lagrangian averaging over the plane averaged dynamic model for channel flow to reduced eddy viscosity in the buffer layer.

Differences in the computed eddy viscosity arise due to different time scales for Lagrangian averaging of the DSM terms. Both T_{SC} and T_{LDSM} are found to increase almost linearly downstream after $x/D > 5$ as shown in fig. 4.20, though for different reasons. Based on the surrogate correlation of the GIE, increasing T_{SC} is consistent with the flow structures becoming bigger as they advect downstream. Whereas, the

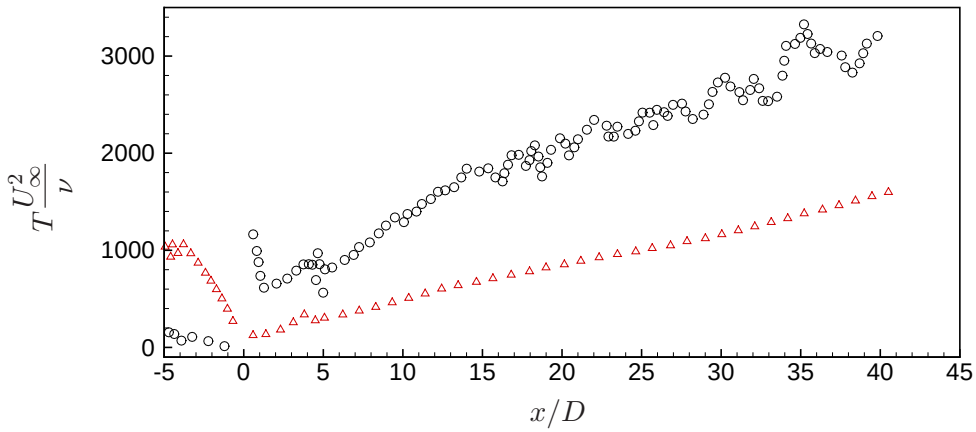

Figure 4.20: Downstream evolution of the Lagrangian time scale on the centerline of the cylinder wake at $Re_D = 3900$. ○ : T_{SC}; △ : T_{LDSM}.

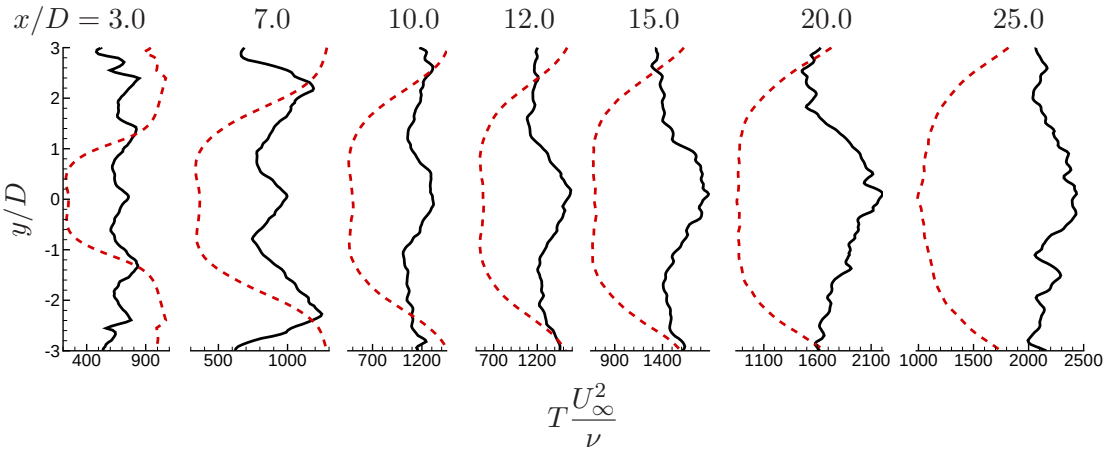

Figure 4.21: Profiles of the Lagrangian time scale at streamwise stations in the cylinder wake at $Re_D = 3900$. —— : T_{SC}; - - - - : T_{LDSM}.

strong dependence of T_{LDSM} on the strain rate though $\mathcal{I}_{LM}$ and $\mathcal{I}_{MM}$ gives it a linear profile both ahead of and behind the cylinder. It can be argued that perhaps a different value of the relaxation factor θ would be more appropriate for this flow. In fact, fig. 4.20 suggests scaling the value of θ by a factor of two or so ($\theta \geq 3.0$) will result in T_{LDSM} being close to T_{SC} after $x/D > 5$. Recall that for turbulent channel flow (end of section 4.3.1), T_{SC} actually overlaps with $T_{LDSM}, \theta = 3.0$ for almost half the channel width, therefore suggesting $\theta = 3.0$ to be a preferable alternative to $\theta = 1.5$. However, it is

	$\langle K_T \rangle$	$\langle K_Q \rangle$	$\langle K_S \rangle$	$\sigma(K_S)$	$\sigma(K_F)$
LES	-0.358	-0.067	0.046	0.024	0.037
Experiment [26]	-0.340	-0.060	0.044 - 0.048	0.019 - 0.021	0.035 - 0.041

Table 4.4: Computed and experimental values of mean and rms of coefficient of thrust K_T, torque K_Q, side-force magnitude K_S, and rms of side-force K_F on propeller blades.

clear that T_{LDSM} would still not show the appropriate trend ahead of the cylinder and in the recirculation region. Note that T_{SC} is high just behind the cylinder ($x/D \sim 1$) in the recirculation region and low in the high acceleration region ahead of the cylinder, as is to be expected on intuitive grounds.

When the variation in the cross-direction is considered (fig. 4.21), T_{SC} is relatively high in the wake centerline which is consistent with the relatively low momentum flow directly behind the cylinder. T_{LDSM} shows the opposite behavior as it is low in the centerline, consistent with a higher strain rate. Again, this opposite trend cannot be changed by a different value of θ.

4.3.3 Marine propeller in crashback

The LES of crashback in marine propellers in chapter 3 were performed at the advance ratios $J = -1.0$ and $J = -0.5$ using locally-regularized DSM (eq. 2.14). This section shows the result of applying the Lagrangian averaged DSM (eq. 4.3) with the proposed dynamic time scale (eq. 4.10) to propeller crashback with an upstream hull at $J = -0.7$. The numerical method, computational grid and boundary conditions are the same as described in sec. 3.2.

Performance of T_{SC}

Time averaged statistics of flow field are computed over 70 propeller rotations. Table 4.4 shows the predicted mean and rms of the unsteady forces and moments on the blades to be in reasonable agreement with the experiment of Bridges et al. [26]. The time averaged flow statistics are further averaged along planes of constant radius to yield circumferentially averaged statistics in the $x-r$ plane; these are used in the subsequent discussion.

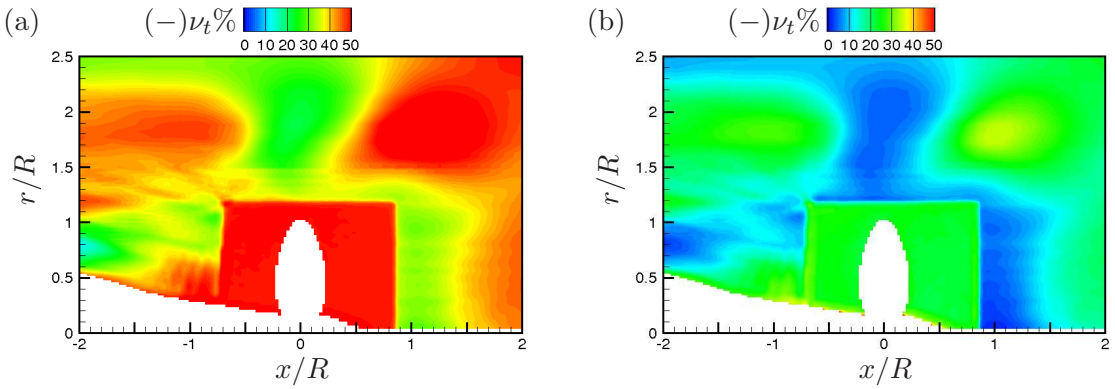

Figure 4.22: Propeller in crashback. Percentage of negative values of eddy viscosity with (a) no averaging, (b) Lagrangian averaging.

The idea of Lagrangian averaging for DSM was introduced by Meneveau et al. [11] to allow regularization of the DSM terms without resorting to averaging along homogeneous directions. The need for regularization becomes apparent in inhomogeneous flows such as the flow past a marine propeller. Fig. 4.22(a) shows that if no averaging is performed for the DSM terms, large regions of the flow see negative eddy viscosities (ν_t) for more than 50% of the computed time steps. The negative ν_t values are more prevalent in the regions with unsteady flow, such as the ring vortex, wake of the hull, and the tetrahedral grid volumes in the vicinity of the propeller blades. On the other hand, fig. 4.22(a) shows that regularization is achieved through Lagrangian averaging. The same unsteady regions of the flow experiencing negative ν_t values are greatly reduced.

Fig. 4.23 compares the Lagrangian time scales T_{SC} and T_{LDSM}. Note that the computations are done using T_{SC} and T_{LDSM} is computed *a posteriori*. The streamlines reveal a vortex ring, centered near the blade tip. A small recirculation zone is formed on the hull ($x/R \sim -1.3$) due to the interaction of the wake of the hull with the reverse flow induced into the propeller disk by the reverse rotation of the propeller. Compared to $J = -1.0$ [53], this recirculation zone is smaller and located slightly upstream of the blades. This is consistent with a higher rotational rate of the propeller inducing a higher reverse flow into the propeller disk. The location of this recirculation region is intermediate to its locations at $J = -1.0$ and $J = -0.5$ [53], as would be expected.

T_{SC} is seen to be varying locally with the flow features. It is high in the low-momentum wake behind the propeller where flow structures are expected to be more

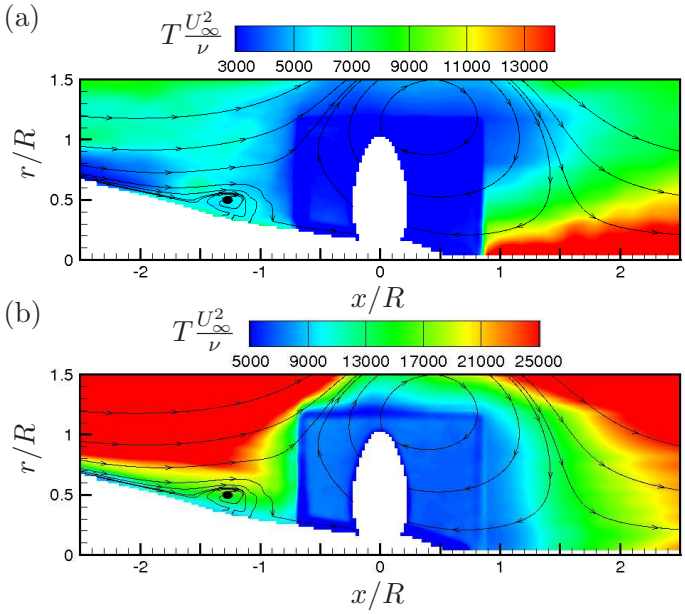

Figure 4.23: Propeller in crashback. Contours of Lagrangian time scale with streamlines, (a) T_{SC}, (b) T_{LDSM}.

coherent. It is low in the unsteady vortex ring region around the propeller blades. The cylindrical region around the blades is where the grid transitions from tetrahedral to hexahedral volumes. Interestingly, T_{SC} is higher in the small recirculation region on the hull. Whereas, T_{LDSM} does not show such level of local variation. It varies smoothly from low values on the hull body and the unsteady region around the propeller blades to higher values away from the propeller. The recirculation region on the hull and the propeller wake do not see a time scale much different from their neighborhood. The performance and physical consistency of T_{SC} for such complex flows is encouraging.

4.4 Summary

A dynamic Lagrangian averaging approach is developed for the dynamic Smagorinsky model for large eddy simulation of complex flows on unstructured grids. The standard Lagrangian dynamic model of Meneveau et al. [11] uses a Lagrangian time scale (T_{LDSM}) which contains an adjustable parameter θ. We extend to unstructured grids, the dynamic time scale proposed by Park and Mahesh [10], which is based on a "surrogate-correlation" of the Germano-identity error (GIE). Park and Mahesh [10] computed their

time scale for homogeneous flows by averaging along homogeneous planes in a spectral structured solver. The present work proposes modifications for inhomogeneous flows on unstructured grids. This development allows the Lagrangian averaged dynamic model to be applied to complex flows on unstructured grids without any adjustable parameter. It is shown that a "surrogate-correlation" of GIE based time scale is a more apt choice for Lagrangian averaging and predicts better results when compared to other averaging procedures for DSM. Such a time scale also removes the strong dependency on strain rate exhibited by T_{LDSM}. To keep computational costs down in a parallel unstructured code, a simple material derivative relation is used to approximate GIE at different events along a pathline instead of multi-linear interpolation.

The model is applied to LES of turbulent channel flow at various Reynolds numbers and relatively coarse grid resolutions. Good agreement is obtained with unfiltered DNS data. Improvement is observed when compared to other averaging procedures for the dynamic Smagorinsky model, especially at coarse resolutions. In the standard Lagrangian dynamic model, the time scale T_{LDSM} is reduced in the high-shear regions where $\mathcal{I}_{MM}$ is large, such as near wall. In contrast, the dynamic time scale T_{SC} predicts higher time scale near wall due to high correlation of GIE and this is consistent with the prevalence of near wall streaks. It also reduces the variance of the computed eddy viscosity and consequently the number of times negative eddy viscosities are computed.

Flow over a cylinder is simulated at two Reynolds numbers. The proposed model shows good agreement of turbulence statistics and power spectral density with previous computations and experiments, and is shown to outperform T_{LDSM}. The significance of using an appropriate Lagrangian time scale for averaging is borne out by significant difference in the computed eddy viscosity which consequently impact the results. Increased accuracy of the turbulent statistics using the proposed model can be attributed to reduced eddy viscosity in the shear layer. GIE is shown to follow the Karman vortex street and the behavior of the resulting time scale also shows consistency with the unsteady separation bubble, recirculation region and increasing size of flow structures in the cylinder wake. Note that Park and Mahesh [10] found that, with their control-based corrected DSM, T_{SC} is lesser than T_{LDSM} in the center of a channel, which increases the weight of the most recent events, making their corrections more effective. This behavior of the time scales is opposite from what we observe from turbulent channel flow (case

590c) and also cylinder flow at $Re_D = 3900$. We observe that $T_{SC} > T_{LDSM}$ near the channel-wall, center, and in the cylinder wake; a higher time scale leads to lower mean eddy viscosity, leading to more resolved stress and hence improved results.

When the model is applied to flow past a marine propeller in crashback, T_{SC} provides the regularization needed for computing eddy viscosity without sacrificing spatial localization. It is also established that T_{SC} is physically consistent with the dominant flow features and produces results in good agreement with experiments. Finally, the extra computational overhead incurred by the proposed Lagrangian averaging is only 2% compared to the cost when no averaging is performed (for case 590c).

Chapter 5

Hybrid Reynolds Stress Constrained SGS Model

5.1 Introduction

The Lagrangian averaged DSM with a dynamic time scale gives better results over existing averaged DSM methods. However, it does not solve the wall modeling problem. Fig. 5.1 shows that the GIE from the 3 cases 590tl, 1ktl, and 2ktl (which use relatively 'wall-resolved' grids) from sec. 4 is still high in the near-wall region; the error increases as the grid coarsens. This is indicative of greater SGS modeling errors near the wall, especially when coarser near-wall grids are employed for LES. It is well known that LES with simple eddy viscosity model works poorly under such circumstances [54–56]. This is primarily due to the fact that near the wall, flow structures scale in viscous units. If the near-wall grid is constructed to resolve the large or integral length scales of the flow, these dynamically important near-wall structures remain unresolved. Moreover, near-wall flow structures tend to be anisotropic and simple SGS models fail to accurately represent the turbulent stress near the wall. It has been estimated that the grid requirement for a wall-resolved LES scales as Re_τ^2 [57]; comparable to that for a DNS which scales as $Re_\tau^{9/4}$. In order to overcome this severe resolution requirement, various wall modeling approaches have been suggested and summarized in some excellent review articles [58, 59]. One such approach is that of hybridizing Reynolds Averaged Navier-Stokes (RANS) and LES formulations. The present work is motivated by (1)

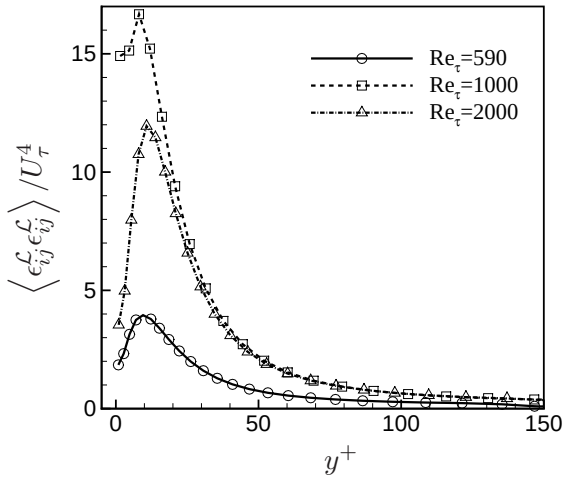

Figure 5.1: Turbulent channel flow: Germano-identity error near the wall from cases 590tl, 1ktl, and 2ktl of sec. 4.

the inherent limitations of the existing hybrid RANS-LES methodologies and (2) the challenges in implementing a robust hybrid RANS-LES framework for complex flows on unstructured grids. A brief review of the limitations of existing hybrid RANS-LES approaches is presented in the next section.

5.1.1 Hybrid RANS-LES approaches

The idea of hybridization of RANS and LES methodologies has been investigated by numerous investigators. Schumann [60] had elements of a hybrid approach which used averaged N-S equations as a near-wall model for LES. Speziale [61] proposed SGS models that allow DNS to transition smoothly to an LES to Very LES (VLES) to RANS depending on the computational grid. Along the lines of Speziale's original idea is Batten *et. al.*'s Limited Numerical Scales (LNS) [62] and Girimaji's Partially Averaged Navier-Stokes (PANS) model [63]. The most successful approach however has been the Detached-Eddy Simulation (DES) by Spalart et al. [64] for high Reynolds number complex flows.

The near-wall region of a high Reynolds number wall-bounded flow is more appropriately modeled by RANS than a coarse grid LES whose filter width is greater than the integral scale of the turbulence. DES uses a limiter based on wall distance and local grid

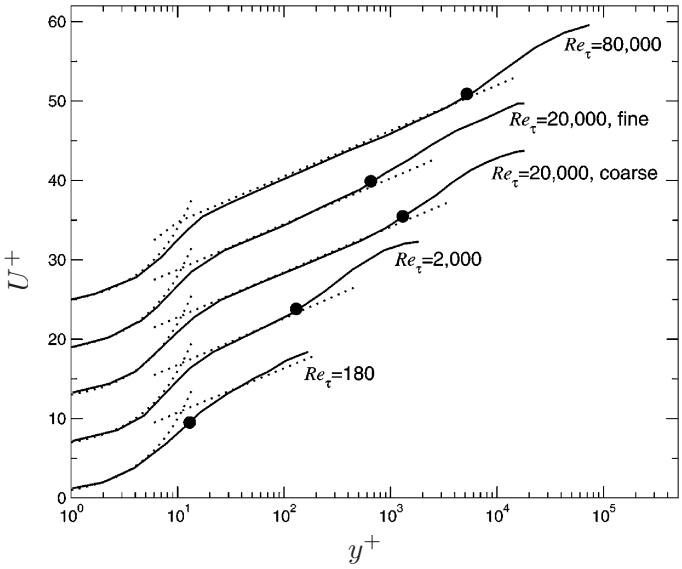

Figure 5.2: Mean velocity profiles in plane channel flow with DES-based wall model by Nikitin et al. [65]. Bullet shows the interface between the RANS and LES regions. (reproduced from Piomelli and Balaras [58]).

spacing to transition from RANS to LES. The idea is to compute the boundary layer ('attached' region) using RANS and use LES away from the wall (in the 'separated' region). DES showed moderate success for external flows with massive separation for which it was originally conceived. However, over the years, it has had to evolve to address various issues arising out of different grid and flow situations. Menter and Kuntz [66] found that DES suffered from grid-induced separation where the grid was small enough for the DES limiter to be activated but not small enough for proper LES. This was alleviated in the Delayed DES (DDES) by Spalart et al. [67] where dependency on the solution was introduced to prolong the RANS region near the wall and delay separation. DES was also found to have a zonal interface problem when applied to non-separating boundary layer. Nikitin et al. [65] showed that when applied to turbulent channel flow, DES results show unnatural change of the slope of the mean velocity at the zonal interface in the log layer (fig. 5.2). This log-layer mismatch is explained by the absence (or lack) of resolved scale fluctuation in the RANS zone and resolved by stochastic forcing in the interface region [68]. The Improved Delayed DES (IDDES) due to Shur et al. [69] addresses the log-layer mismatch by stimulating instabilities in the

zonal interface.

Another hybrid RANS-LES approach is constructed by coupling separate RANS and LES flow solvers which are running on separate domains of a complex geometry. Apart from the huge challenge in the implementation of the coupling of two separate solvers in a parallel computing framework [70], flow information needs to be exchanged at the RANS-LES interface as boundary conditions. Areas where problems arise are boundary conditions for the RANS turbulence model and those for the LES solver, especially since the RANS region has no temporal fluctuations [71].

5.1.2 An ideal RANS-LES zonal simulation

Since this zonal interface problem might be the main drawback of a hybrid approach, further investigation is performed to determine whether it is an inherent problem or it is caused by curable reasons like modeling/numerical error or switch design. To this end, an ideal zonal simulation of turbulent channel flow is considered, whose governing equation is:

$$\begin{aligned} \frac{\partial u_i}{\partial t} + \frac{\partial u_i u_j}{\partial x_j} &= -\frac{\partial p}{\partial x_i} + \frac{1}{Re}\nabla^2 u_i - F_i, \\ F_i &= \begin{cases} \frac{\partial \tau_{ij}}{\partial x_j}, & y \geq \delta_z \\ \sigma(u_i - U_{\mathrm{RANS}}), & y < \delta_z \end{cases} \\ \frac{\partial u_i}{\partial x_i} &= 0, \end{aligned} \tag{5.1}$$

where δ_z is the zonal interface location, U_{RANS} denotes the exact mean velocity from RANS, σ is a forcing coefficient. Reynolds number is $Re_\tau = u_\tau \delta/\nu$ where u_τ denotes friction velocity, δ channel half-width and ν viscosity. Case 590spec is simulated (described later in table 4.1) and the details of the Pseudo-spectral numerical method used are in B. The forcing term F_i enforces the RANS solution and attenuates fluctuations for $y < \delta_z$. Therefore, this region corresponds to an ideal RANS region in the zonal simulation. Since there is no forcing in the region $y \geq \delta_z$, this region corresponds to an LES zone. Mean velocity profile and root-mean-square (rms) velocity fluctuations for this simulation is shown in fig. 5.3. Though more exaggerated, the predicted mean velocity shows the same jump across the boundary as shown in the DES of Nikitin et al. [65]. Baggett [72] argues that the velocity jump is unavoidable to balance the rapid jump

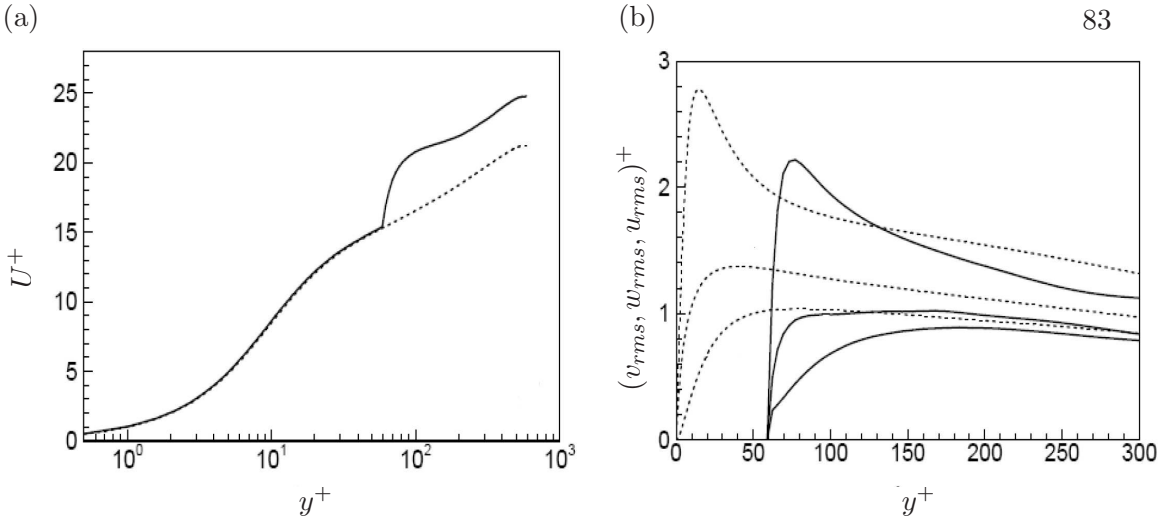

Figure 5.3: Mean statistics from turbulent channel flow at $Re_\tau = 590$: (a) mean velocity, (b) rms velocity fluctuations. ····· DNS of Moser et al. [40]; —— ideal RANS-LES zonal simulation with $\delta_z^+ = 60$.

of Reynolds stress in the log layer. Also, this approach creates false wall-turbulence starting at the zonal interface that has striking similarity with true wall–turbulence (fig. 5.3(b)).

5.1.3 Proposed hybridization approach

The zonal simulation leads to the conclusion that using a RANS model directly in the near-wall region produces excessive dissipation. A less dissipative 'subgrid-scale model' is needed which leads the solution to a target quantity prescribed from external data only in the mean sense. This target quantity may be the wall stress, Reynolds stress or mean velocity and could be sourced from RANS, DNS, experiments or even empirical closures/fits. The intention is to perform LES in the whole computational domain using a simple yet robust wall model. Away from the wall, in general, LES has relaxed grid requirements and simple eddy viscosity models work well. Hence, the external constraint should be imposed in a limited region near the wall where LES is expected to be erroneous.

This work addresses the 'zonal interface issue' inherent in existing hybrid RANS-LES formulations. It proposes a hybrid framework which 'seamlessly' couples a desired mean behavior near the wall to a 'pure' LES solution away from the wall. Note that the

proposed formulation still provides for LES everywhere in the domain. The chapter is organized as follows. A hybrid dynamic SGS model constrained by externally prescribed Reynolds stress is formulated in sec. 5.2. The results of applying the proposed model to turbulent channel flow at various Reynolds numbers and grids, and their discussion is in sec. 5.3. The applicability of the proposed SGS model as a wall model is studied in sec. 5.4. A summary of this work is presented in sec. 5.5.

5.2 Constrained dynamic SGS model

An advantage of the dynamic procedure is that various terms can be easily incorporated to form dynamic mixed models [33]. The minimization of an objective function yields the various model coefficients in a mixed model. The construct of a minimization problem also allows the incorporation of constraints. Ghosal et al. [30] showed that the averaging and truncation operations on the computed eddy viscosity can be viewed as a constrained minimization of eq. 2.12. Shi et al. [73] imposed an energy dissipation constraint on the dynamic mixed similarity model. Under the ambit of the dynamic procedure, eq. 2.13 can be generalized and the objective function for constrained minimization can be constructed to be of the form:

$$\mathcal{J} = \int_{\Omega} \epsilon_{ij}^{\mathcal{L}} \epsilon_{ij}^{\mathcal{L}} d\mathbf{x} + \omega^{\mathcal{C}} \int_{\Omega} \epsilon_{ij}^{\mathcal{C}} \epsilon_{ij}^{\mathcal{C}} d\mathbf{x}, \tag{5.2}$$

where $\epsilon_{ij}^{\mathcal{L}}$ is a measure of the error in the LES model, $\epsilon_{ij}^{\mathcal{C}}$ is a constraint which is desired to be satisfied, $\omega^{\mathcal{C}}$ is a weighting function, and $\mathcal{L}$ and $\mathcal{C}$ denote LES and constraint respectively.

For the scope of the present work, only Reynolds stress is considered to be provided as a constraint. More particularly, only a time average of the Reynolds stress needs to be provided and hence it could be sourced from RANS, DNS, experimental statistics or even empirical closures/fits. A simple and efficient hybrid SGS model is proposed in the next sub-section that incorporates Reynolds stress constraints into the dynamic procedure. This idea was first introduced by Park and Mahesh [74].

5.2.1 Reynolds stress constrained DSM

Performing an ensemble average of the momentum LES equations (eq. 2.5) results in:

$$\frac{\partial\langle\overline{u}_i\rangle}{\partial t}+\frac{\partial}{\partial x_j}(\langle\overline{u}_i\rangle\langle\overline{u}_j\rangle)=-\frac{\partial\langle\overline{p}\rangle}{\partial x_i}+\nu\frac{\partial^2\langle\overline{u}_i\rangle}{\partial x_j\partial x_j}-\frac{\partial}{\partial x_j}(\langle\overline{u}_i\overline{u}_j\rangle-\langle\overline{u}_i\rangle\langle\overline{u}_j\rangle+\langle\tau_{ij}\rangle), \tag{5.3}$$

where $\langle\cdot\rangle$ denotes an ensemble average, equivalent to $(\cdot)_{t,h}$ = (temporal + spatial averaging in homogeneous directions, if any). Note that $\langle r_{ij}\rangle=\langle\overline{u}_i\overline{u}_j\rangle-\langle\overline{u}_i\rangle\langle\overline{u}_j\rangle$ is the resolved Reynolds stress. Under the Ergodic assumption that $\langle\overline{u}_i\rangle=\langle u_i\rangle$ and $\langle\overline{p}\rangle=\langle p\rangle$, eq. 5.3 can be compared with the RANS equations (eq. B.2) to yield:

$$\langle r_{ij}\rangle+\langle\tau_{ij}\rangle=\mathcal{R}_{ij}, \tag{5.4}$$

where the RANS Reynolds stress $\mathcal{R}_{ij}=\langle u_iu_j\rangle-\langle u_i\rangle\langle u_j\rangle$ is assumed to be available from an external source. The above condition that the ensemble average of the sum of the resolved and SGS stress be equal to the RANS Reynolds stress is desired to be imposed as a constraint.

However, imposition of this condition to unsteady simulation is not straightforward. Using an SGS stress model τ_{ij}^M, the error in eq. 5.4 is ensemble-averaged upto the current time t and written instantaneously as:

$$\epsilon_{ij}^{\mathcal{R}}=\langle\overline{u}_i\overline{u}_j\rangle_t-\langle\overline{u}_i\rangle_t\langle\overline{u}_j\rangle_t+\langle\tau_{ij}^M\rangle_t-\mathcal{R}_{ij}, \tag{5.5}$$

where $\epsilon_{ij}^{\mathcal{R}}$ is the error (and $\mathcal{R}$ denotes RANS), and $\langle(\cdot)\rangle_t=\frac{1}{t}\sum_0^t(\cdot)$ is cumulative, ensemble-averaged up to current time t. When t is sufficiently large, $\epsilon_{ij}^{\mathcal{R}}$ in eq. 5.5 represents deviation from eq. 5.4 due to SGS modeling error. Thus, the minimization of $\epsilon_{ij}^{\mathcal{R}}$ seems to be a proper RANS constraint.

Thus, following eq. 5.2, the cost function to be minimized can take the form

$$\mathcal{J}=\int_\Omega\epsilon_{ij}^{\mathcal{L}}\epsilon_{ij}^{\mathcal{L}}d\mathbf{x}+\omega^{\mathcal{R}}\int_\Omega\epsilon_{ij}^{\mathcal{R}}\epsilon_{ij}^{\mathcal{R}}d\mathbf{x}, \tag{5.6}$$

where Ω is the domain, $\epsilon_{ij}^{\mathcal{L}}$ is the LES (Germano-identity) error and $\omega^{\mathcal{R}}$ is the weight function for RANS constraints. For the sake of brevity, $(C_s\Delta)^2$ is denoted as C_s henceforth. Considering a one-parameter SGS model $\tau_{ij}^M=\tau_{ij}^M(C_s)$, the optimal C_s is given

by:

$$\delta\mathcal{J}\left(C_s\right) = \int_{\Omega} \frac{\partial}{\partial C_s}\left[\epsilon_{ij}^{\mathcal{L}}\epsilon_{ij}^{\mathcal{L}} + \omega^{\mathcal{R}}\epsilon_{ij}^{\mathcal{R}}\epsilon_{ij}^{\mathcal{R}}\right]\delta C_s d\mathbf{x} = 0, \tag{5.7}$$

which implies that

$$\frac{\partial}{\partial C_s}\left[\epsilon_{ij}^{\mathcal{L}}\epsilon_{ij}^{\mathcal{L}} + \omega^{\mathcal{R}}\epsilon_{ij}^{\mathcal{R}}\epsilon_{ij}^{\mathcal{R}}\right] = 0. \tag{5.8}$$

Eq. 5.8 is a general relation that can be used for complex flows and one-parameter SGS models. Averaging along homogeneous directions or pathlines can be incorporated by considering ω to be the averaging domain and by assuming C_s to be constant in ω.

Substituting GIE from eq. 2.12 in the first term of the above eq. 5.8 leads to:

$$\frac{\partial}{\partial C_s}\left[\epsilon_{ij}^{\mathcal{L}}\epsilon_{ij}^{\mathcal{L}}\right] = 2C_s(M_{ij}M_{ij}) - 2(L_{ij}M_{ij}). \tag{5.9}$$

Clearly, equating eq. (5.9) to zero results in the standard DSM (eq. 2.14). Next, the RANS Reynolds-stress reconstruction error (eq. 5.5) is considered by substituting the Smagorinsky model for τ_{ij}^{M} (eq. 2.8):

$$\begin{aligned}
\epsilon_{ij}^{\mathcal{R}} &= \langle r_{ij}\rangle_t - 2\langle C_s|\overline{S}|\overline{S}_{ij}\rangle_t - \mathcal{R}_{ij} \\
&\approx \langle r_{ij}\rangle_t - 2C_s\left\langle|\overline{S}|\overline{S}_{ij}\right\rangle_t - \mathcal{R}_{ij} \\
&= \underbrace{\langle r_{ij}\rangle_t - \mathcal{R}_{ij}}_{A_{ij}} - \underbrace{2\left\langle|\overline{S}|\overline{S}_{ij}\right\rangle_t}_{B_{ij}} C_s \\
&\equiv A_{ij} - B_{ij}C_s,
\end{aligned} \tag{5.10}$$

where $\langle r_{ij}\rangle_t = \langle\overline{u}_i\overline{u}_j\rangle_t - \langle\overline{u}_i\rangle_t\langle\overline{u}_j\rangle_t$ and C_s is taken out of the $\langle\cdot\rangle_t$ operator. Similar to eq. 5.9, the second term of eq. 5.8 is:

$$\frac{\partial}{\partial C_s}\left[\epsilon_{ij}^{\mathcal{R}}\epsilon_{ij}^{\mathcal{R}}\right] = 2C_sB_{ij}B_{ij} - 2A_{ij}B_{ij}. \tag{5.11}$$

Inserting eqs. (5.9) and (5.11) in eq. (5.8) yields the constrained SGS model coefficient C_s as:

$$C_s = \frac{L_{ij}M_{ij} + \omega^{\mathcal{R}}A_{ij}B_{ij}}{M_{ij}M_{ij} + \omega^{\mathcal{R}}B_{ij}B_{ij}}. \tag{5.12}$$

Note that this approach/formulation to perform Reynolds stress constrained LES is different from that of Chen et al. [75] who directly compute the SGS stress in the inner

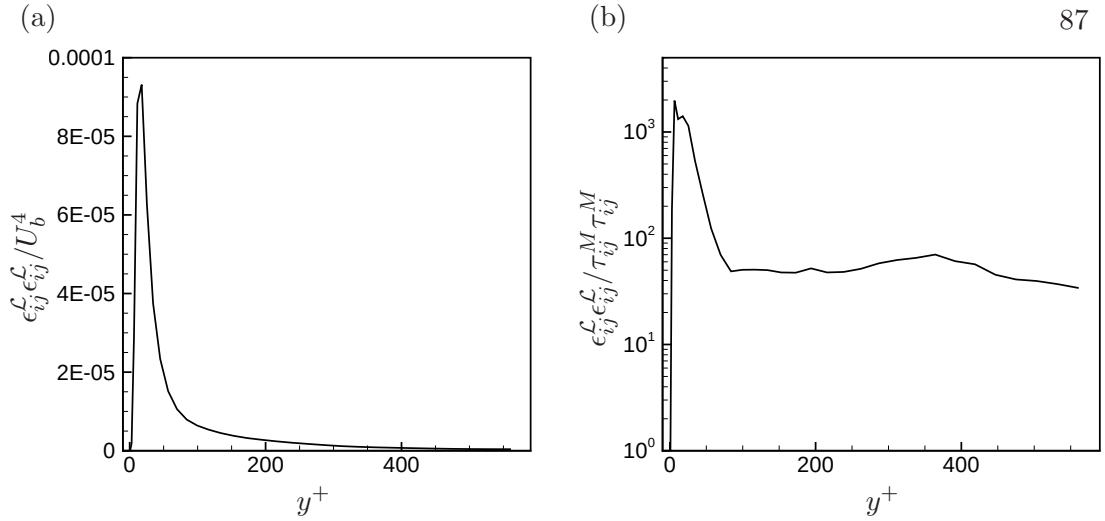

Figure 5.4: Turbulent channel flow at $Re_\tau = 590$ - Case 590spec: Germano-identity error normalized by, (a) bulk velocity U_b, (b) modeled subgrid stress.

.

layer based on the Reynolds stress constraint and a 'fluctuating' model coefficient C_s'. Another major difference is in the definition of the interface separating the constrained LES region from the non-constrained LES region. Chen et al. [75] prescribe an interface at the bottom of the logarithmic layer for turbulent channel flows and suggest adopting a DES-type interface for complex flows. A dynamic procedure to determine the interface is described in the next sub-section.

5.2.2 Dynamic determination of $\omega^{\mathcal{R}}$

In principle, the expression for C_s in eq. 5.12 is applicable throughout the flow. However, as mentioned earlier, the intention is to apply the external constraint only in a limited region where LES is expected to be erroneous. Fig. 4.5(a) shows that instantaneously, the Germano-identity error (GIE) is high near the wall and in fact manifests itself in the form of long correlation times near-wall streaks as shown in fig. 4.5(b).

The GIE (eq. 2.12) is proposed as a measure of accuracy of LES utilizing a dynamic Smagorinsky SGS model. In fact, the GIE has been used to compare the performance of different models during LES [33, 76]. Fig. 5.4 shows that time-averaged GIE is very high near the wall so that the validity of the Smagorinsky SGS model (eq. 2.8) in this region can be questioned. The external constraint should be active in such regions where

the GIE is deemed too high; to be determined by the weight function $\omega^{\mathcal{R}}$. Note that, to transition from RANS to LES, DES uses purely grid parameters such as the wall distance and local grid spacing; its variants incorporate some flow information. The current proposal to use GIE is explicitly dependent on the flow and the underlying SGS model.

The Germano-identity error is normalized by the modeled SGS stress as:

$$\mathcal{E} = \epsilon_{ij}^{\mathcal{L}} \epsilon_{ij}^{\mathcal{L}} / \tau_{ij}^{M} \tau_{ij}^{M}. \tag{5.13}$$

The weight function $\omega^{\mathcal{R}}$ is then proposed to be of the form:

$$\omega^{\mathcal{R}} = C_{\omega} \max\left(\mathcal{E} - \mathcal{E}_{\mathrm{t}}, 0\right), \tag{5.14}$$

where C_{ω} is a scaling coefficient and $\mathcal{E}_t$ is the threshold value. Nominally, $C_{\omega} = 0.1$ and $\mathcal{E}_t = 100$ is chosen to impose the constraints in the near-wall region. Separately, the EDQNM analysis of isotropic turbulence also yields $\mathcal{E}_t = 100$. Hence $\omega^{\mathcal{R}} \neq 0$ implies the external constraint is active only in the region where the normalized Germano-identity error $\mathcal{E}$ exceeds a certain threshold $\mathcal{E}_t$. Clearly, $\omega^{\mathcal{R}} = 0$ retrieves the standard DSM (eq. 2.14). Sensitivity of the proposed hybrid model to these two parameters is studied in sec. 5.3.3.

Note that such a form for $\omega^{\mathcal{R}}$ is also consistent with Baggett [72] who proposed that the 'blending' function merging the RANS and LES regions of the flow be a function of the resolution and might be parameterized by the ratio of a measure of the filter width and a measure of the turbulent integral dissipation length. It is however, different from a blending function $\beta : 0 \leq \beta \leq 1$ which transitions from pure LES to RANS eddy viscosity [77].

5.3 Results

LES is performed for turbulent channel flow at various Reynolds numbers $Re_{\tau} = u_{\tau}\delta/\nu$ and grid resolutions as tabulated in table 5.1. Here u_{τ}, δ and ν denote the friction velocity, channel half-width, and viscosity respectively. All cases have uniform spacing in x. Cases 590spec and 590s have uniform spacing in z. The rest have an unstructured

LES							
Case	Re_τ	$N_x \times N_y \times N_z$	$L_x \times L_z$	Δx^+	Δz^+	Δy_w^+	$\Delta y_{cen}/\delta$
590spec		$12 \times 64 \times 16$	$\pi \times \pi/2$	154	58	0.7	0.05
590s	590	$160 \times 64 \times 66$		23.2	28.1	4	0.05
590un		$160 \times 66 \times (150, 100)$		23.2	$12.4, 18.5$	3.5	0.05
1kun	1000	$160 \times 70 \times (150, 100)$	$2\pi \times \pi$	39.3	$21, 31.4$	4	0.05
2kun	2000	$160 \times 74 \times (150, 100)$		78.5	$42, 63$	4	0.05
10kun	10000	$160 \times 90 \times (150, 100)$		393	$209, 314$	4	0.05
DNS							
Moser et al. [40]	587	$384 \times 257 \times 384$	$2\pi \times \pi$	9.7	4.8	-	0.012
del Alamo et al. [41]	934	$- \times 385 \times -$	$8\pi \times 3\pi$	11	5.7	-	-
Hoyas and Jimenez [42]	2003	$- \times 633 \times -$	$8\pi \times 3\pi$	12	6.1	-	-

Table 5.1: Grid parameters for turbulent channel flow.

grid near the wall in the spanwise direction which allows near-wall spacings (scaling with viscosity) independent of outer region spacings. A slightly finer Δz^+ is used near-wall which is then quickly coarsened to the outer region Δz^+ after 11 rows. Away from the wall in the channel center, the grids are constructed to have almost-isotropic cells; the cell size scales with the outer variables and hence are the same for all Re_τ. Also note that the near-wall Δz is the same; only Δy is varied to achieve the same $\Delta y^+_{wall} \approx 4$. This gridding methodology is used for the unstructured grid cases 590un, 1kun, 2kun and 10kun. The LES results are compared to DNS whose grid parameters are also included in the table for comparison. Henceforth, DSM denotes Dynamic Smagorinsky Model (eq. 2.14) and CDSM denotes Constrained DSM which is the proposed Reynolds stress constrained model (eq. 5.12). The proposed model is validated in sec. 5.3.1, the effect of the imposed constraint is studied in 5.3.2, and the sensitivity to model parameters and numerical methods is discussed in sections 5.3.3 and 5.3.4 respectively.

In this chapter, the simulations in sec. 5.3.4 are performed using DSM with averaging along homogeneous directions (eq. 2.14), and using Lagrangian averaged DSM (eq. 4.3) with dynamic Lagrangian time scale (eq. 4.10) elsewhere. The unstructured finite-volume method (sec. 2.4) is used to solve eq. 2.5.

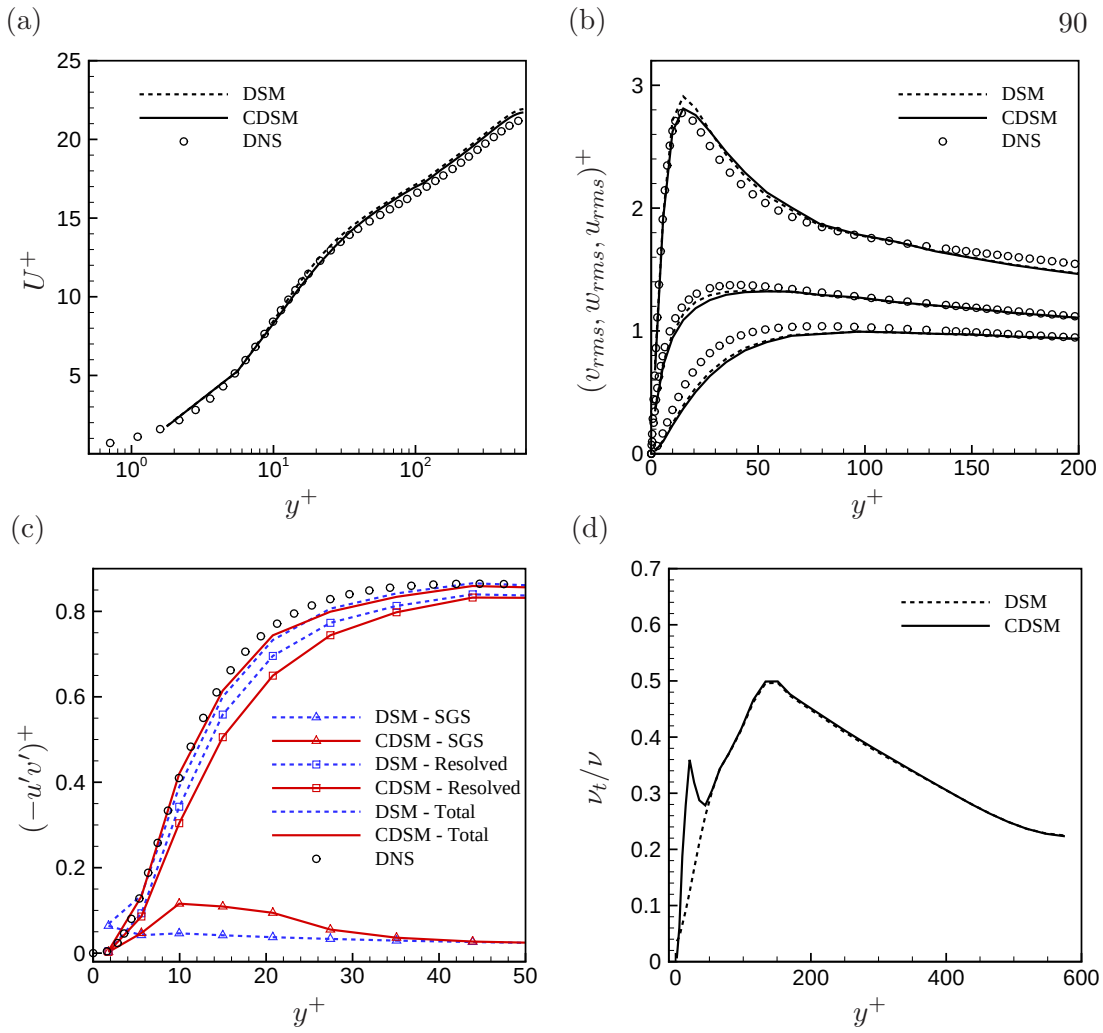

Figure 5.5: Mean statistics from turbulent channel flow at $Re_\tau = 590$ - Case 590un: (a) mean velocity, (b) rms velocity fluctuations, (c) Reynolds stress, (d) eddy-viscosity.

5.3.1 Validation

Results are shown at $Re_\tau = 590$ and 1000 (cases 590un and 1kun) to provide validation for CDSM as an LES model. Fig. 5.5 shows results from case 590un using the ensemble averaged Reynolds shear stress from the DNS of Moser et al. [40] as the constraint. Both DSM and CDSM predict the mean and rms velocity and Reynolds shear stress in good agreement with the DNS of Moser et al. [40]. In fact, CDSM shows a slight improvement over DSM for mean and rms streamwise velocity. Fig. 5.5(c) shows the resolved, modeled and total Reynolds stress for DSM and CDSM. For CDSM, the

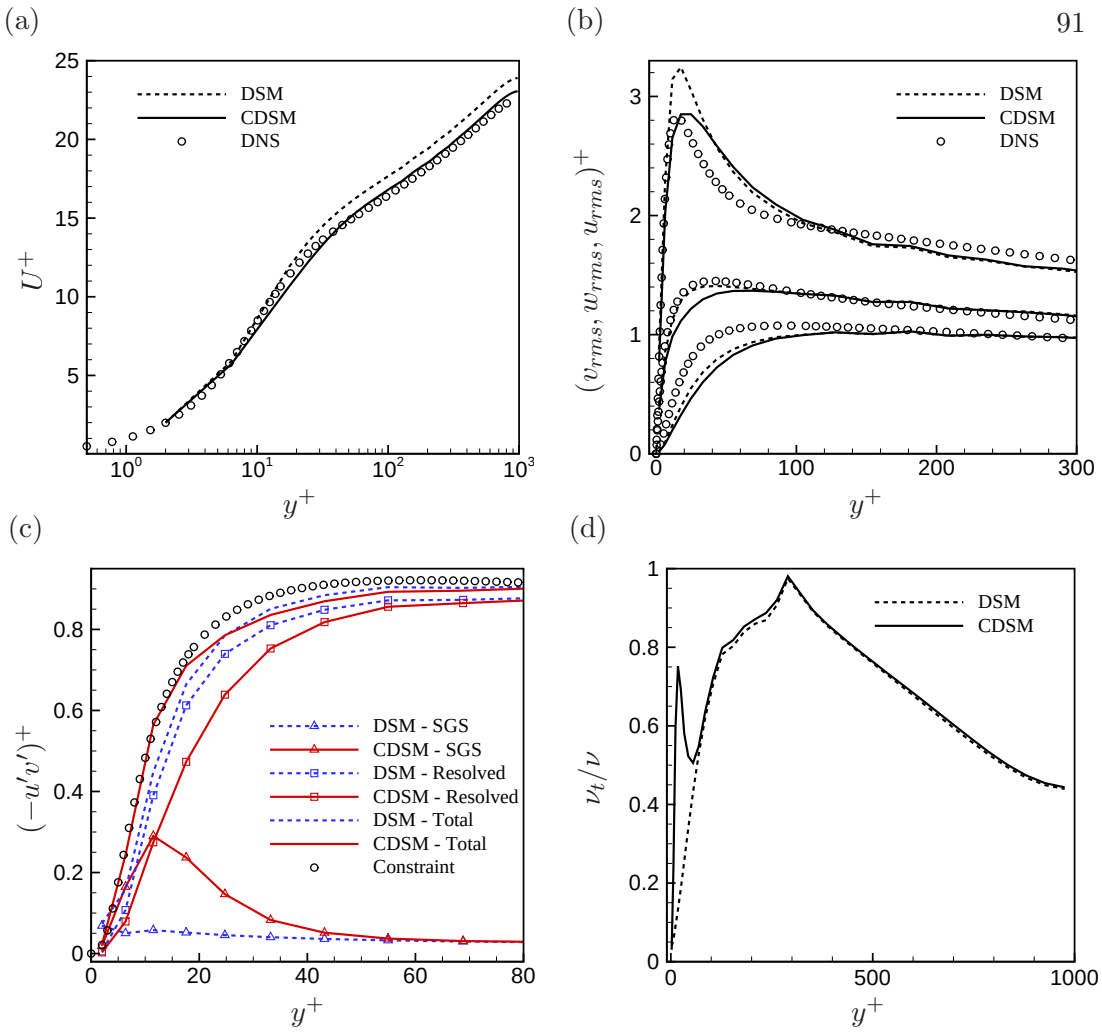

Figure 5.6: Mean statistics from turbulent channel flow at $Re_\tau = 1000$ - Case 1kun: (a) mean velocity, (b) rms velocity fluctuations, (c) Reynolds stress, (d) eddy-viscosity.

resolved shear stress is slightly lower than DSM near the wall but is compensated by higher SGS stress such that the total shear stress is closer to the DNS constraint than DSM. Eddy viscosity computed due to CDSM is higher near the wall than DSM.

Admittedly, the grid resolution for case 590un is adequate for a reasonably resolved LES. In this limit, CDSM offers marginal improvement over DSM. A coarser grid is used for LES at $Re_\tau = 1000$ and results are shown in fig. 5.6 for case 1kun. The mean and rms streamwise velocity and Reynolds shear stress predicted by CDSM is in good agreement with the DNS of del Alamo et al. [41]. The magnitude of peak u_{rms} is better predicted

due to reasonable near-wall Δz^+ even though it is shifted due to coarse near-wall Δy^+. Analogous to case 590un, the computed eddy viscosity is higher near the wall using CDSM which increases the modeled SGS stress, compensating for the reduced resolved Reynolds stress such that the total shear stress is closer to the imposed constraint near the wall (figs. 5.6(c)-(d)). This validates the current hybridization procedure to incorporate mean constraints in an unsteady LES methodology. The mean velocity profile is captured better with CDSM than DSM on coarse grids.

5.3.2 Effect of constraint

As seen in the previous sub-section, the constraint plays a more significant role on coarser grids when the base SGS stress model is unable to compensate adequately for the reduced resolution (for case 1kun). Hence, the effect of the constraint on the solution is studied at $Re_\tau = 590$ for case 590s which is a coarser grid than that was employed to validate the model in the previous sub-section (for case 590un).

Figs. 5.7(a)-(b) show again that CDSM improves the mean velocity and total Reynolds shear stress prediction compared to DSM. Note that increased Δz^+ resolution near the wall was found to improve the mean velocity prediction (case 590un). However, it is clear that minimization of the GIE with a constraint results in a lower GIE near the wall with CDSM as shown in fig. 5.7(c). This indicates that constraining the mean near-wall Reynolds stress to the appropriate value reduces the error inherent in the SGS stress model. Furthermore, fig. 5.7(d) shows that only a few points near the wall have the SGS stress normalized GIE greater than the threshold $\mathcal{E}_t$. Hence the constraint is active only at a few points near the wall ($y^+ < 100$) as can be seen by non-trivial values of the weight function $\omega^{\mathcal{R}} > 0$. The near-wall variation of the terms of eq. 5.12 are plotted in fig. 5.5(e). In the computation of C_s, the term due to the Reynolds stress constraint $\frac{A_{ij}B_{ij}}{B_{ij}B_{ij}}$ is dominant near the wall due to high values of $\omega^{\mathcal{R}}$. Away from the wall as $\omega^{\mathcal{R}} \to 0$, $C_s \to \frac{L_{ij}M_{ij}}{M_{ij}M_{ij}}$. Hence the transition and variation of the hybrid C_s given by eq. 5.12 (denoted by solid red). Increased C_s results in increased eddy viscosity with CDSM (fig. 5.5(f)). The transition of the CDSM ν_t to the DSM ν_t occurs around the same location ($y^+ \sim 80$) where C_s transitions because $\omega^{\mathcal{R}} \to 0$. Also plotted is the RANS eddy viscosity ν_t^+ which is obtained from the non-dimensionalized

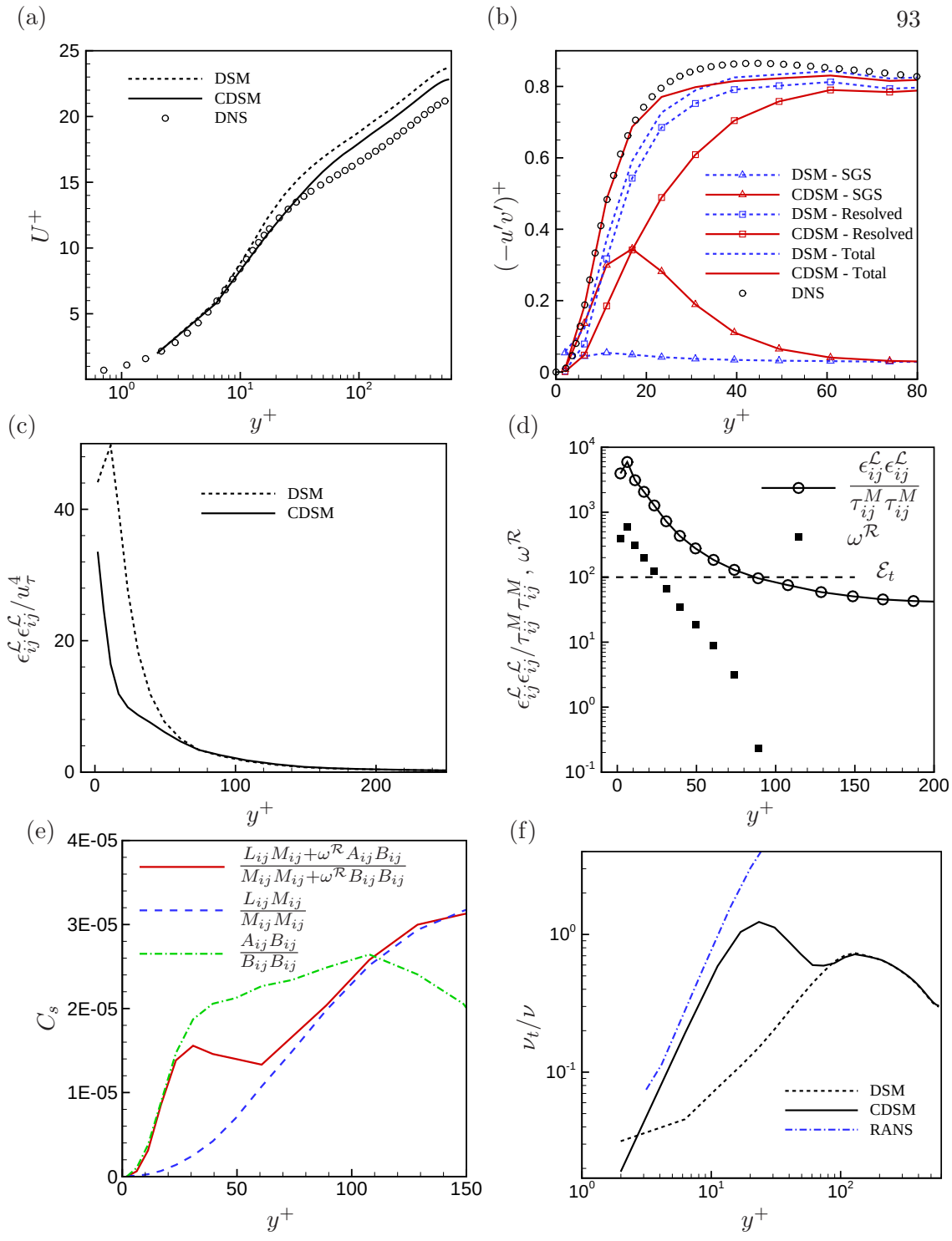

Figure 5.7: Mean statistics from turbulent channel flow at $Re_\tau = 590$ - Case 590s: (a) mean velocity, (b) Reynolds stress, (c) Germano-identity error, (d) weight function, (e) model coefficient, (f) eddy-viscosity.

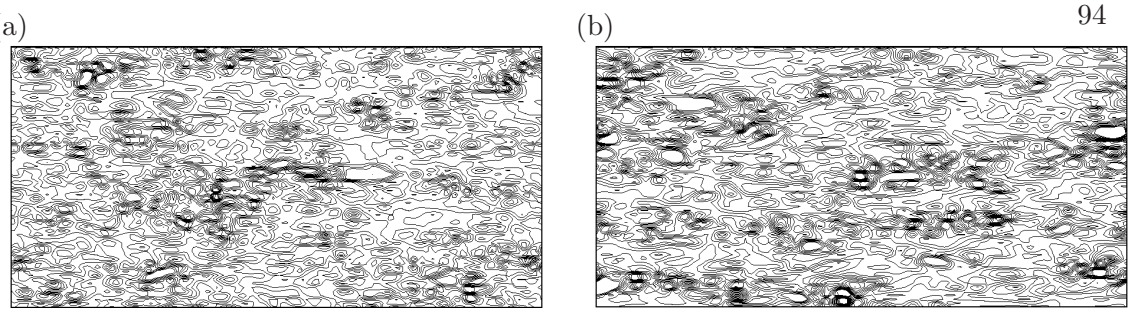

Figure 5.8: Instantaneous contours of streamwise vorticity ω_x in the xz plane at $y^+ = 12$ - Case 590s: (a) DSM, (b) CDSM.

RANS equation for channel flow:

$$(1 + \nu_t^+)\frac{du^+}{dy^+} = 1 - \frac{y^+}{Re_\tau},$$

where du^+/dy^+ is the gradient of the ensemble averaged streamwise velocity from CDSM. Note that the value of ν_t computed using CDSM approaches and has a similar slope as the RANS ν_t near the wall. Templeton et al. [78] provide a relation between the LES and RANS eddy viscosity for channel flow:

$$\overline{\nu}_t^{LES} = \overline{\nu}_t^{RANS} + \frac{\langle \overline{uv} \rangle}{\langle d\overline{u}/dy \rangle},$$

which also predicts that the mean LES eddy viscosity is always less than the RANS eddy viscosity. Such behavior of the CDSM eddy viscosity near the wall indicates that minimization of the RANS Reynolds-stress reconstruction error $\epsilon_{ij}^{\mathcal{R}}$ (eq. 5.5) could also be construed as a near-wall RANS model.

The effect of the near-wall constraint on the instantaneous flow field is assessed in fig. 5.8 which compares streamwise vorticity ω_x in an xz plane near the wall at $y^+ = 12$. Clearly, the small structures are at the same scale for DSM and CDSM. This demonstrates that having an eddy viscosity higher than DSM near the wall did not dissipate away the smaller scales. Different from hybrid RANS/LES methods, Park and Mahesh [10] also reported higher eddy viscosity near the wall and comparable near-wall structures using their control-based DSM which attempts to further minimize the GIE by including the sensitivity of the velocity field to C_s. Hence, the current formulation

is indeed behaving as a large eddy simulation all through the domain and may even be successful in predicting higher order statistics near the wall.

5.3.3 Sensitivity to $\mathcal{E}_t$ and C_ω

Various numerical experiments have been performed to study the sensitivity of CDSM to the threshold $\mathcal{E}_t$ and scaling coefficient C_ω. Fig. 5.7(d) shows that the normalized GIE has a logarithmic variation near the wall. Hence changing $\mathcal{E}_t$ only by factors may add or remove any significant volume to/from the constrained region. It has indeed been observed that changes of the order of this did not make any apparent difference to the statistics. Note that reducing $\mathcal{E}_t$ to levels which would constrain a significant portion of the domain beyond the near-wall region (e.g. $\mathcal{E}_t = 0$) essentially results in $C_s \sim \frac{A_{ij}B_{ij}}{B_{ij}B_{ij}}$ which is not a desirable SGS stress model for LES (but akin to a RANS model near the wall as shown before). Setting $\mathcal{E}_t$ to low values indeed results in spurious solutions. Increasing $\mathcal{E}_t$ leads to the constraint being active in a smaller region and the solution tends towards DSM. For instance in fig. 5.7(d), $\mathcal{E}_t = 100$ results in $\omega^{\mathcal{R}} > 0$ for $y^+ \leq 90$. $\mathcal{E}_t = 1000$ would result in $\omega^{\mathcal{R}} > 0$ for only $y^+ \leq 30$. Unless there is an order of magnitude change in $\mathcal{E}_t$ which would significantly expand or contract the constrained region, it can be said that CDSM is free of sensitivity to a judicious choice of the threshold $\mathcal{E}_t$ limiting it to a small region near the wall. Recall that $\mathcal{E}_t = 100$ is also justified from EDQNM analysis of isotropic turbulence.

Similar to $\mathcal{E}_t$, CDSM is sensitive to only orders of magnitude change in the value of C_ω. Obviously, in the limit $C_\omega \to 0$, CDSM tends to DSM. Increasing C_ω implies a stronger imposition of the constraint over the base SGS stress model. Sensitivity of CDSM to the scaling coefficient C_ω is studied at $Re_\tau = 2000$ and shown in fig. 5.9. The coarse near-wall Δz^+ in case 2kun serves to distinguish the performance of CDSM when C_ω is changed by an order of magnitude ($C_\omega = 0.1$ is increased to 1.0). Stronger imposition of the mean Reynolds stress constraint increases the eddy viscosity near the wall, following the RANS eddy viscosity (fig. 5.9(a)). As can be expected, fig. 5.9(b) shows that the weight function $\omega^{\mathcal{R}}$ is an order of magnitude higher at $C_\omega = 1.0$ than at $C_\omega = 0.1$ and there is a significant drop in GIE near the wall. The increased eddy viscosity leads to higher modeled SGS stress accompanied by a drop in the resolved Reynolds shear stress (fig. 5.9(c)). Since $\omega^{\mathcal{R}}$ is a decade higher at $C_\omega = 1.0$, the total

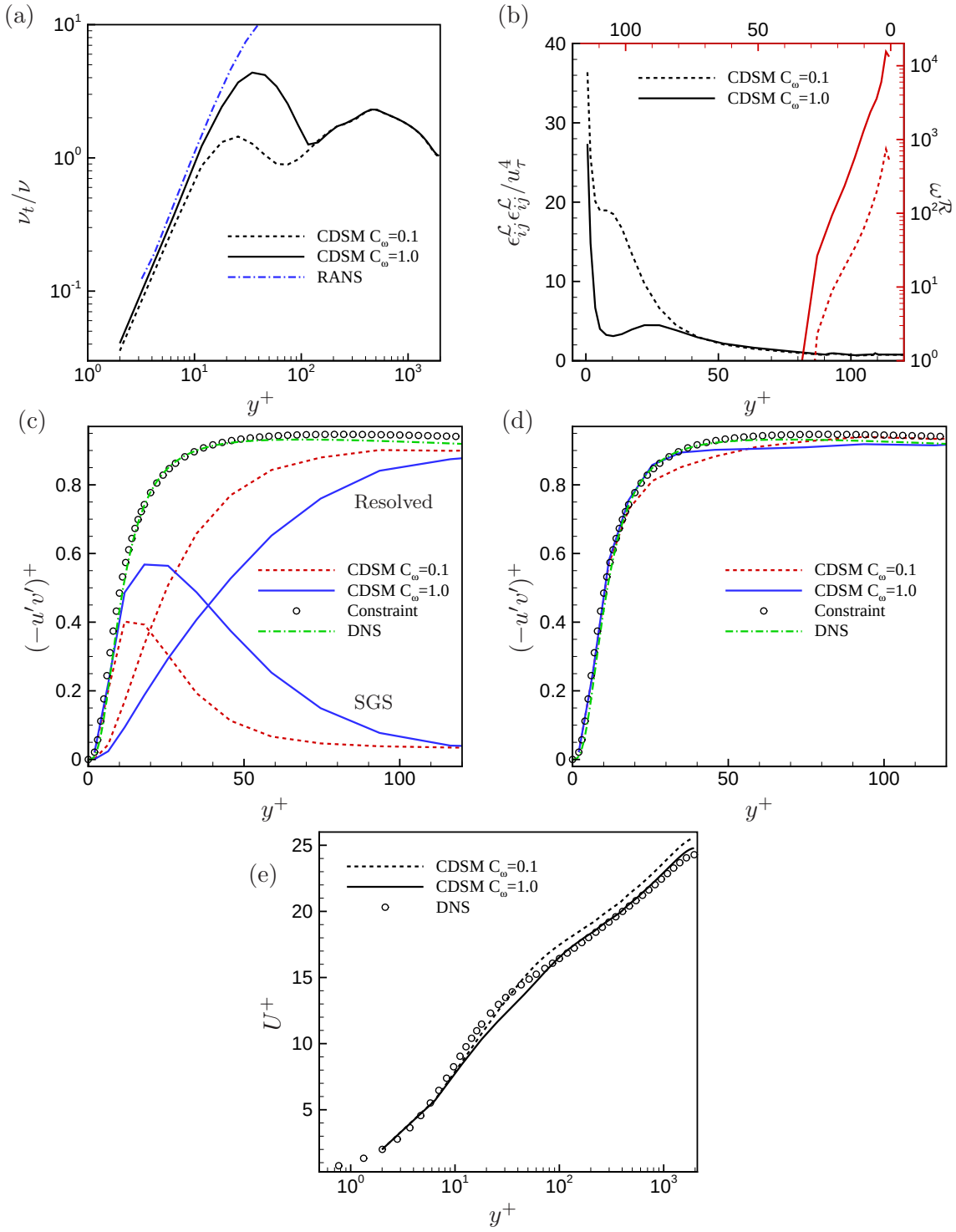

Figure 5.9: Mean statistics from turbulent channel flow at $Re_\tau = 2000$ - Case 2kun: (a) eddy-viscosity, (b) Germano-identity error and weight function, (c) resolved and SGS Reynolds stress, (d) total Reynolds stress, (e) mean velocity.

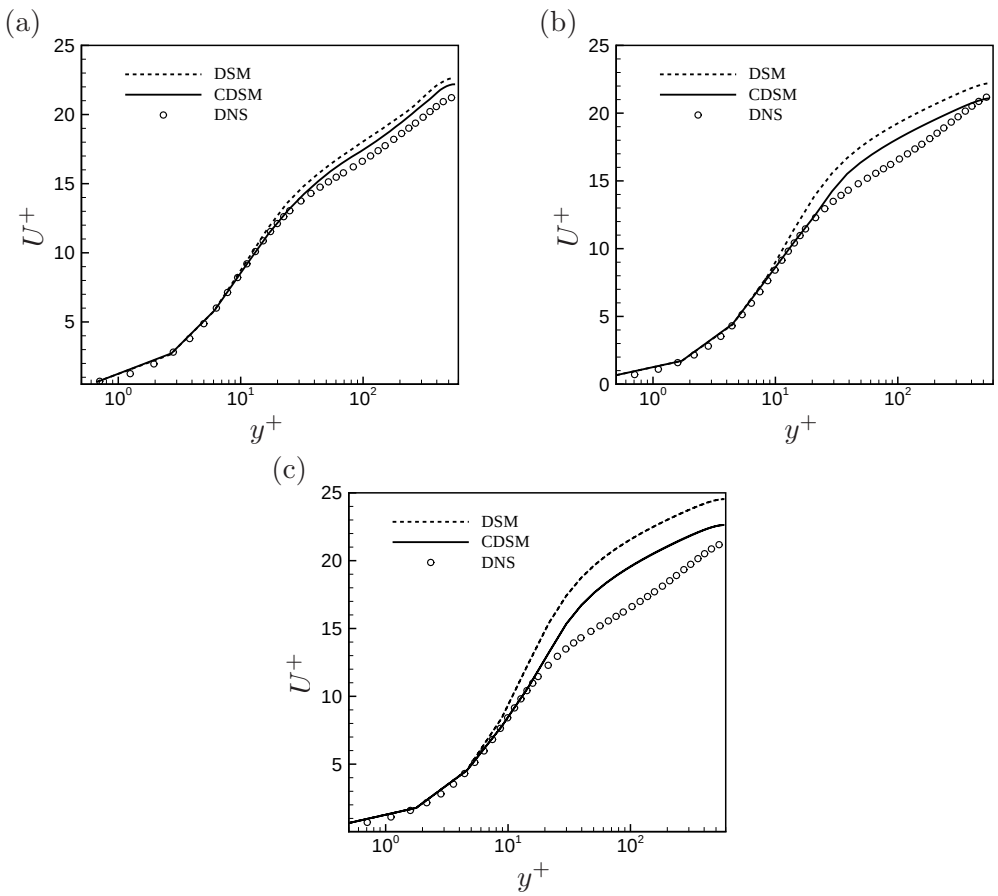

Figure 5.10: Mean velocity from turbulent channel flow at $Re_\tau = 590$ (case 590spec) using different numerical methods: (a) pseudo-spectral, (b) finite-difference, (c) unstructured finite-volume.

Reynolds shear stress is closer to the imposed constraint in the small region around $20 \leq y^+ \leq 40$ than at $C_\omega = 0.1$ (fig. 5.9(d)). The impact on the bulk flow is such that the mean streamwise velocity is slightly closer to the DNS with $C_\omega = 1.0$ (fig. 5.9(d)). Hence, CDSM is marginally sensitive to the choice of C_ω.

5.3.4 Effect of numerical method

As is true for any simulation methodology, an idea of what constitutes an adequate grid requirement for a reasonable solution is essential, particularly when the intention is to simulate high Reynolds number flows in complex geometries. Apart from the base SGS model, the inherent accuracy of the numerical method plays a major role in the accuracy

of results obtained from CDSM on coarse grids. Fig. 5.10 shows mean velocity profiles from using three numerical methods : Chebychev pseudo-spectral, structured finite-difference (briefly described in appendix B), and unstructured finite-volume method (sec. 2.4). These results are obtained for case 590spec which has a very coarse near-wall Δz^+ and Δx^+. The Chebychev pseudo-spectral solver produces reasonable results. The log-layer and the outer region are not predicted as accurately by spatially second-order central difference schemes on such a coarse grid. However, CDSM consistently predicts better results than DSM and relatively relaxes the near-wall grid requirement for accurate C_f prediction over DSM.

5.4 Implications as a wall model

The goal of wall modeling is to relax the near-wall grid scaling with Reynolds number. DES achieves this by operating on a RANS near-wall grid where the wall-parallel spacing is large compared to the boundary-layer thickness ($\Delta_{\parallel} \gg \delta$) but the wall-normal grid spacing requirement is stricter ($\Delta^+_{\perp,w} \leq 1$). Nikitin et al. [65] followed this guideline for their DES of channel flow and showed results with $\Delta_{\parallel} = 0.1\delta$ and $\Delta y^+_w < 1$. Further savings could be obtained by relaxing the wall-normal grid spacing requirement. When the first off-wall grid point is in the log layer, the filter width is much larger than the local turbulent integral scales. Hence, wall stress models are required to compensate for the SGS modeling errors in this region. Nicoud et al. [79], Templeton et al. [78] and various other researchers use walls stress models on coarse grids. Chung and Pullin [80] propose a stretched-vortex SGS model to compute an instantaneous slip velocity at a 'virtual wall' which scales with δ.

Throughout this dissertation, LES is performed using no-slip boundary conditions at the wall with a slightly relaxed near-wall grid requirement. Results have been shown with wall parallel coarsening ($\Delta x \geq 0.04\delta$, $\Delta z > 0.02\delta$) and reasonable wall-normal resolution ($\Delta y^+ \sim 4$). For instance, fig. 5.9(e) in sec. 5.3.3 showed that CDSM predicts the mean velocity for $Re_\tau = 2000$ at such a coarse resolution where DSM is just not expected to perform well. Fig. 5.11 shows that CDSM is able to reasonably predict the mean velocity even when $\Delta z^+_w > 200$ at $Re_\tau = 10000$. The reference lines are plotted to allow comparison to the high Re DES of Nikitin et al. [65] and LES of Chung and

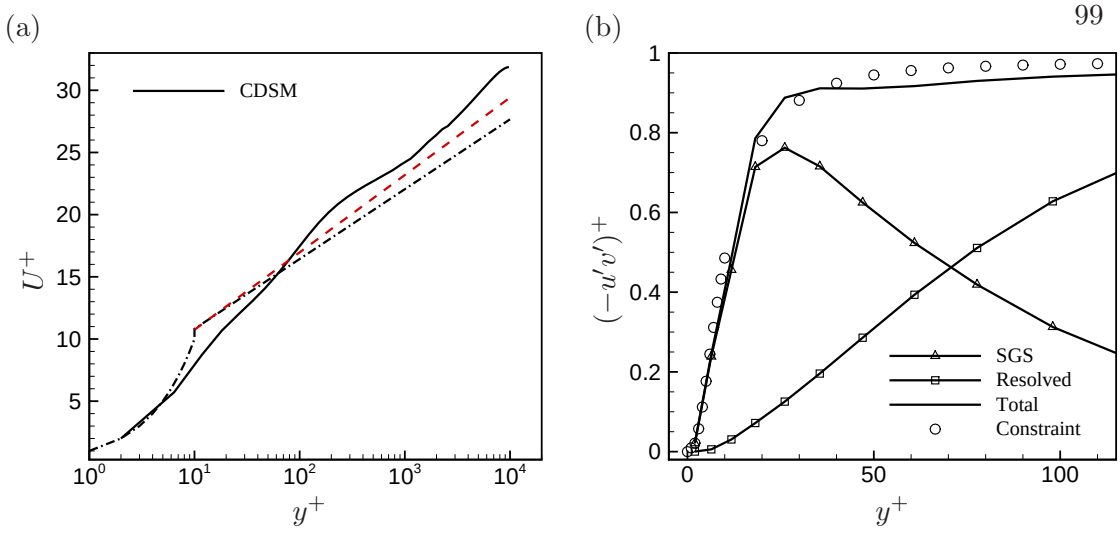

Figure 5.11: Mean statistics from turbulent channel flow at $Re_\tau = 10^3$ - Case 10kun: (a) mean velocity; ---- : $log(y^+/11)/0.37 + 11$ (Ref. [80]); —·— : $y^+, log(y^+)/0.41 + 5.2$ (Ref. [65]), (b) Reynolds stress.

Pullin [80]. Clearly, at such coarse resolution, the Reynolds shear stress is not expected to be resolved; the CDSM constraint compensates by increasing the modeled SGS stress near the wall. Note that using a more accurate numerical method such as a pseudo-spectral method would predict better results than what have been shown here using an unstructured finite-volume solver (shown in section 5.3.4).

Recall that the target Reynolds stress could be sourced from RANS, DNS, experiments or empirical closures/fits. For instance, case 590spec uses Reynolds stress from a RANS model (briefly described in appendix B), and cases 590s, 590un and 1kun use Reynolds stress from DNS. At high Reynolds numbers and complex flows, the target Reynolds stress may not be available *a priori*. A more convenient alternative may be models for Reynolds stress. Such models need only be reasonably accurate in the near-wall region as the constraint is only intended to be applied there. Cases 2kun and 10kun use Reynolds stress obtained using the model described by Perry et al. [81] and made available as an online tool [82]. Fig. 5.9(c)-(d) show that the constraint is in good agreement with DNS near the wall and this is also found to be true for other available DNS data (not shown here). Fig. 5.12 shows that the weight function $\omega^{\mathcal{R}}$ is significant only at some grid points near the wall upto $y \leq 0.07\delta$; this region gets smaller with increasing Re. Hence the Reynolds stress constraint is only active at these points,

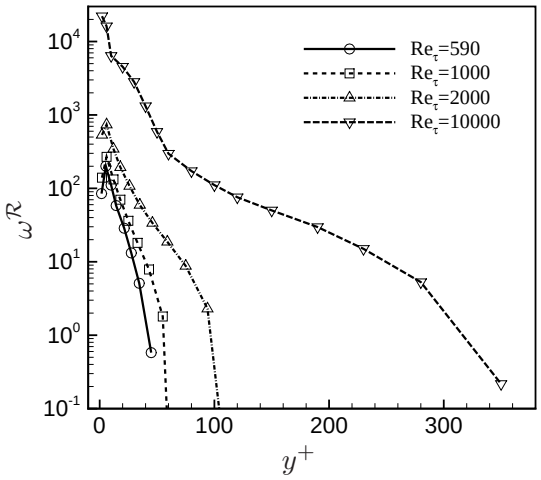

Figure 5.12: Comparison of weight function $\omega^{\mathcal{R}}$ from cases 590un, 1kun, 2kun, and 10kun using $C_\omega = 0.1$.

implying that the target Reynolds stress need only be accurate in this region near the wall.

The proposed procedure to impose a constraint is general (eq. 5.2) and can in principle, be extended to incorporate constraints other than Reynolds stress. In general, the constraint $\epsilon_{ij}^{\mathcal{C}}$ would need to be expressed as a function of the model coefficient C_s and then the minimization can be carried out either analytically or numerically. For instance, a desired and relatively easily available constraint is the skin friction C_f or wall shear stress τ_w. Then, the velocity U would need to be expressed as an implicit function of C_s and the minimization of $\epsilon_{ij}^{\mathcal{C}}(U(C_s))$ may be carried out in a predictor-corrector manner. In fact, such a predictor-corrector approach has been used by Park and Mahesh [10] in their control-based SGS model. However such 'implicit dependence' models would not lend themselves to an algebraic expression for C_s such as eq. 5.12. Wikström et al. [83] and Fureby et al. [84] use a model for the wall eddy viscosity ν_{bc}:

$$\nu + \nu_{bc} = \tau_w/(du/dy)_w,$$

where u is given by the law of the wall. Instead of imposing a steady condition like the

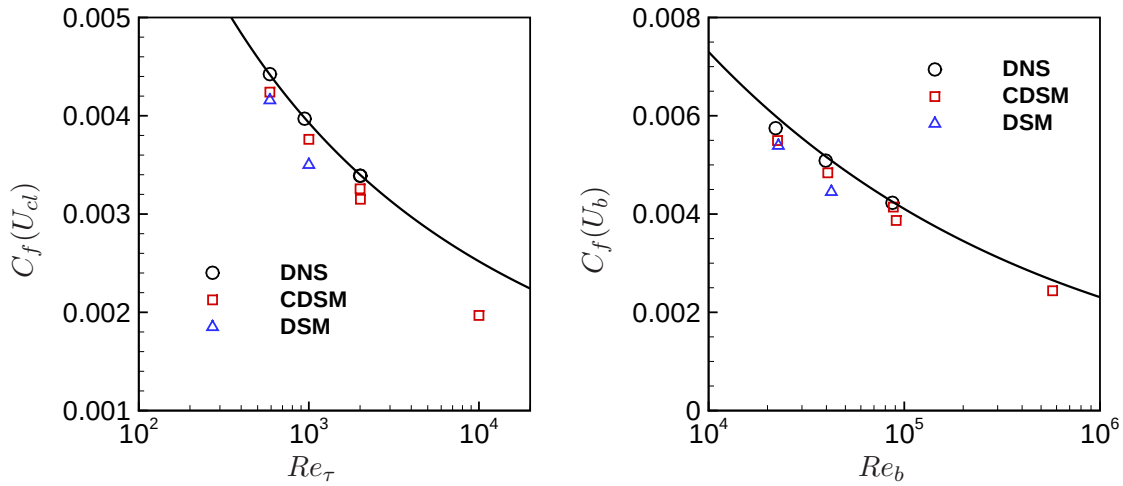

Figure 5.13: Skin-friction coefficient C_f from cases 590un, 1kun, 2kun and 10kun in terms of (a) centerline velocity U_{cl} and Re_τ, —— : extrapolated from the DNS of Moser et al. [40] by assuming $U_{cl}^+ = 21.26 + log(Re_\tau/587)/0.41$ (following ref. [65]), (b) bulk velocity U_b and $Re_b = 2U_b\delta/\nu$, —— : Dean's correlation $C_f = 0.073Re_b^{-1/4}$ [85].

law of the wall, this expression for the wall shear stress can be imposed in the mean as:

$$\langle(\nu + 2C_{s,bc}|S|)\ S_{ij}\rangle_t = \langle\tau_{ij,w}\rangle_t.$$

Analogous to eq. 5.5, the constraint can be now be formulated as the error:

$$\begin{aligned} \epsilon ij^{\mathcal{R}} &= \langle\tau_{ij}\rangle_t - \langle\nu S_{ij}\rangle_t - \langle C_s|S|S_{ij}\rangle_t \\ &\approx A_{ij} - B_{ij}C_s. \end{aligned}$$

Finally, skin-friction coefficient $C_f = \tau_w/(\frac{1}{2}U^2)$ and wall pressure fluctuations $\sigma(p)/\tau_w$ are plotted in figs. 5.13 and 5.14 respectively. C_f in fig. 5.13(a) is based on the centerline velocity U_{cl} and plotted against Re_τ whereas in fig. 5.13(b), it is based on the bulk velocity U_b and bulk Reynolds number $Re_b = 2U_b\delta/\nu$. CDSM is in reasonable agreement with DNS data and empirical fits and it is always better than DSM. Only when the grid is very coarse (case 10kun), CDSM tends to recede from the empirical fits. Fig. 5.14 shows that wall pressure fluctuations from CDSM are in good agreement with DNS and the empirical fit at $Re_\tau = 590$ and 1000. However as the grid coarsens and resolved stress decreases, CDSM predicts decreased resolved $\sigma(p)/\tau_w$ as is expected.

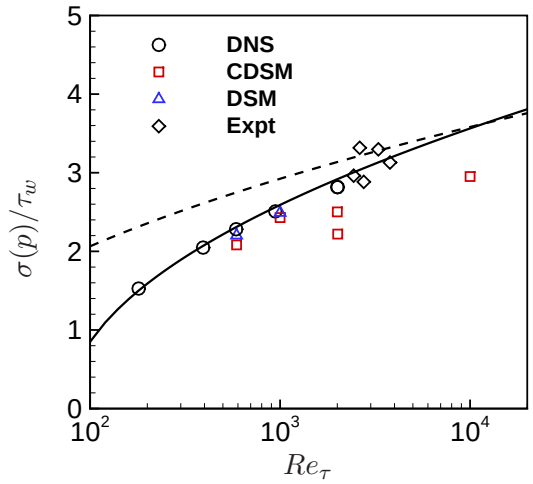

Figure 5.14: Wall pressure fluctuations $\sigma(p)/\tau_w$ from cases 590un, 1kun, 2kun and 10kun. ---- : $(6.5 + 1.86\ log(y^+/333))^{1/2}$ (Ref. [86]); —— : $(2.60\ log(Re_\tau) - 11.25)^{1/2}$ (Ref. [87]); $\diamond$: experiment of Bull and Thomas [88].

Thus, CDSM is a reliable model to perform LES all the way to the wall, better predict skin friction over DSM and also predicts rms wall pressure fluctuations reasonably well.

5.5 Summary

DES is a widely used methodology for high Reynolds number external aerodynamics [89]. LES has been used successfully for high Reynolds number separated flows such as in gas turbine combustors [3] and predicting unsteady forces on marine propellers [90]. The strong scaling of the computing cost of LES with Reynolds number is a challenge to LES being applied to attached wall-bounded flows of engineering interest. However LES for wall-bounded flows offers the advantage of computing fluctuating quantities on the wall such as wall pressure fluctuations and sound [91].

Nicoud et al. [79] note that DES is a suboptimal SGS model because the underlying model is calibrated in the RANS mode. An ideal zonal RANS/LES simulation shows that the zonal interface problem comes from excessive dissipation in the RANS region. The proposed model approaches the mean modeled behavior of RANS through a constraint on what is essentially an SGS model. Primarily, it allows hybridization of the LES methodology with a desired or expected mean target quantity. Currently,

external Reynolds stress constraints are incorporated into the Dynamic Smagorinsky model. Secondly, this target quantity may be imposed in a small region near the wall for wall-bounded flows where SGS modeling errors are expected to be large. Normalized Germano-identity error is used as a measure of SGS modeling errors and hence as a weight for the constraint.

LES is performed for turbulent channel flows at various Reynolds numbers and grid resolutions. CDSM outperforms DSM and this improvement is more apparent as the near-wall grid coarsens. CDSM achieves better predictions than DSM by constraining the total Reynolds stress to an *a priori* imposed target. It has been shown that this target Reynolds stress can be obtained from RANS, DNS and near-wall models. The model is shown to be marginally sensitive to the scaling coefficient C_ω upto an order of magnitude. Threshold $\mathcal{E}_t$ must be judiciously chosen such that the constraint is imposed only in the near-wall region. Imposition of the near-wall Reynolds stress constraint raises the eddy viscosity and reduces the Germano-identity error.

In principle, this procedure of constrained minimization can be extended to incorporate any generalized constraint. Instead of Reynolds stress, the constraint could be skin friction or other quantities which might be known *a priori* at or near the wall. Finally, this procedure does not force the instantaneous flow to a mean quantity but only constrains the mean behavior. Hence CDSM predicts unsteady behavior down to the wall and is a reliable tool to predict quantities of engineering interest such as skin friction and wall pressure fluctuations. For future work, CDSM will be applied to complex geometries and separated flows.

Bibliography

[1] M. Germano, U. Piomelli, P. Moin, and W. H. Cabot. A dynamic subgrid-scale eddy viscosity model. *Physics of Fluids A*, 3:7:1760, 1991.

[2] D. K. Lilly. A proposed modification of the germano subgrid–scale closure model. *Physics of Fluids A*, 4:3:633, 1992.

[3] K. Mahesh, G. Constantinescu, and P. Moin. A numerical method for large–eddy simulation in complex geometries. *Journal of Computational Physics*, 197:1:215, 2004.

[4] M. Vyšohlid and K. Mahesh. Large eddy simulation of propeller crashback. In *Proceedings of Flow Induced Unsteady Loads and the Impact on Military Applications, RTO-MP-AVT-123, Neuilly-sur-Seine, France*, 2005.

[5] M. Vyšohlid and K. Mahesh. Large eddy simulation of crashback in marine propellers. In *Proceedings of the 26^{th} Symposium on Naval Hydrodynamics, Rome, Italy*, 2006.

[6] P. Chang, M. Ebert, Y. L. Young, Z. Liu, K. Mahesh, H. Jang, and M. Shearer. Propeller forces and structural responses to crashback. In *Proceedings of the 27^{th} Symposium on Naval Hydrodynamics, Seoul, Korea*, 2008.

[7] H. Jang and K. Mahesh. Large eddy simulation of marine propellers in crashback. In *Proceedings of the 28^{th} Symposium on Naval Hydrodynamics, Pasadena, CA*, 2010.

[8] H. Jang and K. Mahesh. Large eddy simulation of flow around a reverse rotating propeller. In review, *Journal of Fluid Mechanics*, 2012.

[9] D. H. Bridges. A detailed study of the flowfield of a submarine propeller during a crashback maneuver. Technical Report MSSU-ASE-04-1, Department of Aerospace Engineering, Mississippi State University, 2004.

[10] N. Park and K. Mahesh. Reduction of the germano identity error in the dynamic subgrid model. *Physics of Fluids*, 21:065106, 2009.

[11] C. Meneveau, T. S. Lund, and W. H. Cabot. A lagrangian dynamic subgrid-scale model of turbulence. *J. Fluid Mech.*, 319:353, 1996.

[12] N. Groves, T. Huang, and M. Chang. Geometric characteristics of DARPA SUBOFF models (DTRC Model Nos. 5470 and 5471). Technical Report DTRC/SHD-1298-01, Ship Hydromechanics Dept., David Taylor Research Center, Bethesda, MD, March 1989.

[13] X. Liu and J. Katz. Cavitation phenomena occurring due to interaction of shear layer vortices with the trailing corner of a two-dimensional open cavity. *Physics of Fluids*, 20:041702, 2008.

[14] S. Ghosal and P. Moin. The basic equations for the large eddy simulation of turbulent flows in complex geometry. *J. Computational Physics*, 118:24–37, 1995.

[15] J. Gullbrand. Grid-independent large-eddy simulation in turbulent channel flow using three-dimensional explicit filtering. *Annual Research Briefs, Center for Turbulence Research, Stanford Univ.*, 2002.

[16] J. Smagorinsky. General circulation experiments with the primitive equations: I. The basic experiment. *Mon. Weath. Rev.*, 91:99, 1963.

[17] F. H. Harlow and J. E. Welch. Numerical calculation of time-dependent viscous incompressible flow of fluid with free-stream. *Phys. Fluids*, 8:2182–2189, 1965.

[18] URL https://computation.llnl.gov/casc/hypre/software.html.

[19] H. Jang. *Large eddy simulation of Crashback in marine propulsors*. PhD thesis, University of Minnesota, 2011.

[20] R. B. Green, E. A. Gillies, and R. E. Brown. The flow field around a rotor in axial descent. *Journal of Fluid Mechanics*, 534:237–261, 2005.

[21] C. W. Jiang, R. R. Dong, H. L. Lui, and M. S. Chang. 24–inch water tunnel flow field measurements during propeller crashback. In *Proceedings of the 21st Symposium on Naval Hydrodynamics*. The National Academies Press, Washington DC, 1997.

[22] S. Jessup, C. Chesnakas, D. Fry, M. Donnelly, S. Black, and J. Park. Propeller performance at extreme off design conditions. In *Proceedings of the 25th Symposium on Naval Hydrodynamics, St. John's, Canada*, 2004.

[23] F. Davoudzadeh, L. K. Taylor, W. C. Zierke, J. J. Dreyer, H. McDonald, and D. L. Whitfield. Coupled Navier–Stokes and equations of motion simulation of submarine maneuvers, including crashback. In *Proceedings of the 1997 ASME Fluids Engineering Division Summer Meeting, New York*, 1997.

[24] B. Chen and F. Stern. Computational fluid dynamics of four quadrant marine propeller flow. *Journal of Ship Research*, 43:4:218, 1999.

[25] S. Jessup, D. Fry, and M. Donnelly. Unsteady propeller performance in crashback conditions with and without duct. In *Proceedings of the 26th Symposium on Naval Hydrodynamics, Rome, Italy*, 2006.

[26] D. H. Bridges, M. J. Donnelly, and T. J. Park. Experimental investigation of the submarine crashback maneuver. *Journal of Fluids Engineering*, 130, 2008.

[27] H. Le, P. Moin, and J. Kim. Direct numerical simulation of turbulent flow over a backward–facing step. *Journal of Fluid Mechanics*, 330:349–374, 1997.

[28] R. A. Antonia. Conditional sampling in turbulence measurement. *Annual Review of Fluid Mechanics*, 13:131–156, 1981.

[29] T. S. Lund, S. Ghosal, and P. Moin. Numerical simulations with highly variable eddy viscosity models. *Engineering Applications of Large Eddy Simulations, ASME*, 162:7–11, 1993.

[30] S. Ghosal, T. S. Lund, P. Moin, and K. Akselvoll. A dynamic localization model for large-eddy simulation of turbulent flows. *J. Fluid Mech*, 286:229, 1995.

[31] C. Meneveau and T. S. Lund. On the lagrangian nature of the turbulence energy cascade. *Physics of Fluids*, 6:2820, 1994.

[32] J. I. Choi, K. Yeo, and C. Lee. Lagrangian statistics in turbulent channel flow. *Physics of Fluids*, 16:779, 2004.

[33] R. Anderson and C. Meneveau. Effects of the similarity model in finite-difference LES of isotropic turbulence using a lagrangian dynamic mixed model. *Flow, Turbulence and Combustion*, 62:3:201–225, 1999.

[34] F. Sarghini, U. Piomelli, and E. Balaras. Scale-similar models for large-eddy simulations. *Physics of Fluids*, 11:6:1596–1607, 1999.

[35] R. Stoll and F. Porté-Agel. Dynamic subgrid-scale models for momentum and scalar fluxes in large-eddy simulations of neutrally stratified atmospheric boundary layers over heterogeneous terrain. *Water Resources Research*, 42:W01409, 2006.

[36] D. You, M. Wang, and R. Mittal. A methodology for high performance computation of fully inhomogeneous turbulent flows. *Int. J. for Numerical Methods in Fluids*, 53:6:947–968, 2007.

[37] M. Inagaki, T. Kondoh, and Y. Nagano. A mixed-time-scale SGS model with fixed model-parameters for practical LES. *Engineering Turbulence Modeling and Experiments 5*, pages 257–266, 2002.

[38] O. V. Vasilyev, G. De Stefano, D. E. Goldstein, and N. K.-R. Kevlahan. Lagrangian dynamic SGS model for stochastic coherent adaptive large eddy simulation. *Journal of Turbulence*, 9, 2008.

[39] A. L. Rovelstad, R. A. Handler, and P. S. Bernard. The effect of interpolation errors on the lagrangian analysis of simulated turbulent channel flow. *Journal of Computational Physics*, 110:1:190–195, 1994.

[40] R. D. Moser, J. Kim, and N. N. Mansour. Direct numerical simulation of turbulent channel flow up to $Re_\tau = 590$. *Physics of Fluids*, 11:943, 1999.

[41] J. C. del Alamo, J. Jimenez, P. Zandonade, and Robert D. Moser. Scaling of the energy spectra of turbulent channels. *J. Fluid Mech.*, 500:135–144, 2004.

[42] S. Hoyas and J. Jimenez. Scaling of the velocity fluctuations in turbulent channel flow up to $Re_\tau = 2003$. *Physics of Fluids*, 18:011702, 2006.

[43] R. Stoll and F. Porté-Agel. Large-eddy simulation of the stable atmospheric boundary layer using dynamic models with different averaging schemes. *Boundary-Layer Meteorology*, 126:1–28, 2008.

[44] A. G. Kravchenko, P. Moin, and K. Shariff. B-spline method and zonal grids for simulations of complex turbulent flows. *Journal of Computational Physics*, 151:2: 757–789, 1999.

[45] R. Mittal and S. Balachandar. On the inclusion of three dimensional effects in simulations of two-dimensional bluff body wake flows. In *Proceedings of the ASME Fluids Engg. Div. Summer Meeting, Vancouver, Canada*, 1997.

[46] P. Babu and K. Mahesh. Aerodynamic loads on cactus-shaped cylinders at low reynolds numbers. *Physics of Fluids*, 20035112, 2008.

[47] C. H. K. Williamson. Vortex dynamics in the cylinder wake. *Annu. Rev. Fluid Mech.*, 28:477, 1996.

[48] A. G. Kravchenko and P. Moin. Numerical studies over a circular cylinder at $Re_D = 3900$. *Physics of Fluids*, 12:2:403–417, 2000.

[49] J. Franke and W. Frank. Large eddy simulation of the flow past a circular cylinder at $Re = 3900$. *J. Wind. Eng. Ind. Aerodyn.*, 90:1191, 2002.

[50] L. Ong and J. Wallace. The velocity field of the turbulent very near wake of a circular cylinder. *Experiments in Fluids*, 20:441–453, 1996.

[51] J. C. R. Hunt, A. Wray, and P. Moin. Eddies, stream, and convergence zones in turbulent flows. Technical report, Center for Turbulence Research Report, Stanford Univ., 1988.

[52] J. Wu C. H. K. Williamson and J. Sheridan. Scaling of streamwise vortices in wakes. *Physics of Fluids*, 7:2307, 1995.

[53] A. Verma, H. Jang, and K. Mahesh. Large eddy simulation of the effect of hull on marine propulsors in crashback. In *Proceedings of the 2nd International Symposium on Marine Propulsors, Hamburg, Germany*, 2011.

[54] U. Piomelli, Y. Yu, and R. J. Adrian. Subgrid-scale energy transfer and near-wall turbulence structure. *Physics of Fluids*, 8:1978, 1996.

[55] J. A. Templeton, M. Wang, and P. Moin. An efficient wall model for large-eddy simulation based on optimal control theory. *Physics of Fluids*, 18:025101, 2006.

[56] N. Park and K. Mahesh. A velocity-estimation subgrid model constrained by subgrid scale dissipation. *J. Comput. Phys.*, 227:4190, 2008.

[57] J. S. Baggett, J. Jiménez, and A. G. Kravchenko. Resolution requirements in large-eddy simulations of shear flows. *Annual Research Briefs, Center for Turbulence Research, Stanford Univ.*, 1997.

[58] U. Piomelli and E. Balaras. Wall-layer models for large-eddy simulations. *Annual Review Fluid Mechanics*, 34:349–74, 2002.

[59] U. Piomelli. Wall-layer models for large-eddy simulations. *Progress in Aerospace Sciences*, 44:437–446, 2008.

[60] U. Schumann. Subgrid-scale model for finite difference simulation of turbulent flows in plane channels and annuli. *J. Comput. Phys.*, 18:376, 1975.

[61] C. G. Speziale. Turbulence modeling for time-dependent RANS and VLES: A review. *AIAA Journal*, 36:2, 1998.

[62] P. Batten, U. Goldberg, and S. Chakravarthy. Interfacing statistical turbulence closures with large-eddy simulation. *AIAA Journal*, 42:3, 2004.

[63] S.S. Girimaji. Partially-averaged navier-stokes model for turbulence: a reynolds-averaged navier-stokes to direct numerical simulation bridging method. *J. Appl. Mech.-Trans. ASME*, page 73, 2006.

[64] P.R. Spalart, W.H. Jou, M. Strelets, and S.R. Allmaras. Comments on the feasibility of LES for wings and on a hybrid RANS/LES approach. In *First AFOSR International Conference on DNS/LES, Ruston, Louisiana*. Greyden Press, 1997.

[65] N.V. Nikitin, F. Nicoud, B. Wasistho, K.D. Squires, and P.R. Spalart. An approach to wall modeling in large-eddy simulations. *Physics of Fluids*, 12:1629, 2000.

[66] F.R. Menter and M. Kuntz. Adaptation of eddy-viscosity turbulence models to unsteady separated flow behind vehicles. In *The Aerodynamics of Heavy vehicles: Trucks, Buses, and Trains, editors: R. McCallen, F. Browan and J. Ross*, pages 339–52. Springer, New York, 2004.

[67] P.R. Spalart, S. Deck, M.L. Shur, K.D. Squires, M. Strelets, and A. Travin. A new version of detached-eddy simulation, resistant to ambiguous grid densities. *Theor. Comp. Fluid Dyn.*, 20, 2006.

[68] A. Keating and U. Piomelli. A dynamic stochastic forcing method as a wall-layer model for large-eddy simulation. *J. Turbulence 7*, 12, 2006.

[69] M.L. Shur, P.R. Spalart, M. Strelets, and A. Travin. A hybrid RANS-LES approach with delayed-DES and wall-modeled LES capabilities. *Int. J. Heat Fluid Flow*, 29-6, 2008.

[70] J.U. Schlüter, X. Wu, S. Kim, S. Shankaran, J.J. Alonso, and H. Pitsch. A framework for coupling reynolds-averaged with large-eddy simulations for gas turbine applications. *J. Fluids Engg.*, 127-4:806, 2005.

[71] J.U. Schlüter, H. Pitsch, and P. Moin. Large eddy simulation inflow conditions for coupling with reynolds-averaged flow solvers. *AIAA Journal*, 42-3:478–484, 2004.

[72] J. S. Baggett. On the feasibility of merging LES with RANS for the near-wall region of attached turbulent flows. *Annual Research Briefs, Center for Turbulence Research, Stanford Univ.*, 1998.

[73] Y. Shi, Z. Xiao, and S. Chen. Constrained subgrid-scale stress model for large eddy simulation. *Physics of Fluids*, 20:011701, 2008.

[74] N. Park and K. Mahesh. A dynamic wall model constrained by external reynolds stress. In *Proceedings of XXII ICTAM, Adelaide, Australia*, 2008.

[75] S. Chen, Z. Xia, S. Pei, J. Wang, Y. Yang, Z. Xiao, and Y. Shi. Reynolds-stress-constrained large-eddy simulation of wall-bounded turbulent flows. *J. Fluid Mech.*, 703:1–28, 2012.

[76] C. Meneveau and J. Katz. Dynamic testing of subgrid models in large eddy simulation based on germano identity. *Physics of Fluids*, 11:245–247, 1999.

[77] P. Sagaut. *Large Eddy Simulation for Incompressible Flows*. Springer, Berlin, 2002.

[78] J. A. Templeton, G. Medic, and G. Kalizin. An eddy-viscosity based near-wall treatment for coarse grid large-eddy simulation. *Physics of Fluids*, 17:105101, 2005.

[79] F. Nicoud, J. S. Baggett, P. Moin, and W. Cabot. Large eddy simulation wall-modeling based on suboptimal control theory and linear stochastic estimation. *Physics of Fluids*, 13:2970, 2001.

[80] D. Chung and D. I. Pullin. Large-eddy simulation and wall modelling of turbulent channel flow. *J. Fluid Mech.*, 631:281–309, 2009.

[81] A. E. Perry, I. Marusic, and M. B. Jones. On the streamwise evolution of turbulent boundary layers in arbitrary pressure gradients. *J. Fluid Mech.*, 461:61–91, 2002.

[82] URL http://www.aem.umn.edu/~marusic/UUfit/Marusic_class_files/u1u3/Fourthcomp.htm.

[83] N. Wikström, U. Svennberg, N. Alin, and C. Fureby. Large eddy simulation of the flow around an inclined prolate spheroid. *Journal of Turbulence*, 5:N29, 2004.

[84] C. Fureby, N. Alin, N. Wikström, and U. Svennberg. Large-eddy simulation of high-reynolds-number wall-bounded flows. *AIAA Journal*, 42:3, 2004.

[85] R. B. Dean. Reynolds number dependence of skin friction and other bulk flow variables in two-dimensional rectangular duct flow. *Trans. ASME: J. Fluids Engg.*, 100:215–223, 1978.

[86] T. M. Farabee and M. J. Casarella. Spectral features of wallwall presure fluctuations beneath turbulent boundary layers. *Physics of Fluids A*, 3:10:2410–2420, 1991.

[87] Z. W. Hu, C. L. Morfey, and N. D. Sandham. Wall pressure and shear stress spectra from direct simulations of channel flow. *AIAA Journal*, 44:7:1541–1549, 2006.

[88] M. K. Bull and A. S. W. Thomas. High frequency wall presure fluctuations in turbulent boundary layers. *Physics of Fluids*, 19:579–599, 1976.

[89] P.R. Spalart. Detached-eddy simulation. *Annu. Rev. Fluid Mech.*, 41:181–202, 2009.

[90] A. Verma, H. Jang, and K. Mahesh. The effect of upstream hull on a propeller in reverse rotation. 2012. Journal of Fluid Mechanics.

[91] M. Wang and P. Moin. Dynamic wall modeling for large-eddy simulation of complex turbulent flows. *Physics of Fluids*, 14:7, 2002.

[92] R. E. A. Arndt. Cavitation in vortical flows. *Annual Reviews Fluid Mech.*, 34: 143, 2002.

[93] C. E. Brennen. *Cavitation and bubble dynamics*. Oxford Univ. Press, 1995.

[94] D. Rockwell and E. Naudascher. Self-sustained oscillations of impinging free shear layers. *Annual Reviews Fluid Mech.*, 11:67–94, 1979.

[95] T. S. Lund, X. Wu, and K. D. Squires. Generation of turbulent inflow data for spatially-developing boundary layer simulations. *J. Comp. Phys.*, 140:233–258, 1998.

[96] P. Babu. *Simulation and modeling of three turbulent flow problems*. PhD thesis, University of Minnesota, 2007.

[97] M. Mattson and K. Mahesh. Simulation of bubble migration in a turbulent boundary layer. *Physics of Fluids*, 23:045107, 2011.

[98] D. Rockwell and C. Knisely. Observation of the three-dimensional nature of unstable flow past a cavity. *Physics of Fluids*, 23:425–431, 1980.

[99] J.-C. Lin and D. Rockwell. Organized oscillations of initially turbulent flow past a cavity. *AIAA Journal*, 39:6:1139–1151, 2001.

[100] S. Cerutti, O. M. Knio, and J. Katz. Numerical study of cavitation inception in the near field of an axisymmetric jet at high Reynolds number. *Phys. of Fluids*, 12(10):2444–2460, 2000.

[101] J. Kim, P. Moin, and R. D. Moser. Turbulence statistics in fully developed channel flow at low reynolds number. *J. Fluid Mech.*, 177:133, 1987.

[102] J. A. Ekaterinaris. Implicit, high–resolution, compact schemes for gas dynamics and aeroacoustics. *J. Comput. Phys.*, 156:272, 1999.

[103] Y. Morinishi, T. S. Lund, O. V. Vasilyev, and P. Moin. Fully conservative higher order finite difference schemes for incompressible flow. *J. Comput. Phys.*, 143: 90–124, 1998.

[104] A. A. Wray. Minimal storage time advancement schemes for spectral methods. 1990.

[105] J. K. Dukowicz and A. S. Dvinsky. Approximation as a high order splitting for the implicit incompressible flow equations. *J. Comput. Phys.*, 102:336, 1992.

[106] P. R. Spalart and S. R. Allmaras. A one-equation turbulence model for aerodynamic flows. *La recherche Aérospatiale*, 1:5, 1994.

Appendix A

Cavitation in Turbulent Flow past a Cavity

A.1 Introduction

Cavitation is a widely studied problem owing to their impact on acoustic emission, undesired structural loading and erosion [92]. Gas nuclei reside in most fluids and are believed to be a mechanism for cavitation inception [93]. When these small nuclei reach a region of very low pressure, their volume grows rapidly and macroscopic pockets of vapor are formed in the flow. This formation of macroscopic vapor pockets from the unstable rapid growth of the gas nuclei (and subsequent violent collapse) is the definition of cavitation inception. Cavitation adversely affects the performance of marine propellers, increases noise and erodes the propellers leading to structural failure. The phenomenon of cavitation is also used in medical devices to clean surfaces and remove kidney stones.

Predicting when and where cavitation inception occurs is very difficult and depends on many factors such as cavitation number σ_v and density of gas nuclei in the flow, among other factors [93]. The cavitation number σ_v is defined as

$$\sigma_v = \frac{P_\infty - P_\mathrm{v}}{\frac{1}{2}\rho_\infty U_\infty^2}, \tag{A.1}$$

where P_∞ is the far-field (ambient) fluid pressure, P_v is the far-field vapor pressure of

the carrier fluid, ρ_∞ is the fluid density at far-field and U_∞ is usually taken as the free-stream velocity. Assuming that the onset of cavitation occurs when the local pressure $P(\vec{x}, t)$ drops below the vapor pressure P_v, a critical coefficient of pressure can be defined as

$$C_{p,min} = \frac{P_\mathrm{v} - P_\infty}{\frac{1}{2}\rho_\infty U_\infty^2} = -\sigma_i, \tag{A.2}$$

where σ_i is the cavitation inception index. It is defined as the cavitation number when cavitation inception is first observed as the tunnel pressure is slowly lowered (lowering P_∞). In general, the lower the cavitation number the more likely cavitation is to occur, and once it occurs lowering the cavitation number increases the occurrence and persistence of vapor pockets.

Flow past an open cavity is an old canonical problem, both for experimentalists and practitioners of computational fluid dynamics. Incoming flow separates at the leading edge of the cavity and a shear layer is formed. Vortices are shed from the leading edge, travel downstream with the flow and impinge on the trailing edge of the cavity. This perturbation propagates upstream feeding back into the inducement of further vortical disturbance at the leading edge, resulting in a self-sustaining mechanism. Such self-sustaining oscillations are observed in a wide variety of engineering configurations such as landing gear wells, aircraft bomb bays, sunroof in cars and are a source of broadband noise and structural vibration [94].

Liu and Katz [13] measured the pressure field in a turbulent shear flow past an open cavity and observed unexpected cavitation phenomena. When the cavitation index σ_v is reduced, cavitation is observed in the flow, first at the expansion corner at the trailing edge, then in the vortices shed from the leading edge when σ_v is further decreased. When a shear layer vortex nears the trailing edge, the downwash creates a high pressure region and the cavitating bubbles located near the trailing edge collapse.

The cavitating bubbles respond to the pressure fluctuations by rapidly changing their volume. Predicting cavitation inception and modeling the unsteady evolution of bubbles in turbulent flows of engineering interest is a challenging problem. Large Eddy Simulation (LES) is performed to study cavitation inception in turbulent shear flow past an open cavity. The single phase LES is validated against the experiments in sec. A.5.1. Next, bubbles are introduced into the flow and results are discussed in sec. A.5.2. This

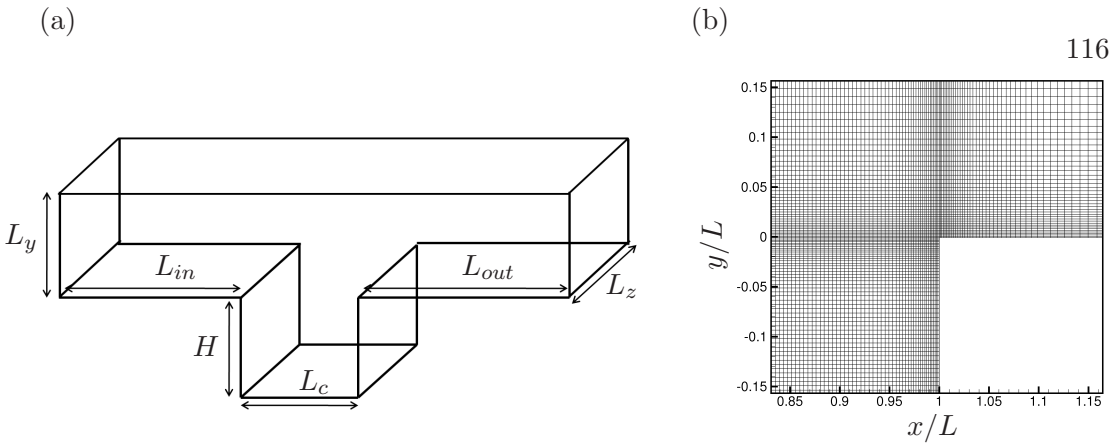

Figure A.1: (a) Domain of the simulation; (b) Computational grid near the cavity trailing edge.

work was performed together with Dr. Michael Mattson.

A.2 Problem definition

A.2.1 Experiment

The experiment by Liu and Katz [13] was performed in a small water tunnel, with a test section that consisted of a contraction ramp leading to the cavity, followed by a diffusing ramp. The leading edge is the edge of the cavity nearest to the inflow and the trailing edge is the cavity edge nearest the outflow. The cavity height $H = 30$ mm, length $L_c = 38.1$ mm and width $L_z = 50.8$ mm. The height of the water tunnel is 63.5 mm. Free stream velocity U_∞ is 5 m/s, with a Reynolds number based on the cavity length L and free-stream velocity U_∞ of $Re_L = 1.7 \times 10^5$. The Reynolds number based on the momentum thickness θ near the leading edge of the cavity is $Re_\theta = 1096$. Tripping grooves are used to ensure that the boundary layer separating at the leading cavity corner is turbulent.

A.2.2 Simulation

Computational domain and grid

Simulations are performed in a duct-like domain with a cavity. A schematic of the simulated geometry is shown in fig. A.1(a). A duct inflow section leads to a cavity,

(near wall)	$\Delta x_{min} = 0.050$, $\Delta y_{min} = 0.050$, $\Delta z_{min} = 0.150$, $\Delta y^+_{min} = 7$, $\Delta z^+_{min} = 21$
(outer region)	$\Delta x_{max} = 0.388$, $\Delta y_{max} = 0.479$, $\Delta z_{max} = 0.483$
(cavity)	$\Delta x_{max} = 0.161$, $\Delta y_{max} = 0.161$

Table A.1: Grid spacings. $^+$ denotes wall units, $y^+ = yu_\tau/\nu$.

followed by a duct outflow section. The reference length $L_{ref} = 1$ mm and the reference velocity $U_{ref} = 1$ mm/s. Henceforth, all dimensions are in terms of L_{ref} and U_{ref}. The inflow channel length $L_{in} = 70$ and the outflow length is $L_{out} = 91.9$. The height of the inflow and outflow section from bottom to the top wall $L_y = 33.5$. The cavity dimensions are kept the same as the experiment. The coordinate system origin is located at the leading edge of the cavity, in the symmetry plane between the spanwise walls. The grid used in the simulation has approximately 17 million control volumes with refinement at the leading and trailing edges of the cavity and walls of the domain. Grid near the cavity trailing edge is shown in fig. A.1(b) and the grid spacings are shown in table A.1.

Boundary conditions

All the channel walls (span-wise, top, bottom) and the cavity walls are treated with a no-slip boundary condition. A convective outflow boundary condition is applied at the outflow. Compared to the experimental setup, the contraction ramp upstream of the cavity with tripping grooves are not simulated in the current LES. It is assumed that the incoming flow separating at the cavity leading edge is a turbulent boundary layer. A separate LES of a spatially developing turbulent boundary layer is performed using the rescaling procedure of Lund et al. [95] on a $200 \times 95 \times 102$ grid at the same Re. The height and width of the channel for this separate boundary layer simulation is the same as the duct in the cavity simulation. A time series of velocity is extracted from an x-station of this equilibrium boundary layer. This velocity information is then supplied in a time-accurate fashion as the inflow boundary condition at the inflow plane of the cavity simulation. Table A.2 compares the boundary layer parameters obtained from this separate boundary layer LES at the extraction plane and those expected upstream of the cavity leading edge. Tables A.3 and A.4 compare the boundary layer parameters between the cavity LES and experiment just upstream of the cavity leading edge.

	δ_{99} (mm)	δ^* (mm)	θ (mm)	u_τ (m/s)
Inflow	1.467	0.2398	0.1417	0.168
$x = -12.5$ mm	2.231	0.315	0.210	0.180

Table A.2: Boundary layer parameters at the inflow plane (inflow boundary condition) and those obtained at a plane downstream (upstream of the cavity leading edge at $x = -12.5$ mm) from a separate turbulent boundary layer simulation.

	δ^*	θ	u_τ
LES	-	-	0.168
Experiment [13]	0.240	0.128	0.245

Table A.3: Boundary layer parameters further upstream of the cavity leading edge ($x = -12.5$ mm) from LES.

	δ_{99}	δ^*	θ	Re_θ	u_τ
LES	2.453	0.442	0.278	1210	0.168
Experiment [13]	1.8	0.325	0.210	1096	0.245

Table A.4: Comparison of boundary layer parameters just upstream of the cavity leading edge ($x = -1$ mm) from LES and experiment.

A.3 One-way coupled Euler-Lagrange method

In the one-way coupled Euler-Lagrangian framework, the bubbles are modeled as a dispersed phase combined with a continuous carrier (single) phase described by the Navier-Stokes equations. The single phase formulation is described in sec. 2.4. A point-particle, one-way coupled Euler-Lagrangian method is used to model the bubble convection and a hard-sphere model is used for bubble collisions. For simplicity, finite-size effects of the bubble on the surrounding flow are ignored. In this approach, the bubbles are modeled as a dispersed phase, with individual bubbles treated as point-particles governed by an equation for bubble motion, combined with a continuous carrier phase described by the Navier-Stokes equations. Hydrodynamic forces on bubbles that are larger than the grid spacing (as occasionally observed in the considered cases) are computed directly from the forces obtained from the bubble center; no attempt is made to correct for the finite size of the bubble.

Each bubble is tracked individually and characterized by its instantaneous position, velocity and size (bubble radius, assuming spherical bubbles). Bubble-wall interactions are treated as hard-sphere, inelastic collisions and bubble-bubble interactions are ignored. For a single spherical bubble in an infinite medium, the bubble response to pressure variation over time is given by the Rayleigh-Plesset (RP) equation:

$$\rho_{\mathrm{f}}\left[R\frac{d^2R}{dt^2}+\frac{3}{2}\left(\frac{dR}{dt}\right)^2\right]=p_B-p_\infty-\frac{2\sigma}{R}-\frac{4\mu_{\mathrm{f}}}{R}\frac{dR}{dt}, \tag{A.3}$$

where the relevant variables are the bubble radius $R(t)$, fluid dynamic viscosity μ_{f}, fluid density ρ_{f}, surface tension σ, far-field carrier fluid pressure P_∞ and bubble pressure p_B. Besides integrating the translation of a bubble, the radial variation must also be integrated. Since the behavior of a bubble can be extremely dynamic (e.g. bubble collapse), the Rayleigh-Plesset equation is integrated using an adaptive time-stepping, 4th-order accurate Runge-Kutta (RK) approach. The purpose of this adaptive control is to achieve accuracy to a predetermined limit while reducing computational overhead. In regions of large gradients small timesteps are prescribed, while in regions of low gradients larger timesteps are allowed to increase efficiency [96]. The details of this numerical method are given in Mattson and Mahesh [97].

A.4 Effect of boundary conditions

A.4.1 Convergent ramp inflow

As explained in sec. A.2.2, a turbulent boundary layer is supplied as an inflow condition in the LES. The boundary layer parameters show reasonable agreement with the experiment just upstream of the cavity leading edge. However, a discrepancy in the mean v-velocity in the inflow leading up to the cavity is observed between the experiment and LES. The experiment has a downward mean v-velocity in the inflow near the cavity as shown in fig. A.2(a). Whereas for the LES, the inflow near the cavity is akin to a turbulent boundary layer profile and hence doesn't have a downward mean v-velocity. The experimental set-up of Liu and Katz [13] consists of a convergent inflow section near the bottom wall. To investigate the effect of the convergent inflow section on the mean v-velocity, an LES with 26 million control volumes of the full-scale experimental

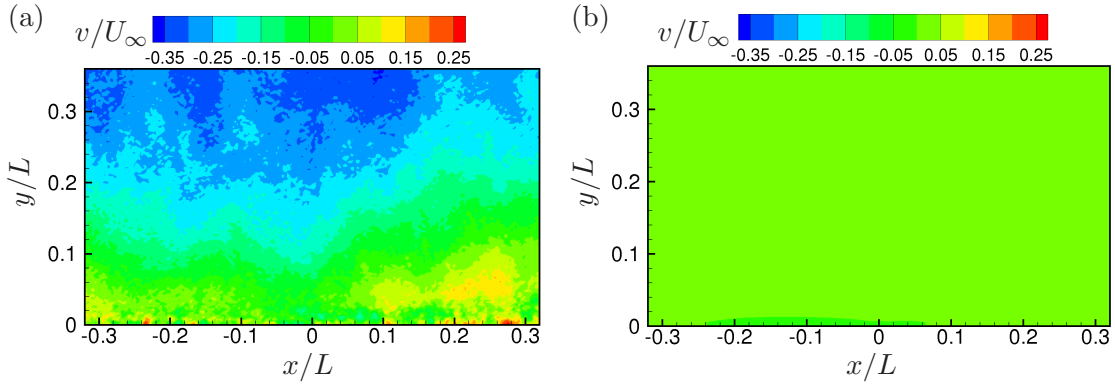

Figure A.2: Mean v velocity near cavity leading edge from (a) experiment [13] (b) convergent inflow section LES.

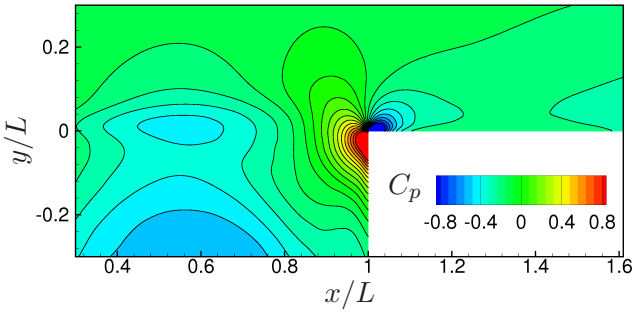

Figure A.3: Mean C_p velocity near cavity trailing edge from convergent inflow section LES.

set-up [see 13] was performed. Just as in the experiment, thirteen notches were used to trip the flow. Even the convergent inflow section LES does not show mean downward v-velocity (fig. A.2(b)). It must also be noted that the pressure inside the cavity in this case (fig. A.3) is found to be much lower than when using turbulent boundary layer inflow (fig. A.9(e)). It is conjectured that insufficient tripping in the simulation and/or noise in the experiment's water tunnel inflow is the reason for this discrepancy.

A.4.2 Spanwise periodicity

The boundary conditions (b.c.) for the spanwise direction play an important role in determining the pressure distribution in the cavity. Fig. A.4 shows the mean and rms pressure when periodic b.c. was used in the spanwise direction. Comparing fig. A.4(a) to A.9(e), the mean pressure in the core of the primary cavity vortex is seen to be lower

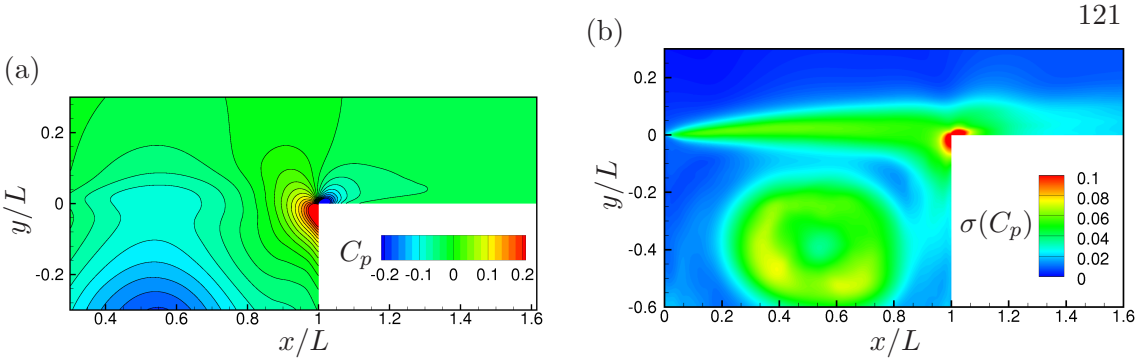

Figure A.4: Time averaged statistics from LES using periodic b.c. in the spanwise direction. (a) mean pressure C_p (b) rms pressure $\sigma(C_p)$.

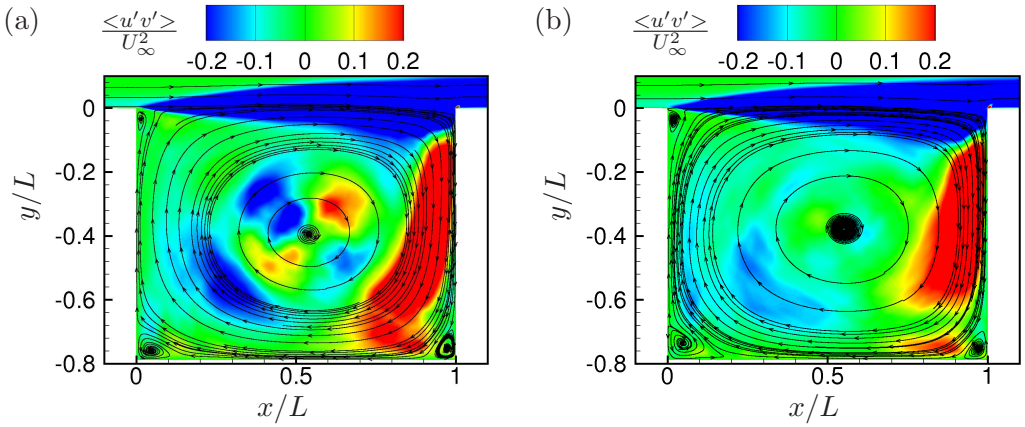

Figure A.5: Time averaged Reynolds-stress along with streamlines in the cavity from LES using (a) periodic b.c. (b) no-slip b.c. in the spanwise direction.

when periodic b.c. is used. Also, it can be seen that the rms pressure in the core of the cavity is higher in fig. A.4(b) than fig. A.10. Fig. A.5 shows higher velocity correlation along the near the bottom wall and in the center of the cavity. These regions correspond to the end of the jet-like flow along the vertical face of the trailing edge and the center of the primary vortex. This points towards the cavity flow being more correlated when periodic b.c. are used in the spanwise direction, thereby letting some coherence to build up in the flow.

On the other hand, using no-slip walls in the spanwise direction breaks up the coherence of the primary vortex within the cavity. Fig. A.5(b) shows slightly larger secondary vortices in the left bottom and top cavity corners. Rockwell and Knisely [98] observed

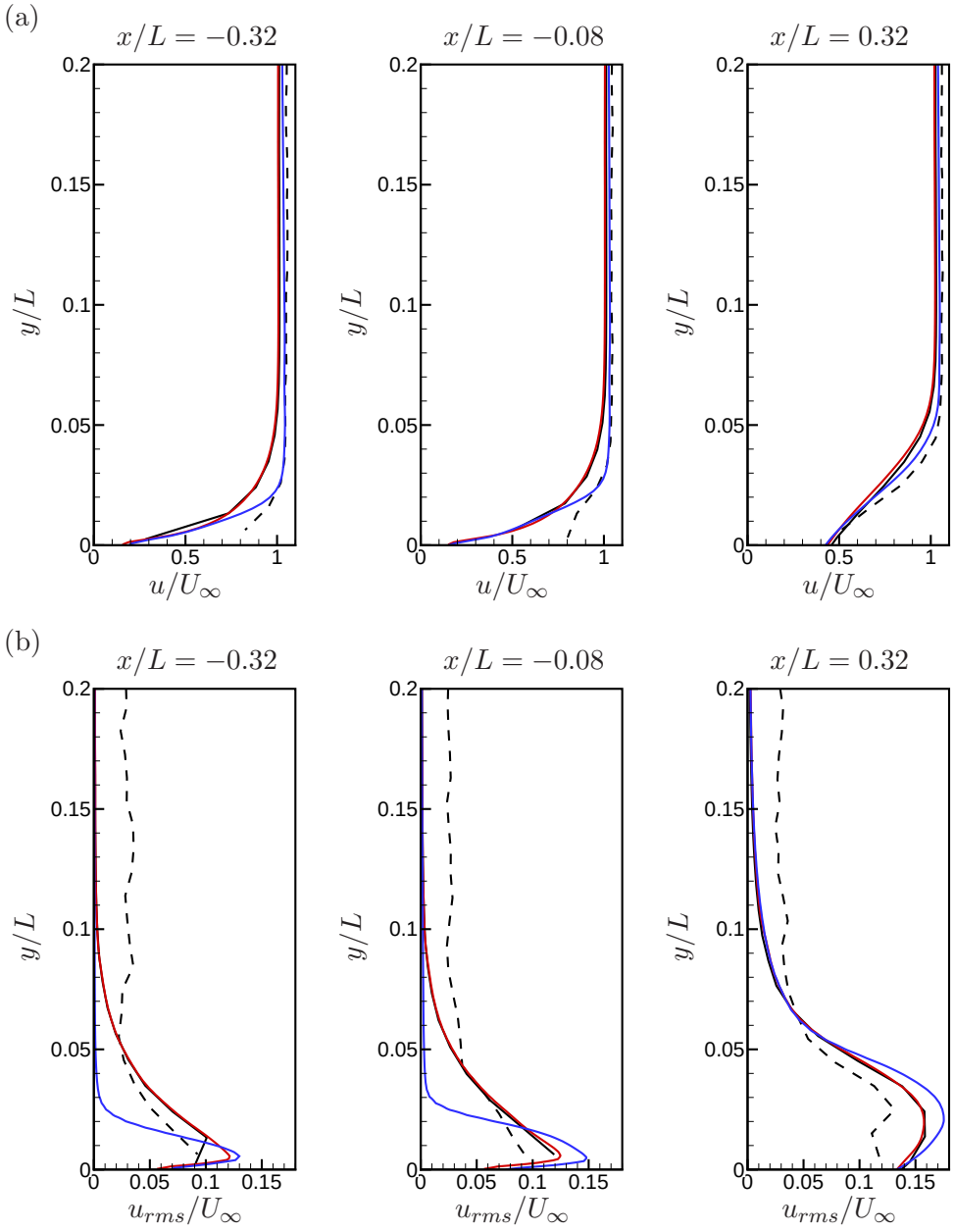

Figure A.6: Comparison of (a) streamwise mean velocity, (b) streamwise rms velocity profiles near the leading corner. —— LES, ---- experiment [13], —— spanwise periodic b.c., —— convergent inflow section LES

a secondary longitudinal instability that acts on the primary instability associated with the growth of the spanwise vortex tubes. To extend that, it can be postured that the secondary vortices add low frequency instabilities which aid to break up the spanwise

coherence of the cavity flow. This is also in agreement with the observation of Lin and Rockwell [99] who suggested a possible low-frequency modulation by the unsteady recirculating flow in the cavity.

Fig. A.6 shows the streamwise u-velocity profiles near the cavity leading edge when different boundary conditions are used. Profiles are shown for mean and rms of u-velocity at streamwise locations, of which two are upstream ($x/L = -0.32, -0.08$)and one is downstream ($x/L = 0.32$) of the leading edge. Comparing different spanwise b.c., the LES using no-slip walls (solid) has almost the same profiles as obtained using spanwise periodic b.c. (red). It is clear that the mean u-velocity profiles from the convergent inflow section LES (blue) are in better agreement with the experiment as must be expected. However, lack of appropriate turbulence information in the convergent inflow section LES is evident from the rms profiles. u_{rms} is overpredicted near the wall which could be attributed to inadequate near-wall resolution. But this turbulence dies down very quickly away from the wall. This might suggest that the turbulence in the incoming flow isn't developed enough to sustain itself away from the wall. Better modeling of the notches may be required to address this issue of reduced turbulence.

To summarize, better agreement with the experimental statistics in the cavity are obtained using (i) no-slip condition than using periodic b.c. in the spanwise walls, and (ii) turbulent inflow condition (described in sec. A.2.2) as compared to the convergent inflow section. The single phase results are validated with experiments in sec. A.5.1.

A.5 Results

Large eddy simulations are performed for the aforementioned geometry and boundary conditions at $Re_L = 1.7 \times 10^5$. The single, carrier-phase flow is analyzed in the next section followed by the two-phase flow with bubbles.

A.5.1 Single-phase

Fig. A.7 compares instantaneous pressure distribution near the cavity trailing edge during low and high pressure events above corner. The low pressure region is indicative of the presence of the vortex core. Clearly, when the vortex is further away ($x/L \sim 0.8$) from the trailing edge, there is a low pressure region above the corner. When this

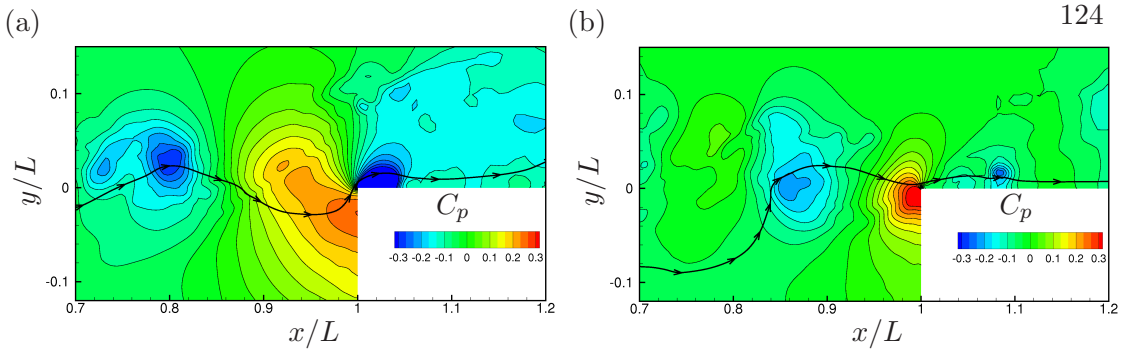

Figure A.7: Instantaneous pressure distribution during (a) low pressure above corner (b) high pressure above corner.

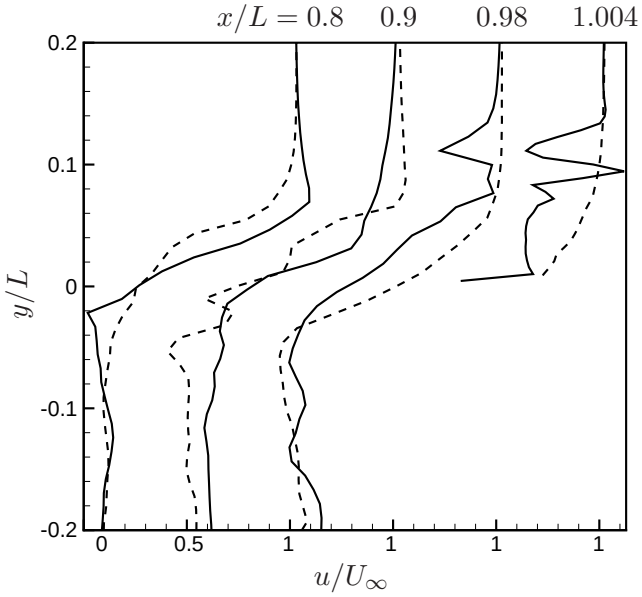

Figure A.8: Comparison of streamwise velocity profiles during low and high pressure events over the corner. —— low pressure, ---- high pressure.

vortex travels further downstream ($x/L \sim 0.9$), the corner experiences high pressure. The downwash due to the closer vortex reduces the curvature of the streamline above the corner resulting in higher pressure. The effect of these vortices on the streamwise velocity also shows up in fig. A.8. The presence of the vortex at ($x/L = 0.8$) during low pressure can be seen in the changing sign of the u-velocity around $y/L = 0.8$. The spectra of pressure at $(x/L, y/L, z/L) = (1.270, 0.01, 0)$ yields a frequency of $f \sim 160$ Hz., corresponding to a Strouhal number of $St = fL/U_\infty = 1.22$. These observations are in agreement with those of Liu and Katz [13].

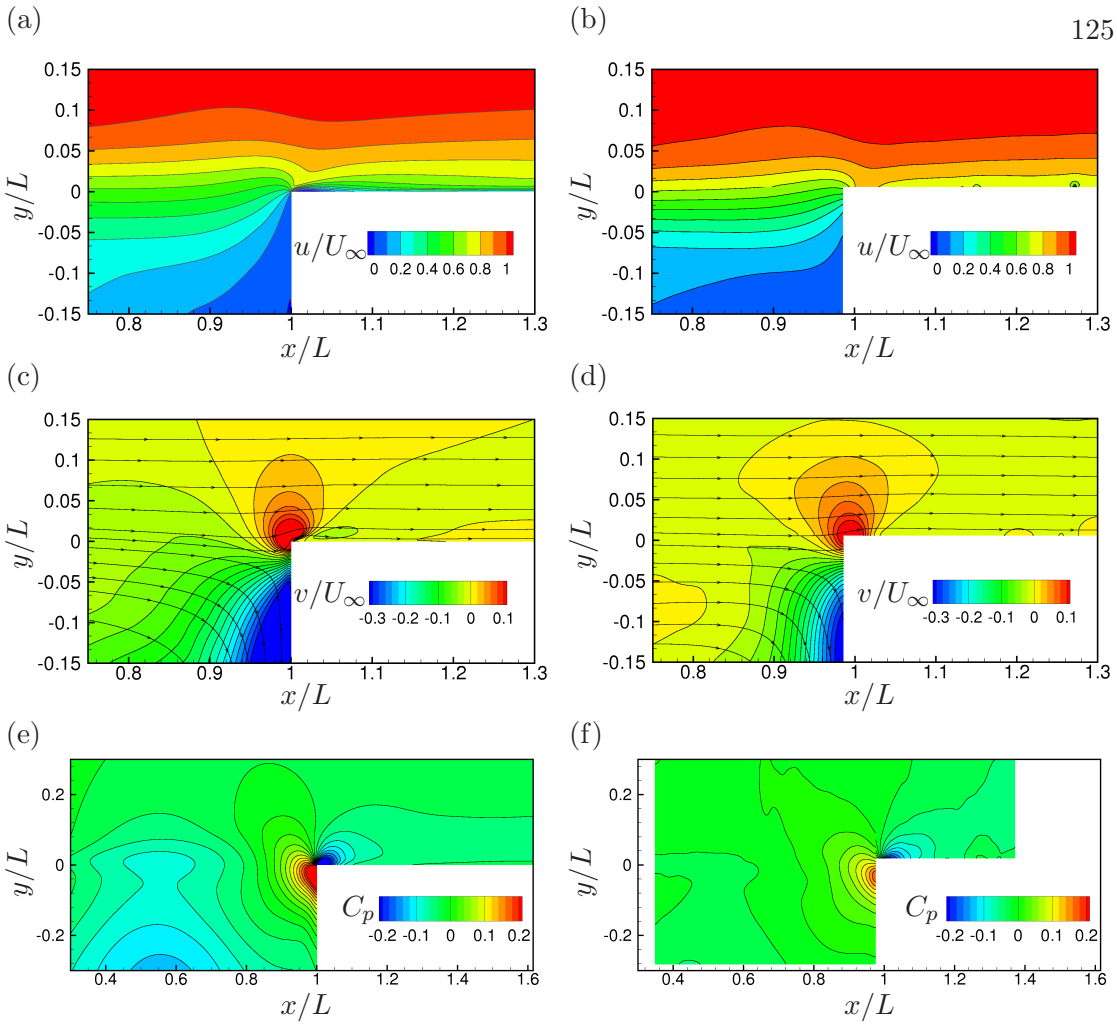

Figure A.9: Comparison of time averaged statistics from LES and experiment [13]; u : (a) LES (b) experiment; v with streamlines: (c) LES (d) experiment; C_p : (e) LES (f) experiment.

Converged, time averaged statistics are obtained for 102 flow through times (where one flow through time is taken to be L/U_∞). A.9 shows reasonable agreement between the LES and experiment [13] for mean u and v velocity, and mean pressure coefficient. The highest pressure fluctuations occur in the shear layer just upstream of and on the cavity trailing edge (fig. A.10). It will be shown later that most of the cavitation occurs on the cavity trailing edge. Axial profiles of mean and rms of the streamwise velocity are extracted at three locations upstream ($x/L = -0.32$, -0.20 and -0.08) and downstream ($x/L = 0.08$, 0.20 and 0.32) of the leading edge in the shear layer. The

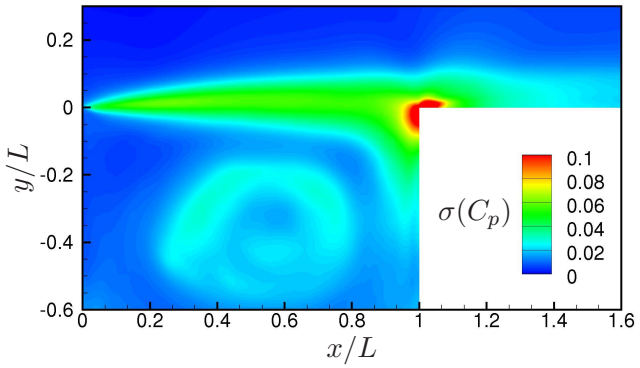

Figure A.10: Distribution of rms pressure $\sigma(C_p)$.

LES is in reasonable agreement with the experiment (figs. A.6 and A.11); insufficient near-wall grid resolution could be responsible for the near-wall over-prediction of u_{rms}.

A.5.2 Bubbles

Bubbles are injected in a small window above the cavity at $x = 3\ mm$, $0.25 < y\ (mm) < 1.5$ along the entire span. This window is chosen so that the bubbles get entrained in the shear layer and cavitate in the low pressure regions. The sensitivity to initial bubble radius is studied using three initial bubble radii $R_{b0} = 10,\ 50$ and $100\mu m$. The effect of the cavitation index σ is studied at two indices $\sigma = 0.4$ and 0.9. Henceforth, results are shown for $\sigma = 0.4$ unless noted as $\sigma = 0.9$.

Liu and Katz [13] observe that the first location of cavitation inception is the cavity trailing edge regardless of the free-stream speed and dissolved gas content in the water. Fig. A.12 shows an instantaneous distribution of bubbles for initial bubble radii $R_{b0} = 10\mu m$ and $R_{b0} = 50\mu m$ at a cavitation number of $\sigma_v = 0.4$. Henceforth, the cavity is outlined by solid lines. Bubbles are shows at the same instant of time and are colored by radius. Cavitation is seen readily at the cavity trailing edge, in agreement with experiment. In fact, bubbles with larger initial radius ($R_{b0} = 50\mu m$) are seen to cavitate sooner, in the shear layer. Bubbles with $R_{b0} = 1\mu m$, $10\mu m$ do not show this early cavitation.

PDF analysis of the bubble size distribution and Lagrangian statistics are computed for 8.1 flow through times. The ensemble averaged trajectory of the bubbles is not too different for different initial bubble radii and cavitation index (fig. A.13(a)). The

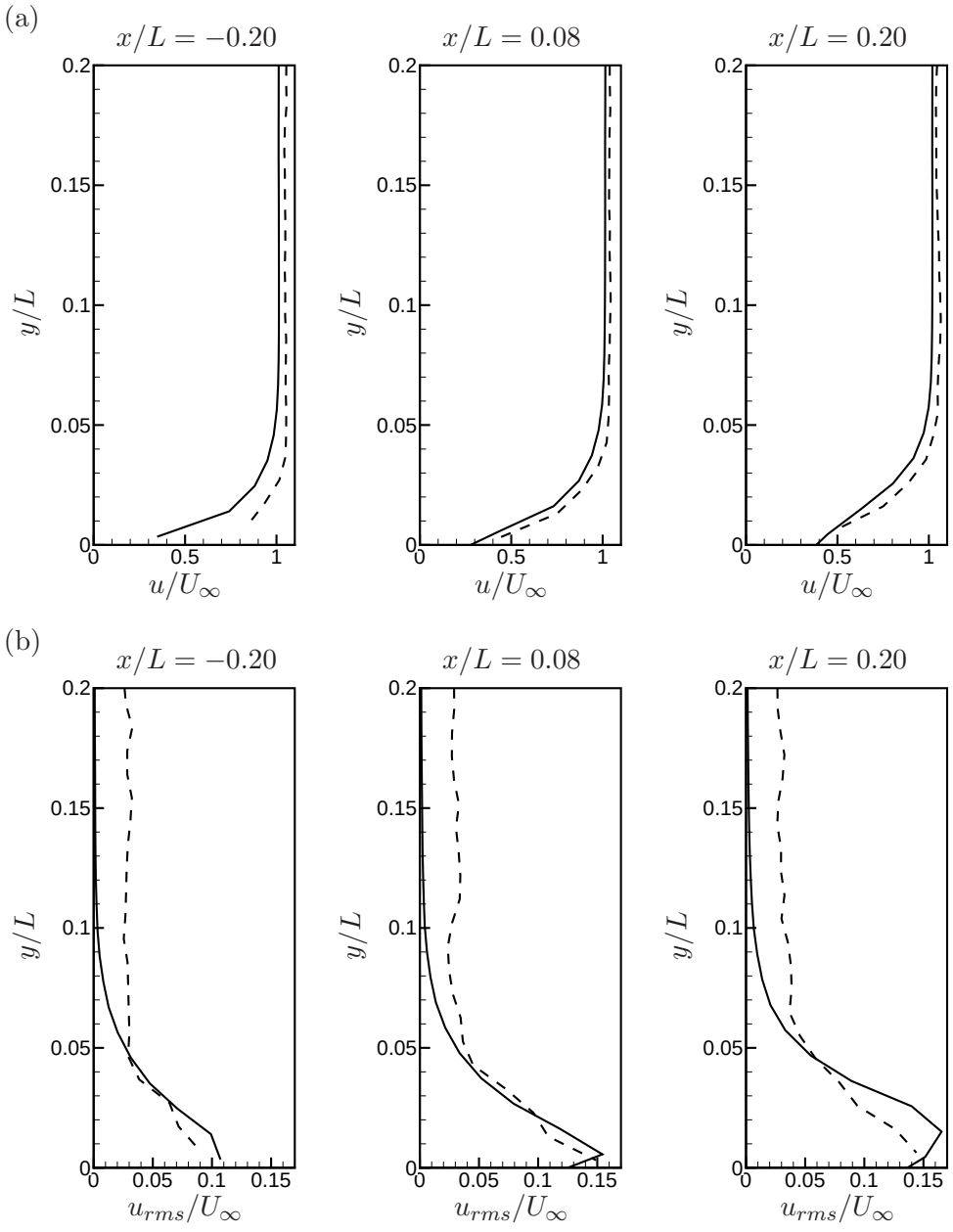

Figure A.11: Comparison of (a) streamwise mean velocity, (b) streamwise rms velocity profiles upstream of the leading corner. —— LES, ---- experiment [13].

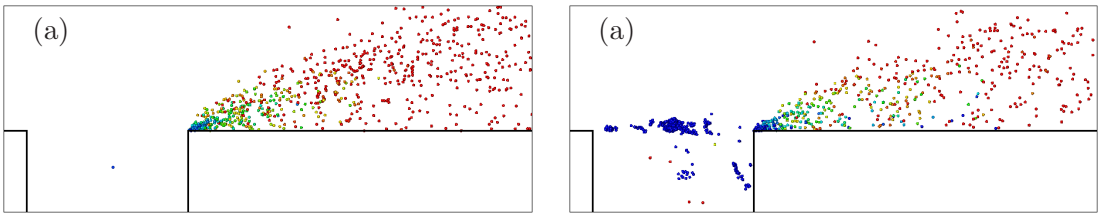

Figure A.12: Visual evidence of cavitation at $\sigma = 0.4$: (a) $R_{b0} = 10\mu m$, (b) $R_{b0} = 50\mu m$. Only bubbles bigger than $R_b = 60\mu m$ are shown for clarity. Blue indicates smaller bubbles while red indicates largest bubbles.

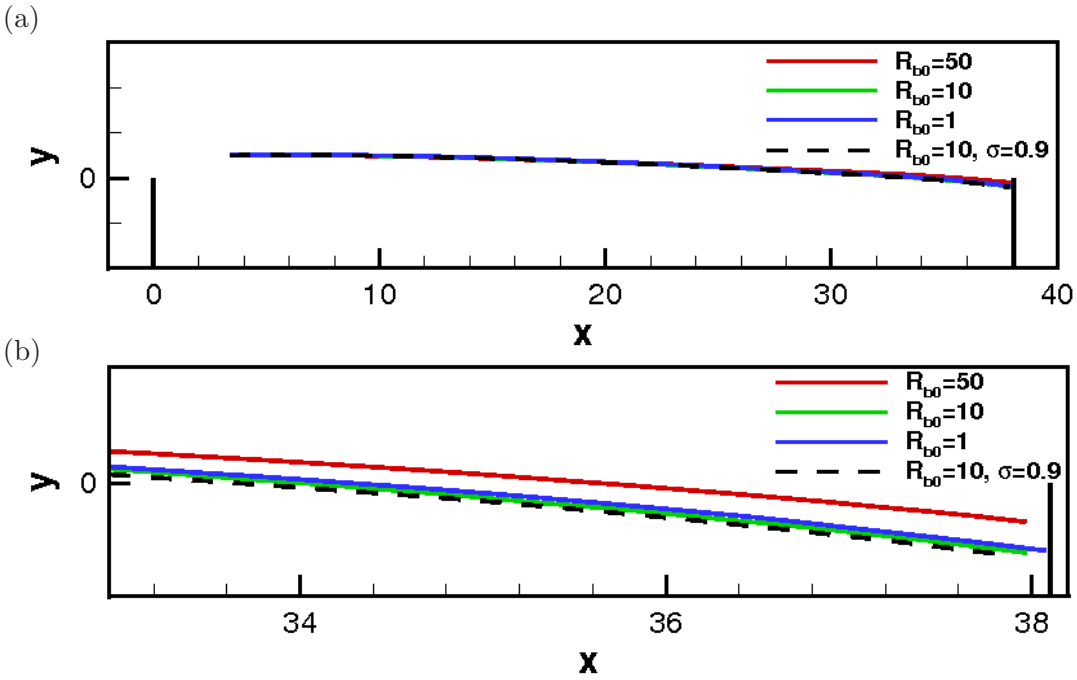

Figure A.13: Lagrangian averaged bubble trajectory in the shear layer. (a) view along the entire cavity, (b) zoomed in near the trailing edge.

trajectory for $R_{b0} = 50\mu m$ diverges from the rest near the trailing edge as seen in fig. A.13(b).

Figs. A.14(a)-(c) plot the variation of ensemble averaged bubble pressure. Note that the lowest mean pressure ($\overline{C_p}$) occurs around $x \sim 20$ which shows up as cavitation in zone 2 of the PDF (shown in fig. A.15 and discussed later). Some bubbles which cavitate here, grow upto the maximum allowed $R_{b,max}$ (green triangles in the PDF

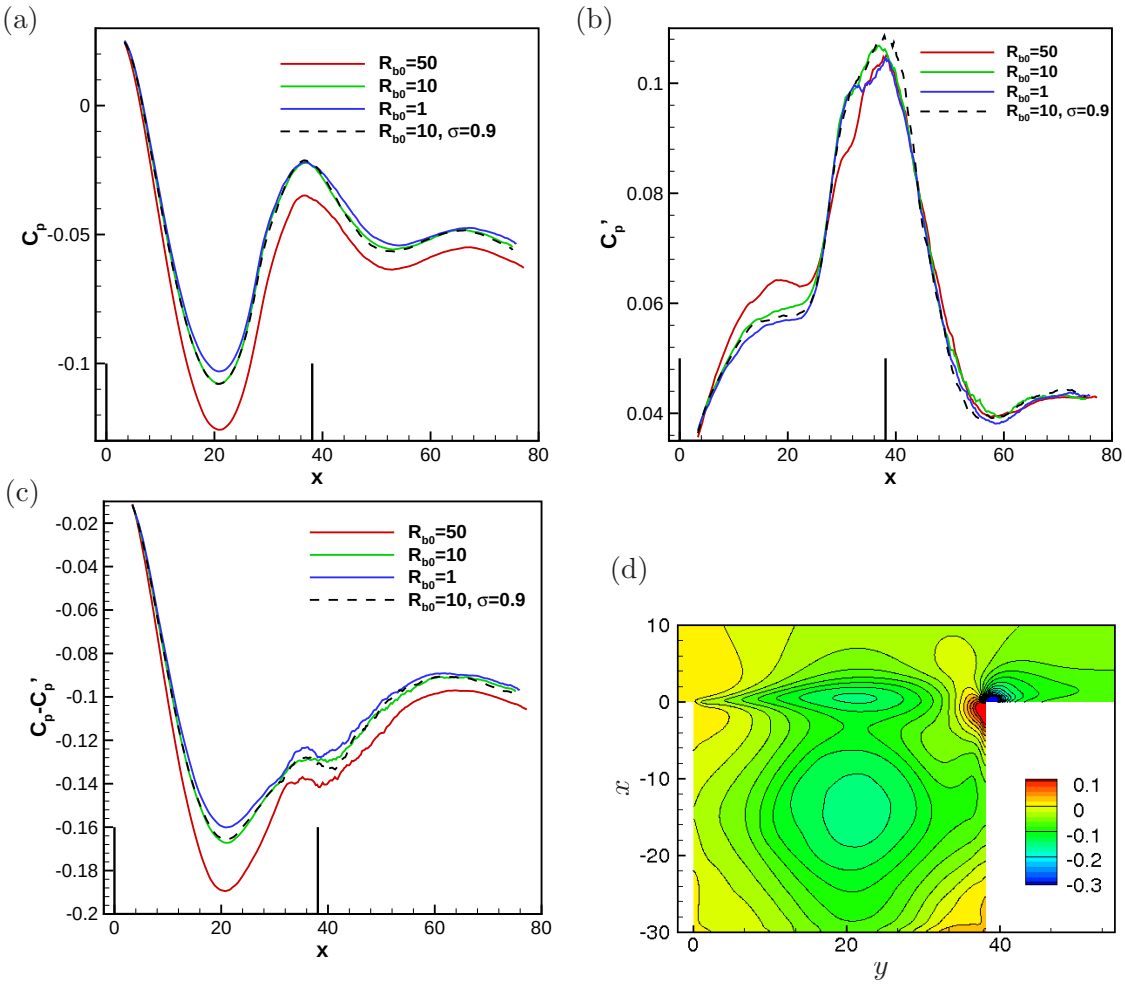

Figure A.14: Lagrangian averaged (a) $\overline{C_p}$, (b) $\sigma(C_p)$, (c) $\overline{C_p} - \sigma(C_p)$ of bubbles in the shear layer. (d) Contours of $\overline{C_p} - \sigma(C_p)$ of the single phase flow.

plots) because of low $\overline{C_p}$. Bubbles with initial radius $R_{b0} = 50\mu m$ experience the lowest mean pressure. They also experience a local maxima around $x \sim 20$ for the pressure rms $\sigma(C_p)$. $\overline{C_p} - \sigma(C_p)$ is also plotted in fig. A.14(c) to give a statistical idea about the lowest instantaneous pressure. It is least at $x \sim 20$, indicating that this might be a preferred location for cavitation for all cases. Furthermore the bubbles with the larger initial radius ($R_{b0} = 50\mu m$) are most likely to cavitate on account of lowest $\overline{C_p} - \sigma(C_p)$. Comparing with the Eulerian $\overline{C_p}$ field (fig. A.14(d)), this is likely a vortex trapping effect, where larger bubbles are more easily captured in the vortex core than smaller

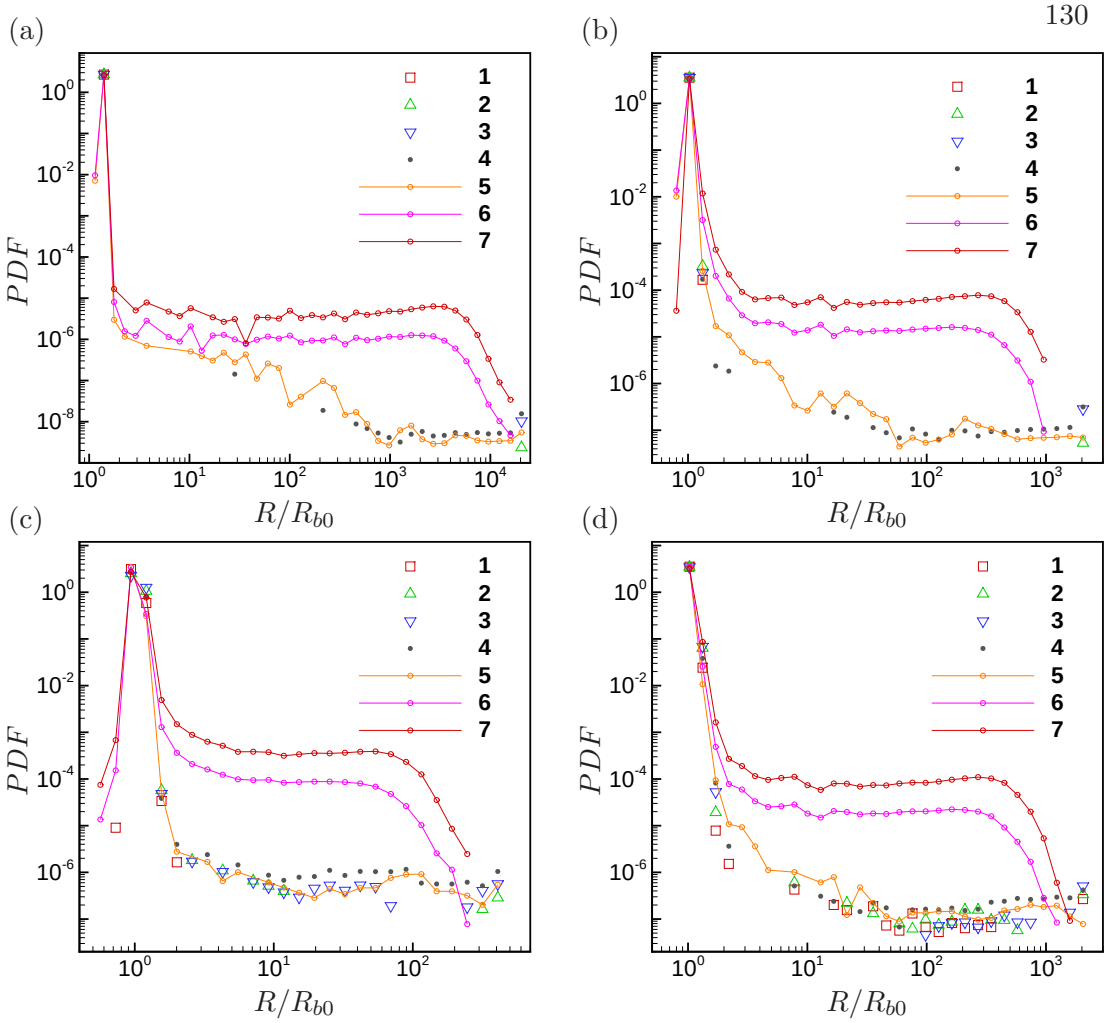

Figure A.15: PDF of number of bubbles from seven zones. (a) $R_{b0} = 1\mu m$, (b) $R_{b0} = 10\mu m$, (c) $R_{b0} = 50\mu m$ with $\sigma = 0.4$, and (d) $R_{b0} = 10\mu m$ with $\sigma = 0.9$.

bubbles [100].

Probability distribution functions (PDFs) of the number of bubbles are computed based on their growth ratio (r/r_0) and plotted in fig. A.15. The degree or ease of cavitation can be gauged from the values of the PDF. Conditional sampling is performed based on the location of the bubbles from seven equi-sized zones within $0.22 < x/L < 1.27$. For all cases shown, significant cavitation is seen in zones 6 and 7 which correspond to the region above the cavity trailing edge ($0.97 < x/L < 1.27$). Some cavitation is also seen in the shear layer (particularly zones 4 and 5, $0.67 < x/L < 0.97$), although

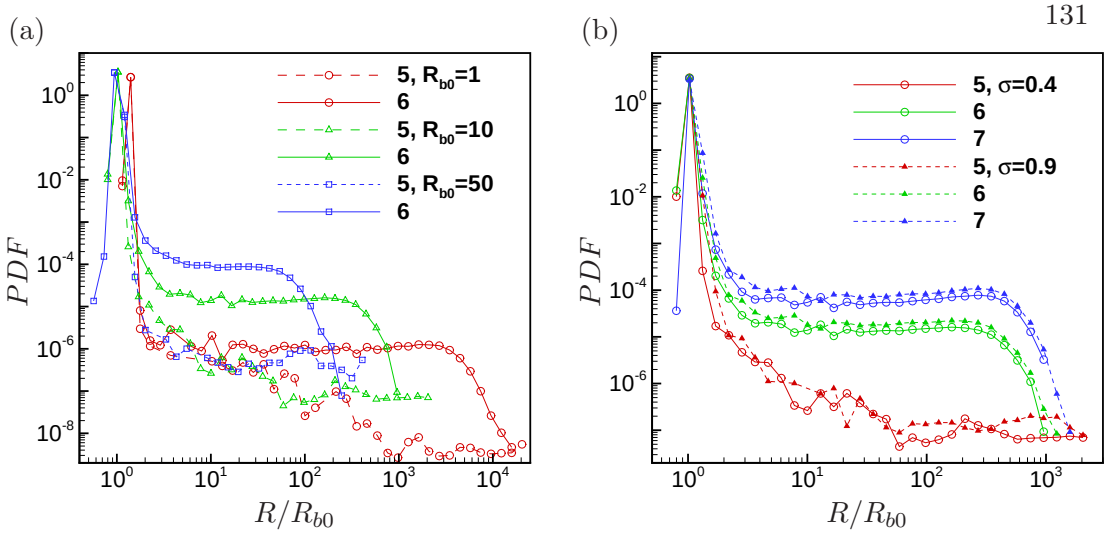

Figure A.16: PDF of number of bubbles. (a) Effect of initial bubble size in zones 5 and 6. (b) Effect of cavitation index σ for $R_{b0} = 10\mu m$ in zones 5, 6, and 7.

the PDF values of the big bubbles ($R_b > 1mm$) are almost three decades lower than in zone 7. Very few bubbles get trapped in the shear layer and cavitate immediately in the vortex cores (zones 2 and 3). For all the cases shown except $R_{b0} = 1\mu m$, the peak of the PDF is at $R/R_{b0} = 1$. This implies that bubbles with sizes close to the initial seed bubbles are the most numerous in the flow, as is expected. However, at $R_{b0} = 1\mu m$ (fig. A.15(a)), bubbles twice their initial radius are most numerous. Also, there are no significant number of bubbles smaller than $R = R_{b0} = 1\mu m$; most collapse perhaps. In contrast, when bubbles start off relatively big ($R_{b0} = 10\mu m$ and $50\mu m$), significant number of bubbles reduce in size ($R/R_{b0} < 1$) and persist in the higher pressure regions above the cavity trailing edge (zones 6 and 7).

Bubbles with initial radius $R_{b0} = 1\mu m$ seem to grow in size the least (fig. A.15(a)) and those with $R_{b0} = 50\mu m$ grow most easily (fig. A.15(c)). In fact, increased cavitation is seen even in the shear layer (zone 1) for $R_{b0} = 50\mu m$. The effect of initial bubble size on the prevalence of cavitation can be gauged from comparing the PDFs for any zone. Fig. A.16(a) clearly shows that cavitation increases with increasing initial bubble radius. Fig. A.16(b) shows the effect of cavitation index σ for $R_{b0} = 10\mu m$. Bubbles do not seem to be sensitive to increasing of the pressure up until $\sigma = 0.9$. Fig. A.17 plots the lift, drag, fluid acceleration and the total force on the bubbles.

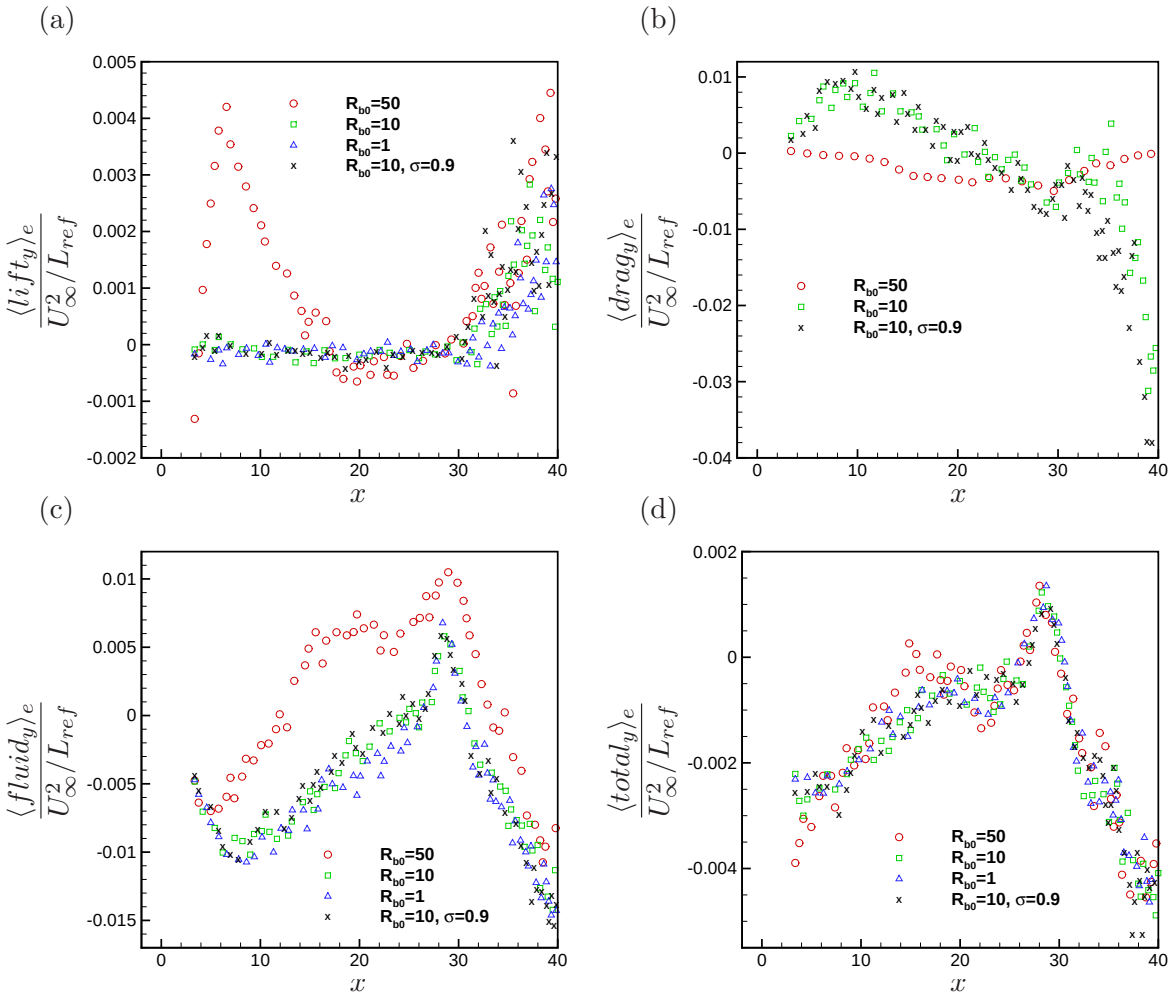

Figure A.17: Force budgets in y-direction. (a) lift, (b) drag, (c) fluid acceleration and the (d) total force on the bubbles.

Appendix B

Details for Constrained SGS Model

B.1 Pseudo-spectral method

This numerical method is similar to that used in Kim et al. [101]: Fourier expansion with 3/2–rule dealiasing for homogeneous (x and z) directions, and a Chebychev polynomial expansion is adopted in the wall-normal direction. The governing equations (eq. 2.5) are written in terms of the resolved wall–normal vorticity ($\overline{g} \equiv \partial\overline{u}/\partial z - \partial\overline{w}/\partial x$) and the Laplacian of the resolved wall–normal velocity ($\overline{\phi} \equiv \nabla^2\overline{v}$) to eliminate the pressure, which take the form

$$\begin{aligned} \frac{\partial \nabla^2 \overline{v}}{\partial t} &= h_v + \frac{1}{Re_\tau}\nabla^4 \overline{v}, \\ \frac{\partial \overline{g}}{\partial t} &= h_g + \frac{1}{Re_\tau}\nabla^2 \overline{g}, \\ \nabla \cdot \overline{\mathbf{u}} &= 0, \end{aligned} \tag{B.1}$$

where $h_v = -\partial_y(\partial_x H_1 + \partial_z H_3) + (\partial_x^2 + \partial_z^2)H_2$, $h_g = \partial_z H_1 - \partial_x H_3$, and $H_i = -\partial_j(\overline{u}_i\overline{u}_j) - \partial_j \tau_{ij}^M$ $(i = 1, 2, 3)$ are nonliear and SGS terms. Plane–averaged streamwise and spanwise velocities, or wall–parallel velocities at $(k_x, k_z) = (0, 0)$ modes are integrated separately. The flow is driven by a fixed mean pressure gradient, and the governing equation (B.1) is naturally normalized in terms of u_τ and δ. h_v and h_g are treated explicitly with

the Adams–Bashforth scheme and viscous terms are treated implicitly with the Crank–Nicolson method. A temporal discretization scheme similar to Ekaterinaris [102] is used for the implicit treatment of viscous terms. As the test filter of DSM, the sharp cutoff filter is applied to homogeneous directions with $\widehat{\Delta}/\overline{\Delta} = 2$.

B.2 Finite-difference method

Eq. 2.5 is solved by a second order fully conservative finite difference scheme in a staggered grid system [103]. A semi-implicit time marching algorithm is used where the diffusion term in the wall normal direction is treated implicitly with the Crank-Nicolson scheme and a third order Runge-Kutta scheme [104] is used for all other terms. The fractional step method [105] is used in order to enforce the divergence free condition. The resulting Poisson equation for the pressure is solved using Fourier Transform in the streamwise and spanwise directions and a tri-diagonal matrix algorithm in the wall normal direction. A three-point Simpson's filter is used as the test filter along the wall parallel directions with $\widehat{\Delta}/\overline{\Delta} = 2$.

B.3 RANS model to obtain Reynolds stress

The Reynolds-Averaged Navier-Stokes (RANS) equations are obtained by performing an ensemble average of the Navier-Stokes equations (eqs. 2.1-2.2):

$$\begin{aligned} \frac{\partial \langle u_i \rangle}{\partial x_i} &= 0, \\ \frac{\partial \langle u_i \rangle}{\partial t} + \frac{\partial}{\partial x_j}(\langle u_i \rangle \langle u_j \rangle) &= -\frac{\partial \langle p \rangle}{\partial x_i} + \nu \frac{\partial^2 \langle u_i \rangle}{\partial x_j \partial x_j} - \frac{\partial}{\partial x_j}(\langle u_i u_j \rangle - \langle u_i \rangle \langle u_j \rangle), \end{aligned} \tag{B.2}$$

where $\langle \cdot \rangle$ denotes an ensemble average, equivalent to $(\cdot)_{t,h}$ = (temporal + spatial averaging in homogeneous directions, if any). Note that $\mathcal{R}_{ij} = \langle u_i u_j \rangle - \langle u_i \rangle \langle u_j \rangle$ is the RANS Reynolds stress.

In a practical computation, the Reynolds stress $\mathcal{R}_{ij}$ in A_{ij} (eq. 5.10) could be replaced by RANS model $\mathcal{R}^M_{ij}$. The algebraic eddy viscosity model is given by:

$$\mathcal{R}^M_{ij} = -2\nu^{\mathcal{R}}_T \left\langle \overline{S}_{ij} \right\rangle, \tag{B.3}$$

where, $\nu_T^{\mathcal{R}}$ denotes RANS eddy viscosity. The Spalart-Allmaras model [106] for RANS eddy viscosity ν_T^R is used:

$$\frac{D\tilde{\nu}}{Dt} = c_{b1}\tilde{S}\tilde{\nu} + \frac{1}{\sigma}\left[\nabla\cdot\left(\left(\nu+\tilde{\nu}\right)\nabla\tilde{\nu}\right) + c_{b2}\left(\nabla\tilde{\nu}\right)^2\right] - c_{w1}f_w\left(\frac{\tilde{\nu}}{d}\right)^2, \tag{B.4}$$

where $\nu_T = \tilde{\nu}f_{v1}$, $f_{v1} = \chi^3/(\chi^3 + c_{v1})$ and $\chi = \tilde{\nu}/\nu$. S is either magnitude of vorticity or strain rate. The model is closed with the following coefficients and wall functions:

$$\begin{gathered}
\tilde{S} = S + \tfrac{\tilde{\nu}}{\kappa^2 d^2} f_{v2},\ f_{v2} = \left(1 + \tfrac{\chi}{c_{v2}}\right)^{-3}, \\
f_w = g\left(\tfrac{1+c_{w3}^6}{g^6+c_{w3}^6}\right)^{1/6},\ g = r + c_{w2}(r^6 - r),\ r = \tfrac{\tilde{\nu}}{\tilde{S}\kappa^2 d^2}, \\
c_{b1} = 0.1355,\ \sigma = \tfrac{2}{3},\ c_{b2} = 0.622,\ \kappa = 0.41,\ c_{v2} = 5, \\
c_{w1} = \tfrac{c_{b1}}{\kappa^2} + \tfrac{1+c_{b2}}{\sigma},\ c_{w2} = 0.3,\ c_{w3} = 2,\ c_{v1} = 7.1.
\end{gathered} \tag{B.5}$$